UNIVERSITÄTSKLINIKUM HAMBURG-EPPENDORF

Zentrum für Experimentelle Medizin
Institut für Biochemie und Signaltransduktion

Prof. Dr. Aymelt Itzen

Role of diaphanous homolog 1 (DIAPH1) in chromosomal instability of colorectal carcinoma cells

Dissertation
zur Erlangung des Grades eines Doktors der Dr. rer. biol. hum.
an der Medizinischen Fakultät der Universität Hamburg.

vorgelegt von

Shumin Miao
aus Ganzhou

Hamburg 2020

Angenommen von der
Medizinischen Fakultät der Universität Hamburg am:
18.11.2020

Veröffentlicht mit Genehmigung der
Medizinischen Fakultät der Universität Hamburg.

Prüfungsausschuss, der/die Vorsitzende:
Prof. Dr. Sabine Windhorst

Prüfungsausschuss, zweite/r Gutachter/in:
PD Dr. Leticia Oliveira-Ferrer

Content

1 Introduction

1.1 Epidemiology and tumorigenesis of colorectal carcinoma

Colorectal carcinoma (CRC) is a common and lethal disease, ranking the third most commonly diagnosed cancer in males and the second in females worldwide[1]. Currently number of newly diagnosed CRC cases is increasing progressively, and CRC remains to be the fourth most lethal cancer worldwide, leading to almost 900 000 deaths annually [1,2].

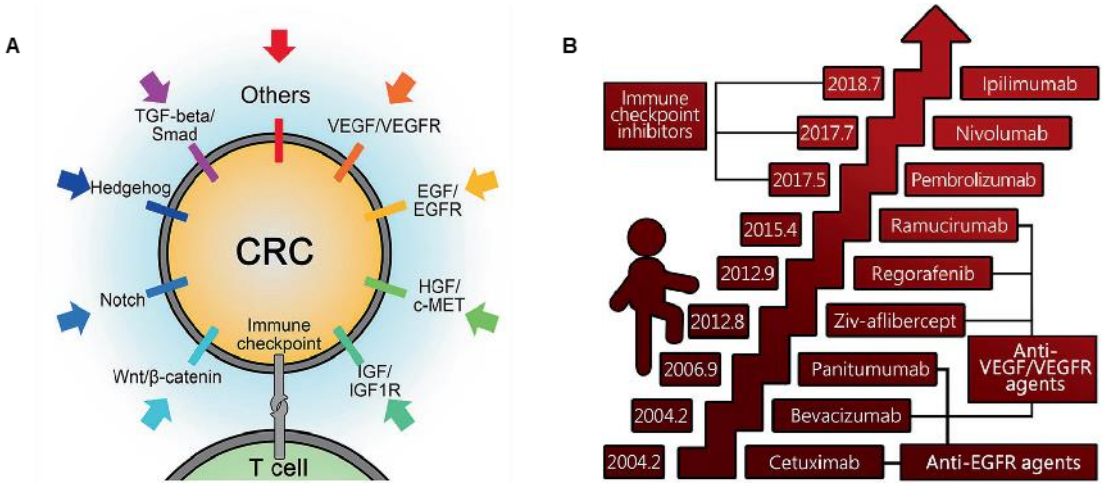

Figure 1 Molecular pathways and development of targeted therapies of CRC. *(A) Potential drug-target sites in molecular pathways for targeted therapies. (EGF/EGFR: epidermal growth factor/epidermal growth factor receptor; HGF: hepatocyte growth factor; c-MET: mesen-chymal–epithelial transition factor; IGF/IGF-1R: insulin-like growth factor/ insulin-like growth factor 1receptor; TGF: transform-ing growth factor); (B) Landscape of United States of America Food and Drug Administration (FDA)-approved molecularly targeted drugs in CRC. (VEGF/VEGFR: vascular endothelial growth factor/vas-cular endothelial growth factor receptor)* [2].

Although recent treatment of CRC has been significantly improved, the overall survival (OS) for advanced disease is only 3 years, and patients suffering from metastatic CRC (mCRC) still have the lowest survival rates [1]. Treatment for CRC largely depends on the stage of cancer. Currently, treatments for mCRC mainly include cytotoxic chemotherapy and targeted therapies in combination with surgical excision for locoregional and metastatic lesions [1,3]. Chemothera-pies are the main choices when cancer has spread and surgery is limited (https://www.can-cer.org/cancer/colon-rectal-cancer/treating/by-stage-colon.html). Systemic cytotoxic chemo-therapy given at maximum tolerated doses (MTD) has shown efficiency for treatment of mCRC, with 5-fluorouracil (5-Fu) widely used [4]. However, this type of therapy management exhibits certain limitations, including systemic toxicity, drug resistance, low tumor-specific selectivity,

and abundant economic costs [2]. Based on this consideration, concept of molecular targeted therapy has flourished in the recent decades, working specifically on both carcinoma cells and tumor microenvironment (TME), including cell proliferation, migration, blood vessels and immune cells (Fig. 1) [2]. It involves targeting of abundant pathway of signaling cascade amplification to affect tumor progression, such as the RAS/RAF/MEK/ERK pathway, and gene mutations related pathways.

Cell line	*MSI status*	*CIMP panel 1*	*CIMP panel 2*	*CIN*	KRAS	BRAF	PIK3CA	PTEN	TP53
CO-115	MSI	+	+	−[46]	wt	V600E	wt	E157fs;R233X	wt
DLD-1	MSI	+	+	−	G13D	wt	E545K;D549N	wt	S241F
HCT-116	MSI	+	+	−	G13D	wt	H1047R	wt	wt
HCT-15	MSI	+	+	−	G13D	wt	E545K;D549N	wt	S241F
LoVo	MSI	−	−	−	G13D;A14V	wt	wt	wt	wt
LS-174T	MSI	−	−	−	G12D	wt	H1047R	wt	wt
RKO	MSI	+	+	−	wt	V600E	H1047R	wt	wt
SW48	MSI	+	+	−	wt	wt	wt	wt	wt
TC71	MSI	+	−	−	G12D	wt	wt	R233X	C176Y;R213X
Caco-2	MSS	+	−	+[48]	wt	wt	wt	wt	E204X
COLO 320	MSS	−	−	+	wt	wt	wt	wt	R248W
EB	MSS	−	+	+	G12D	wt	E545K	wt	wt
FRI	MSS	−	−	+	G13D	wt	E545K	wt	C277F
HT-29	MSS	+	+	+	wt	V600E	P449T[b]	wt	R273H
IS1	MSS	+	−	+	G12D	wt	wt	wt	Y163H
IS3	MSS	−	−	+	G12D	wt	wt	wt	Y163H
LS1034	MSS	−	−	+	A146T[b]	wt	wt	wt	G245S
NCI-H508	MSS	−	−	+[46]	wt	G596R	E545K	wt	R273H
SW1116	MSS	+	−	+[47]	G12A	wt	wt	wt	A159D
SW480	MSS	−	−	+	G12V	wt	wt	wt	R273H;P309S
SW620	MSS	+	−	+[46]	G12V	wt	wt	wt	R273H;P309S
SW948	MSS	−	−	+[47]	Q61L	wt	E542K	wt	G117fs
V9P	MSS	−	−	+	wt	wt	wt	wt	G245D
WiDr	MSS	+	+	+[a]	wt	V600E	P449T[b]	wt	R273H

Table 1 Classification of colon cancer cell lines by signaling pathways (CIN, MSI and CIMP), and mutational status of critical cancer genes. *Mutation status in KRAS; BRAF; PIK3CA; PTEN and TP53 are displayed. (CIN:chromosomal instability; MSI: microsatellite instability; MSS; microsatellite stable; CIMP: CpG island methylator phenotype; wt: wild type)* [5].

However, mCRC often shows resistance to targeted therapy. For instance, RAS and BRAF genes mutation inhibit the efficiency of anti-epidermal growth factor receptor (EGFR) antibodies. In recent years, metronomic chemotherapy, defined as frequent administration of chemotherapeutic agents at a non-toxic dose without extended rest periods, seems to be a potential option for palliative management of patients with mCRC. In consistent with this, a phase III study, performed by Simkens and his college, showed improved prognosis in a patient cohort treated with metronomic chemotherapy, combining capecitabine with bevacizumab, comparing with standard MTD chemotherapy [4]. However, currently we still lack the clinical data on metronomic chemotherapy for mCRC. In this respect, it is necessary to deeply understand the underlying mechanisms and key processes of tumor resistance during treatment with chemotherapeutic agents as this will help to find specific targets to reduce the mortality of CRC [6].

It is well described that sequential accumulation of genetic and epigenetic alterations could drive the progression from colorectal adenoma to carcinoma [7]. Carcinogenesis of sporadic CRC (approximately 65% of CRC cases) is mainly implicated in three independent molecular pathways: chromosomal instability (CIN), microsatellite instability (MSI) and CpG island methylator phenotype (Table 1) [5,8,9]. Nearly 15-20% of sporadic cases exhibited high-frequency MSI

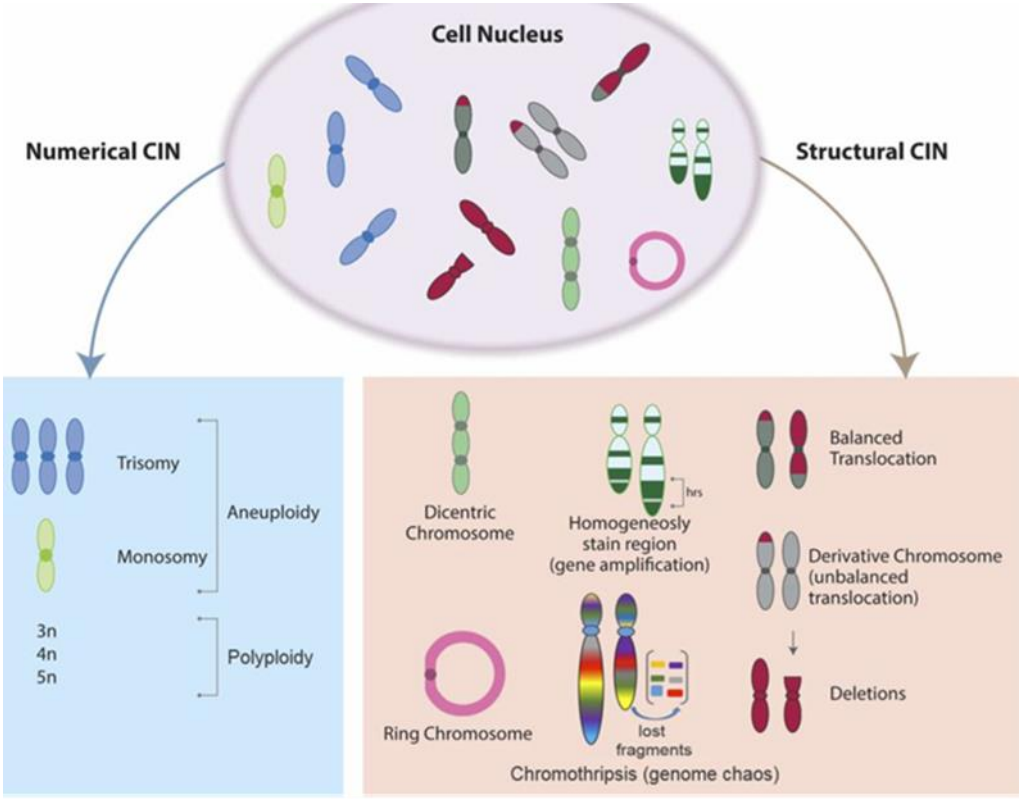

Figure 2 Features of chromosomal instability (CIN). *CIN is characterized by aberrations in chromosome segregation and classified as numerical CIN or structural CIN. Numerical CIN results from gain or loss of the whole chromosomes, while structural CIN results is determined by gain or loss of chromosomal fragments [10].*

phenotypes, a consequence of a defective DNA mismatch repair (MMR) system, while 80-85% of them shows CIN, with alterations in chromosome number and structure (Fig. 2) [9,11]. CIN is a hallmark of cancer and defined as the ongoing rates of chromosome mis-segregation [11]. Although CIN includes numerical and structural changes, robust evidence supported that numerical aberrations occurred much more frequently (~60-fold) in CIN+ cells [12]. CIN occurs when chromosomal "shuffling" is repeated during each cell division, and this continuous genomic alteration is generally associated with poor prognosis because of the rapid adaptation of tumor cells to the anticancer therapies (Fig. 3) [11,13]. However, when the CIN rate exceeds a certain

threshold, cell death will occur (Fig. 3) [11]. There is only a small subtype of human CRC having normal or almost normal chromosome numbers and little chromosomal differences between cells. Nevertheless, Bolhaqueiro et al. revealed that CIN is ongoing and widespread in patient-derived organoids (PDOs) and this phenomenon was observed regardless of changes in genetic background, including MSI [14]. Various present studies suggested that potential molecular

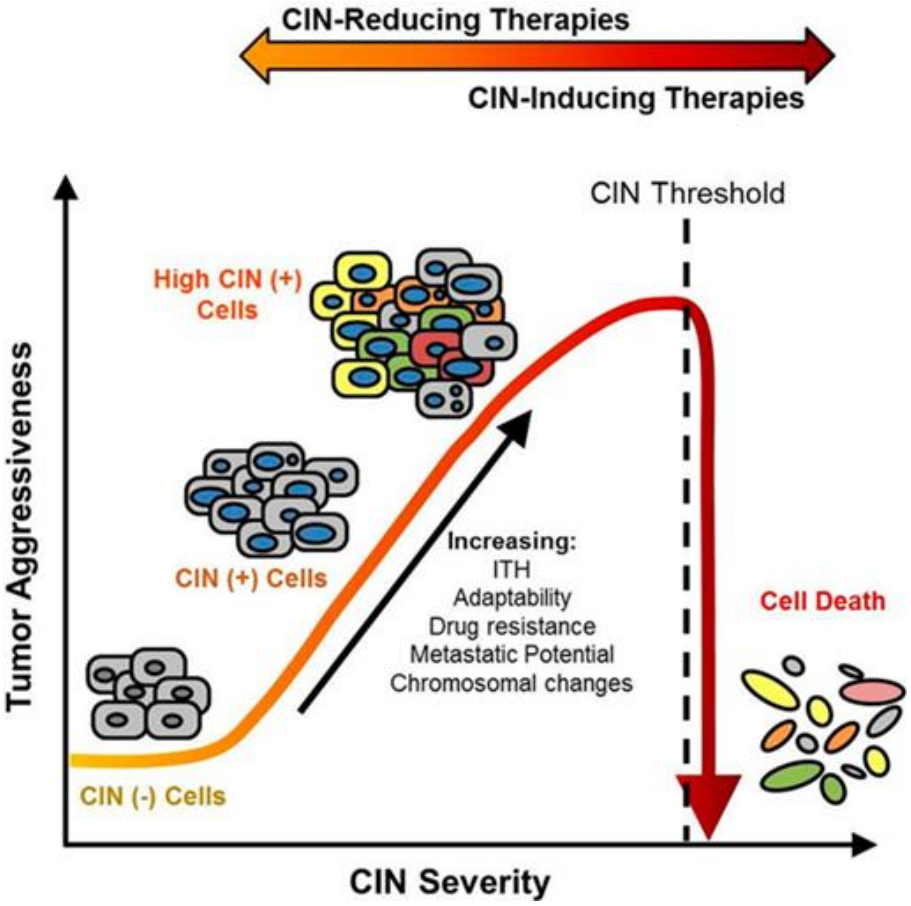

Figure 3 Schematic of tumor features associated with chromosomal instability (CIN) severity in Cancer. *Within a critical CIN threshold, increased CIN levels enhances the key tumor characteristics, including intratumoral heterogeneity (ITH), adaptability, drug resistance, metastatic potential and chromosomal changes. Once the level of CIN upon the threshold, cell death would be induced. The critical CIN threshold indicated by the black dotted line. +: positive; −: negative* [11].

causes for the CIN phenotype includes multipolar spindles, anaphase lagging chromosomes or chromatin bridges, and the most common among them are lagging chromosomes [12,15,16]. These chromosomes lagging in anaphase are mainly caused by improper activity of spindle microtubules, known as merotelic attachments (see section 1.2 for more details). Whereas researches from Kops group indicated different results by 3D live-cell imaging of patient-derived organoids (PDOs), and they revealed that the most commonly observed chromosomal abnormalities

were chromatin bridges instead of laggards [14]. These DNA bridges are actually sister DNA inter-linkage structures, resulting from fused chromosomes (Fig. 4, Fig. 7B) [14]. In order to complete cell-division processes, cleavage of chromatin bridge is required during anaphase/telophase and this process involves poleward transport force from spindle MTs (see details in section 1.2) [17]. Hence, chromosomal mis-segregation, mainly resulted from anaphase chromatin bridges (in 3D cell culture systems) or lagging chromosomes (in 2D monolayer), plays a crucial

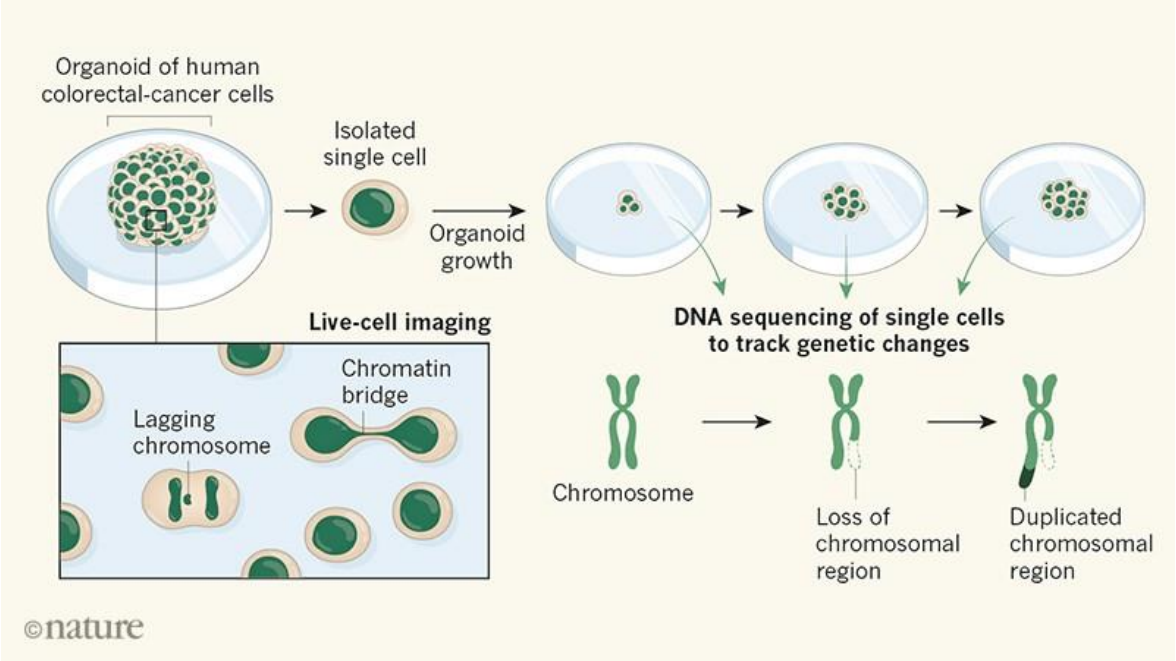

Figure 4 Tracking chromosomal abnormalities in patient-derived organoids (PDOs)*. Human colorectal carcinoma cells were cultured in a 3D cell culture system, termed as PDOs. Labelling the cells with a fluorescent tag enabled the chromosomes (green) to be observed during cell division using microscopy. Chromosomal abnormalities were thus tracked and imaged. The most common chromosomal alterations were chromatin bridges (insert), structures formed by fused DNA from sister chromosomes [14].*

role in the generation of CIN in CRC. Furthermore, this abnormalities of chromosome segregation are associated with dysfunction of spindle MTs.

1.2 Role of dysfunction of spindle MTs in CIN

In section 1.1, it is mentioned that chromatin bridges were observed most frequently in tumor PDOs, however, karyo typing analysis of cells cultured in standard 2D culture showed different results. They indicated that instead of errors occurring in pre-mitotic cells (acentric fragments and chromatin bridges), defects resulting from mitosis (lagging chromosomes) are the primary cause of numerical alteration [12,18,19]. In addition, numerical chromosomal aberrations make up

the majority of CIN (see more details in section 1.1), and these abnormalities result from chromosomal mis-segregation [12]. It is well established that accurate chromosome segregation requires proper activity of spindle MTs, termed kinetochore fibers, including faithful attachments between kinetochores and spindle fibers, and the power of chromosome movement generated by the dynamics of spindle MTs [20,21]. In conclusion, spindle MTs play a pivotal role in CIN, especially in numerical chromosomes aberration arising from lagging chromosomes during mitosis.

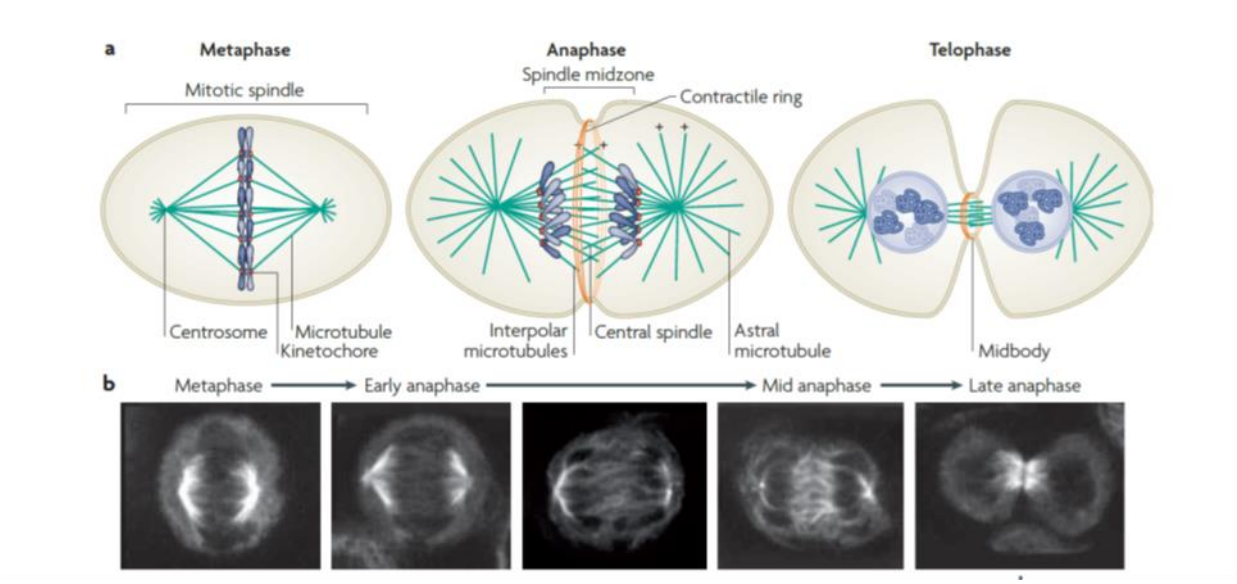

Figure 5 Role of spindle MTs in cell division. *(a) Distribution of different types of microtubules bundles in meta-, ana- and telophase. Spindle MTs are extended from two spindle poles, and consist of kinetochore, interpolar and astral microtubule. (b) Movement of cellular MTs were imaged from meta- to anaphase. Attached chromosomes were transported by spindle MTs toward opposite spindle poles. Microtubules and centrosome are shown in green; kinetochore is shown in red; chromosomes are shown in blue, contractile ring and midbody are shown in yellow.* [22]

During normal cell division, accurate chromosome separation requires a normal mitotic spindle apparatus. This apparatus is formed by microtubules, and consists of kinetochore microtubule (KT-MTs) bundles, astral microtubules and interpolar microtubules (Fig. 5) [22]. We acknowledge that KT-MTs capture each chromosome and make all of them aligned at the spindle equator, assisted by astral and interpolar MTs during metaphase. Before proceeding to anaphase, two kinetochores of each chromosome should be properly attached and then aligned to avoid chromosome gains or losses [23]. This process is controlled by the spindle assembly checkpoint (SAC). The SAC can restrain cells from entering anaphase until all the sister chromatids

achieve bioriented attachment to spindle MTs by generating cytoplasmic mitotic checkpoint complex (MCC), leading to the inhibition of the Anaphase Promoting Complex/Cyclosome (APC/C). Activation of SAC could prolong the mitotic state or cause mitotic catastrophe and even cell death [24,25]. Upon anaphase onset, spindle MTs bound to kinetochores can assemble at the interface of KT-MTs and disassemble at the centrosome by regulating its dynamics (Fig. 6) [26]. By this process, kinetochore fibers become short and transport attached sister chromatid

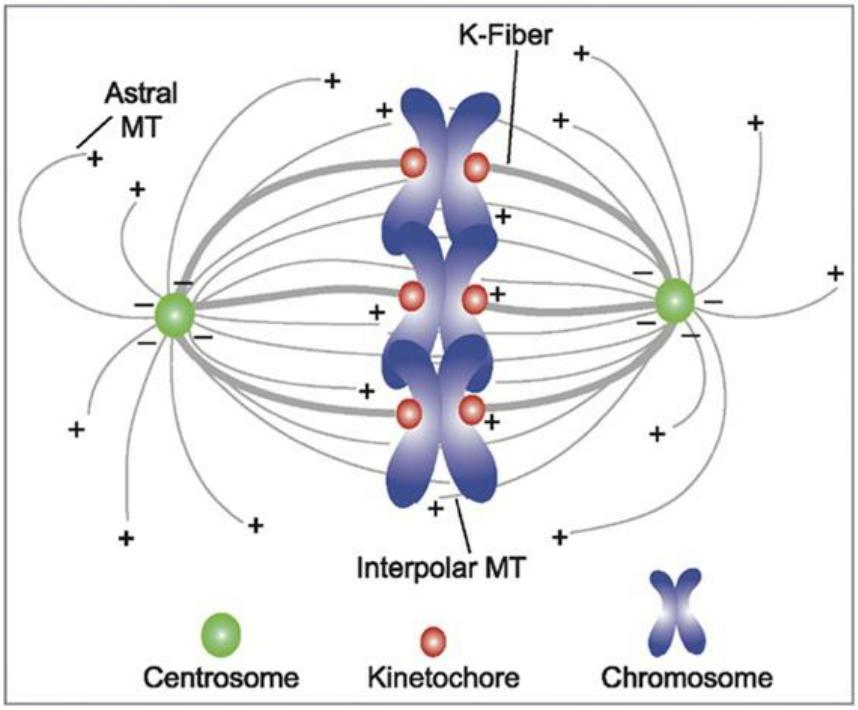

Figure 6 The dynamic properties of spindle MTs. *Sister chromosomes are attached to kinetochore MTs (known as K fibers) in the outer layer of kinetochore. Chromosome alignment and segregation were achieved by the assembly/disassembly of spindle MT. The minus ends (less dynamic) of MTs are firmly anchored at the centrosomes, served as microtubule organizing center, while the more dynamic plus ends extend toward the spindle equator and cell periphery. Microtubules are shown in gray; centrosomes are shown in green, kinetochores are shown in red; chromosomes are shown in blue. Positions of MT minus (−) ends versus plus (+) ends are indicated* [26].

towards the spindle poles. It is apparent that chromosome segregation requires faithful KT-MT attachment to kinetochores, and kinetochore microtubules should be sufficiently stabilized. Those attachments, on the other hand, must be dynamic enough to achieve biorientation, permitting correction of malorientations, and then separate chromosomes [19]. Hence, precise control of the balance of spindle MTs activity is essential to chromosome segregation.

The persistence of improper kinetochore attachment is the primary mechanism of CIN. Types of erroneous KT-MT attachments are shown in figure 7A. Sister kinetochores are physiologically attached to microtubules extending from opposite spindle poles. Interestingly, Kinetochore fibers could also attach to one (monotelic attachment) and/or both sister chromatids (syntelic attachment) from the same spindle pole, leading to chromosomal gain or loss.

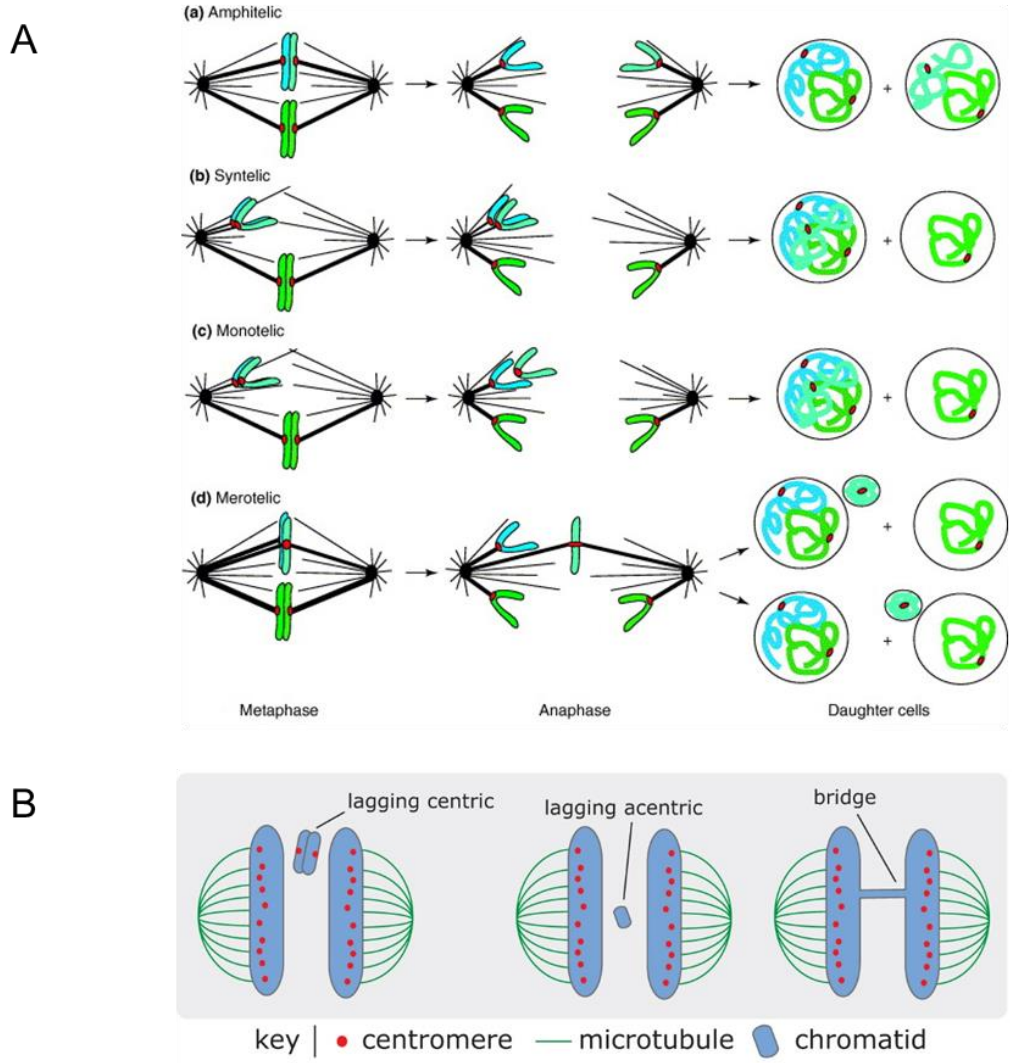

Figure 7 Errors in kinetochore–microtubule attachments and chromosome segregation. *(A) Types of kinetochore–microtubule attachment at metaphase, and subsequent consequences at anaphase and interphase. These KT-MT attachments includes amphitelic attachment, syntelic attachment, monotelic attachment and merotelic attachment. (B) Errors in chromosome segregation. Lagging centric chromosomes are identified as the whole chromosomes, while acentric chromosomes are chromosomal fragments without centromeres. Chromatid bridge is formed by the fusion of telomeres of sister chromatids, resulting in structural rearrangements of chromosomes. Centromeres are shown in red, microtubules are shown in green and chromatids are shown in blue. Modified from cartoons of McClelland, and Degrassi et al.*[27,28].

Kinetochores could also be attached by microtubules from opposite poles, known as merotelic attachment, leading to lagging chromosomes (Fig. 7A) [28]. While lagging chromosomes mainly arise from errors in mitosis, acentric chromosome arms (known as chromosomes without centromeres), as well as chromatid bridges, are caused by pre-mitotic defects and are associated with structural chromosome rearrangements (Fig. 7B) [12]. Many studies suggested that the merotelic attachment, frequently occurring during early mitosis, is a more widespread cause of aneuploidy and can escape SAC detection [29,30]. As a consequence, lagging of anaphase chromosomes will occur, resulting in aneuploidy or micronuclei formation in daughter cells (Fig. 7A). These micronuclei could subsequently collapse and release DNA into cytoplasm.

Temporal regulation of spindle microtubule dynamics is essential to maintain genome stability [19]. With respect to this, two molecular mechanisms are coordinated to ensure precise chromosome segregation. Apart from the inherent centromere geometry against improper KT-MT attachment, another mechanism is that these previous persistent improper attachments are released by regulating activities of Kif2b and MCAK (Fig. 8). Aurora B kinase activity alteration,

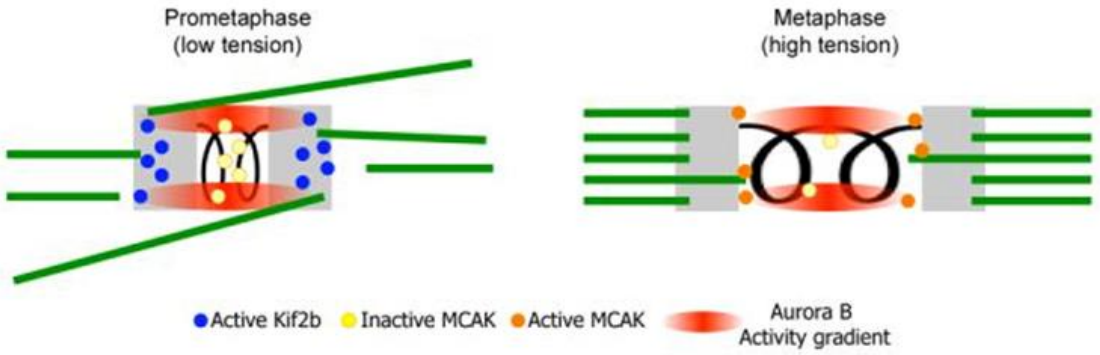

Figure 8 Model for temporal regulation of spindle microtubule dynamics by inter-kinetochore tension. *KT-MTs achieve gradual stabilization along following increased inter-kinetochore tension from pro-metaphase to metaphase. At pro-metaphase, low tension regulates the Aurora B kinase activity gradient to recruit active Kif2b and then inactivate the MCAK, thereby destabilizing spindle MTs for the correction of improper kinetochore attachments. Upon metaphase, generation of high tension by bi-orientation attachments, exceeding the extent limit of the Aurora B kinase activity gradient, could release the Kif2b from kinetochores. In the meantime, a subgroup of MCAK is activated and localizes to centromere, correcting the remaining attachment errors. Kinetochores are shown in grey, microtubules are shown in green, active Kif2b is shown in blue, inactive MCAK is shown in yellow, active MCAK is shown in orange and activity gradient of Aurora B is shown in red. Kif2b: kinesin family member 2b; MCAK/ Kif2c: mitotic centromere associated kinesin* [19].

mediated by tension between sister kinetochores, could regulate KT-MT dynamics temporally to correct the maloriented KT-MT attachments regardless of the original attachments [30]. Low centromeric tension could promote microtubule destabilization to ensure sufficient correction for improper attachment till the high tension is generated upon bi-orientation at metaphase [19].

During anaphase, the microtubules responsible for appropriate chromosome attachments, are predicted to be less dynamic than the microtubule fibers moving chromosomes, ensuring fidelity of chromosome segregation [31]. Hence, kinetochore microtubules become progressively stabilized, and this is mediated by properly increased tension during pro-metaphase to metaphase progression [30]. In summary, maloriented attachment of chromosomes to spindle MTs and/or even subtile changes in spindle MT dynamics during mitosis may lead to chromosome mis-segregation, CIN and aneuploidy.

1.3 Microtubule-targeted drugs in CRC treatment considering genomic diversity

Since cell mitosis is essential for cellular function and survival, mitotic spindle has already been a valuable target to treat a range of human cancers. Paclitaxel (PTX), a microtubule-targeted drug, could prevent MT depolymerization, thereby inducing a mitotic arrest through the activation of SAC. This type of mitotic catastrophe following spindle disruption probably is essential to initiate cellular apoptosis [32]. Nevertheless, taxane (PTX or docetaxel)-treatment of patients in early phase I-II CRC clinical trials, with CIN-positive cohort, failed to achieve a satisfied clinical benefit [33]. Interestingly, a minority group of CRCs in MSI+/CIN- cases, is suggested to response to PTX-therapy. This minority of CRCs may exhibit a different process of mitosis compared to CRC with CIN phenotype (CIN+) [32]. This assumption is consistent with a previous finding, showing that HCT-116 cell line (MSI+/CIN-) showed a potent mitotic arrest in response to paclitaxel treatment followed by apoptosis. In contrast, HT-29 cell line ((MSI+/CIN-) did not respond to PTX treatment [34]. Therefore, the resistance to taxane-based chemotherapies in CRC could be explained by the fact that most CRC cases are CIN+ tumors, and the mitotic spindle is an efficient target for the microtubule inhibitors (MTI) mediated cell cytotoxicity.

As mentioned above, cytotoxic chemotherapy resistance of CRC is associated with CIN+ phenotype. This issue could be promoted by generation of genomic and phenotypic diversity mediated via three possible pathways, that is innate, adaptive and acquired chemo-resistance pathways (Fig. 9) [27]. Comparing to adaptive resistance, in the presence of high intrinsic genomic

variation, acquired resistance is due to the generation of genetic diversity via CIN during chemotherapy treatment. Therefore, a sub-clone exhibiting resistance to chemotherapeutic agents will probably be promoted by this mutated phenotype in cancer cells [27]. We have described the

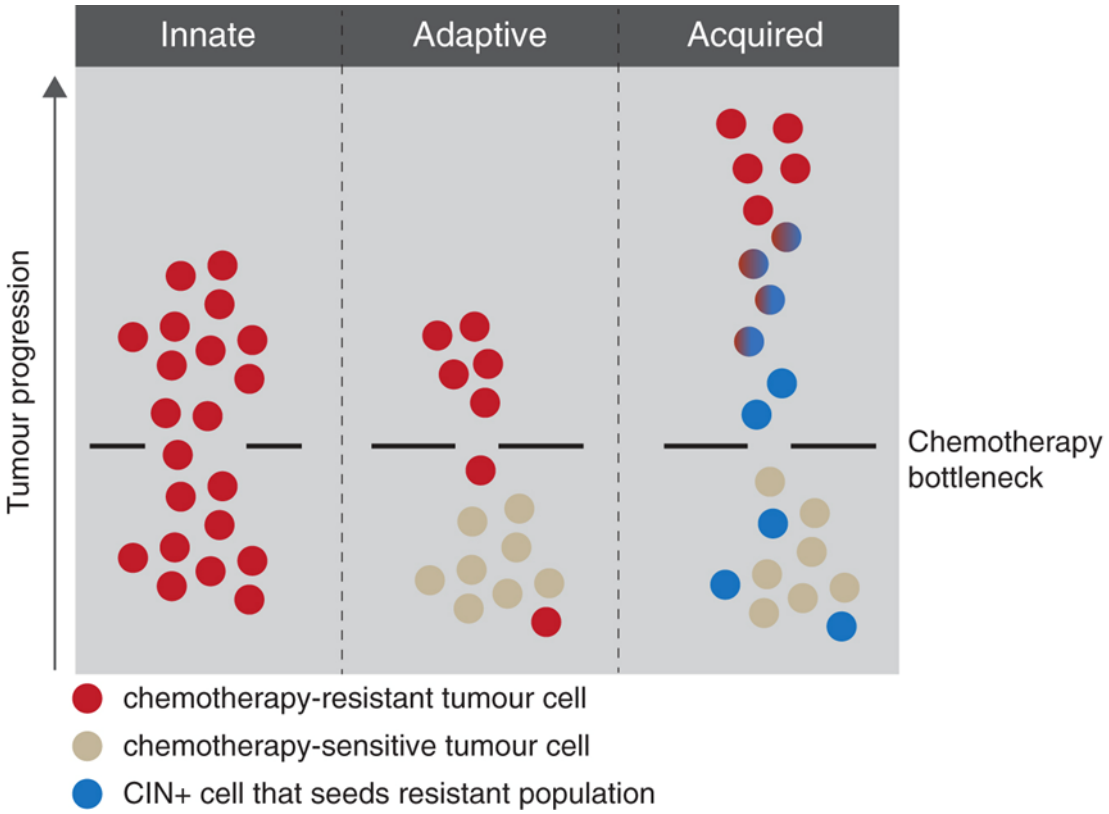

Figure 9 Schematic diagram of three major pathways to chemotherapy resistance. *Innate resistance is the inherency of tumor cells to tolerate chromosomal instability and probably even the chemotherapy agents, allowing tumor growth and progression. Due to high initial chromosomal diversity prior to chemical agents, a subgroup of cells intrinsically carrying the drug resistance are very likely to achieve the adaptive resistance, continuing to grow in the presence of chemotherapeutic agents. Acquired resistance occurs when a subset of cells achieving the drug resistance are generated during cancer treatments, and this resistance does not exist prior to treatments. This process may be promoted by a mutant phenotype that can generate genetic diversity mediated via genome mutation or rearrangements, such as CIN. Chemotherapy-resistant tumor cells are shown in red; chemotherapy-sensitive tumor cells are shown in brown; CIN+ cells with potential resistance are shown in blue.* [27]

association of spindle MT dynamics with CIN in section 1.2, as well as a correlation between CIN phenotype and taxanes resistance in CRC. Taken together, spindle MT could be a potent therapeutic target in reducing genomic diversity in both intrinsic and extrinsic way. During mitosis, spindle MTs could become progressively stabilized as described in section 1.2, and this dynamic is regulated by a series of microtubule-associated proteins (MAPs), with kinesin-related molecular motors well-studied [35]. The assembly/disassembly behavior of microtubules is

known as dynamic instability, driven by GTP hydrolysis (Fig. 10), and the growing and shrinking microtubules could co-exist in the same cell area [25,35]. In addition, this dynamic instability could result in chromosomal diversity, and even tumor tolerance against cytotoxic chemotherapies as mentioned in last paragraph. Since MAPs could regulate the dynamics of spindle MTs, they probably also account for the type of KT-MTs attachment or the speed of kinetochore fiber movement. Hence, signaling activities and/or expression levels of MAPs are likely associated with occurrence of CIN, and even chemotherapy sensitivity. Considering the facts that spindle

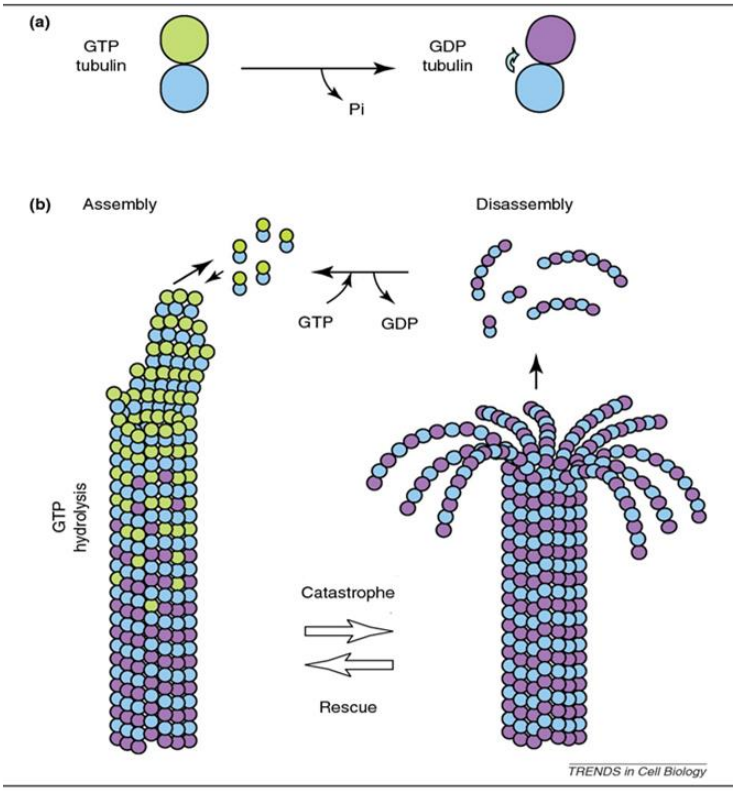

Figure 10 Cartoon of MT dynamic instability driven by GTP hydrolysis. *(a) Conformational switch of αβ-heterodimers accompanying by cycles of GTP hydrolysis. In the GDP state, the interface of αβ-tubulin dimer achieves a slight curvature (indicated with curved arrow) from the straight status in the GTP state. (b) The transitions between MTs assembly and disassembly at the plus ends. Physiologically, GTP-tubulin dimers (shown in green) assemble on the MT plus ends along with GTP hydrolysis, and this process is termed rescue event. In the catastrophe phase, GDP-tubulin dimers (shown in blue) curl and peel off the plus ends, starting the MT shrinkage.* [25]

MTs have already been used as targets for many chemotherapeutic drugs, continued investigation of proteins, specifically regulating spindle MTs dynamic, will be promising targets for cancer therapies.

1.4 Cellular roles of DIAPH1

Mammalian Diaphanous (mDias)-related formins are encoded by the DIAPH1/DRF (diaphanous-related formin) genes and are directly stimulated by Rho GTPases [36]. These Rho proteins are Ras-related GTP-binding proteins, switching between inactive/active GDP/GTP-bound cycles. [37]. DIAPHs are dimeric multi-domain proteins with characteristic of highly conserved C-terminal homology 2 domain (FH2) and include three subtypes: DIAPH1 (DFR1 or mDia1), DIAPH2 (DRF2 or mDia3) and DIAPH3 (DRF3 or mDia2) [36,38]. By regulating the dynamics of cytoskeleton, they participate in abundant cellular functions, and exhibit activities of actin filament nucleation and microtubule stabilization. These effects were achieved by the activities of two conserved regions of homology, FH1 and FH2 (Fig. 11) [39].

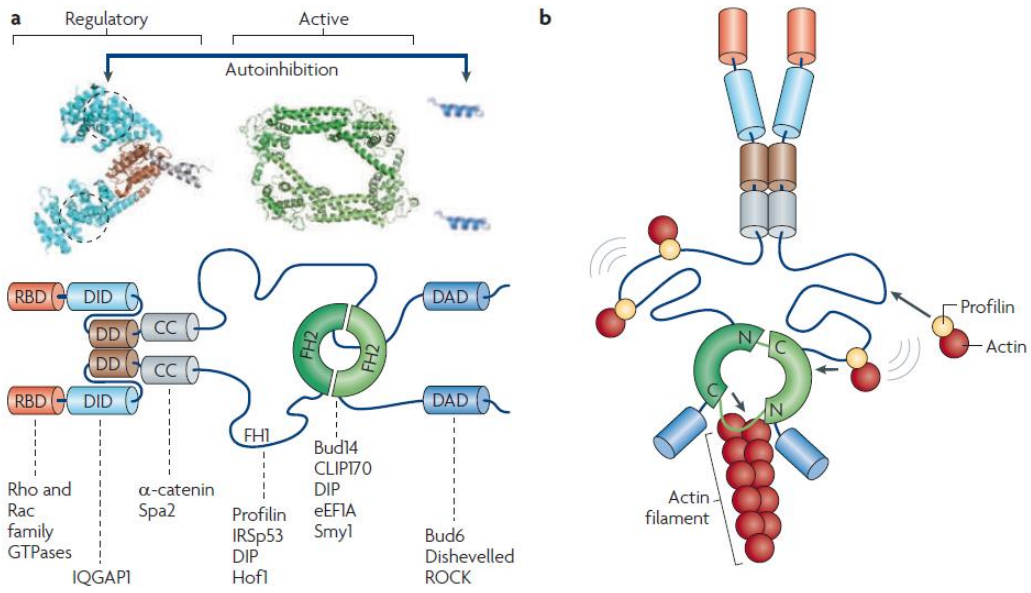

Figure 11 Scheme of DIAPH domains in regulating actin nucleation. *Dia-inhibitory-domain (DID) and diaphanous autoregulatory domain (DAD) interact and prevent binding of profilin/actin to the FH1 and binding of F-actin to FH2 domains. After binding of GTPases of the Rho family, the interaction of the DID and DAD domain is disrupted and the FH1/FH2 domains are released [38].*

Without activated signaling, diaph proteins are in an auto-inhibited form, as a result of the interactions of Dia-inhibitory domain (DID) and diaphanous auto-regulatory domain (DAD). This inactive conformation could be released, mediated by ionic repulsion and steric clashes, in presence of Rho GTPases [37]. In this case, the FH1 domain binds and recruits actin monomers (globular actin or G-actin), to uncapped F-actin, and thereby facilitate actin nucleation (Fig. 11) [38].

Although DAD-DID interactions can be abrogated by binding of Rho to the Rho-binding domain (RBD), under certain conditions, cells require extra cellular factors for the activation of formins [38].

In addition, these formins play a vital role in the regulation of MT-dynamics. Palazzo et al. revealed that DIAPH3 localized to stabilized MTs, and its active conformation exhibited an effect of stabilizing MTs in fibroblasts [40]. Furthermore, this MT-stabilizing effect was independent of its effect of actin polymerization [41]. In some cell lines, like Hela cells, DIAPH1-mediated nucleation of MTs and F-actin is spatially coordinated [42]. DIAPH proteins are also associated with the regulation of mitotic spindle dynamics. It is well studied that DIAPH2 regulated the dynamics of spindle MTs through binding of its FH2 domain to centromere protein A (CENP-A) in a cdc42 manner [43]. This activity was essential to align chromosomes at the spindle equator [43,44]. In consistent with this, our previous research showed that the activity of DIAPH2 is essentially involved in the control of chromosomal alignment by regulating spindle MT dynamics in colorectal cells [45]. In summary, DIAPH formins control MT dynamics in both interphase and in mitosis.

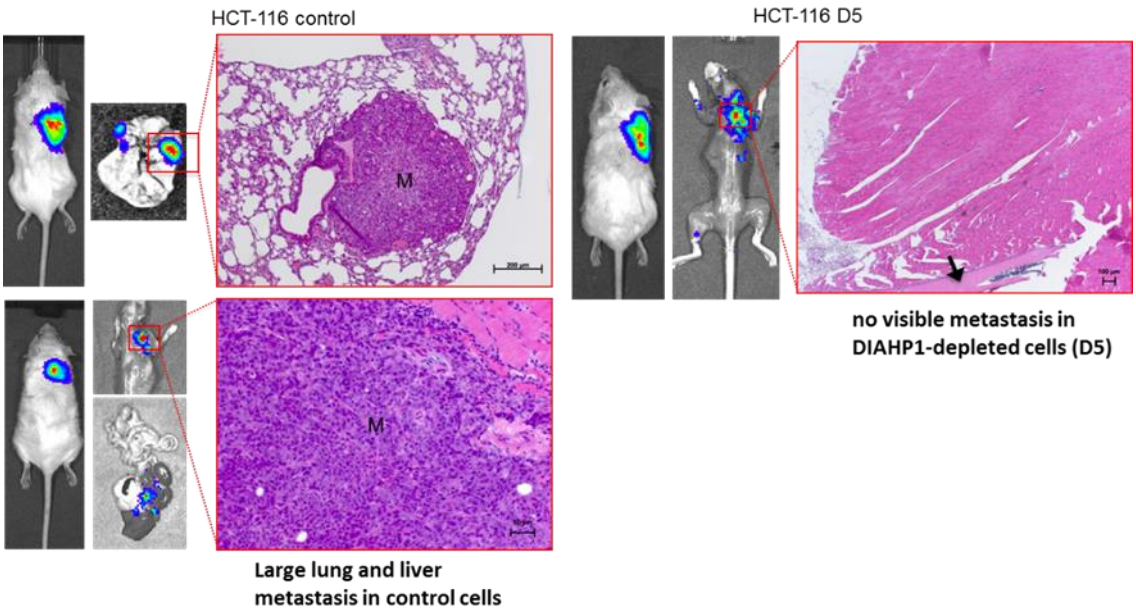

Figure 12 Reduced metastasis in SCID mice injected with HCT-116 DIAPH1 depleted cells. *In SCID mice injected with luciferase-over-expressing HCT-116 DIAPH1-depleted (D5) cells, histological examinations did not show any metastatic cells at different potential metastatic locations, such as lungs and livers. In contrast, the bioluminescence imaging (BLI) analysis showed strong signals at different distant locations in the mice injected with HCT-116 control cells. Moreover, the histological examinations of corresponding tissues showed abundant CRC cells (indicated as "M") in both lungs (upper panel) and livers (lower panel) respectively* [46].

Under physiological conditions, DIAPH formins are mainly expressed in immune cells, in which they are crucially associated with the formation of filopodia, invadopodia and pseudopods [47,48]. Interestingly, expression levels of DIAPH formins were upregulated in tumor cells and they exhibited clinical relevance for various cancer types, including oral squamous cell carcinoma, CRC, ovarian cancer, head and neck/laryngeal squamous cell carcinoma [46,49–51].

Among these three members of diaphanous proteins, DIAPH1 has been well investigated by our group. Lin et al. found that DIAPH1 is up-regulated in CRC, and depletion of DIAPH1 nearly completely blocked metastasis from neck to lung and liver in SCID mice (Fig. 12). It has

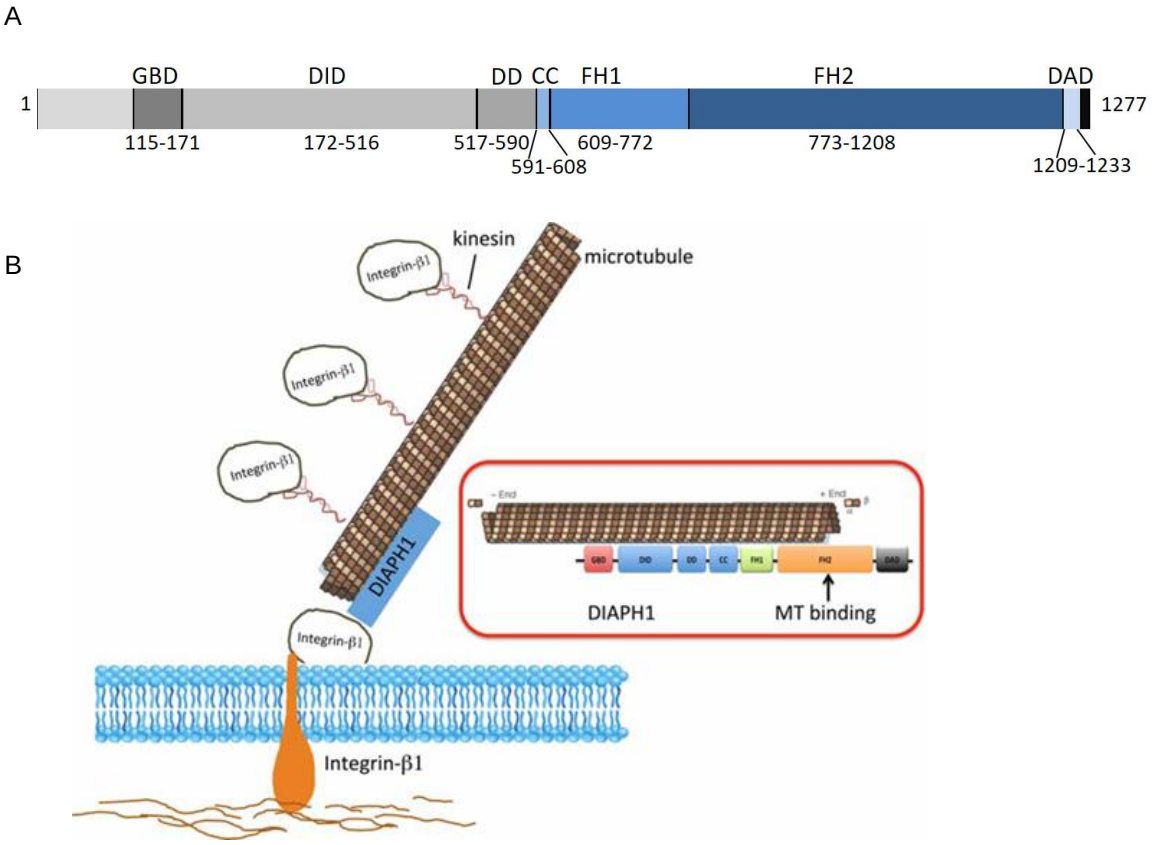

Figure 13 Scheme of DIAPH1 domains and its binding to microtubules. *(A) Scheme of DIAPH1 domains. GBD: GTPase binding domain, DID: Diaphanous Inhibitory Domain domain, DD: Dimerization Domain. CC: Coiled Coiled, FH1: Formin homology do-main 1, FH2: Formin homology domain 2, DAD: Diaphanous Autoregulatory; (B) DIAPH1 promotes cellular adhesion by stabilizing MTs. The DIAPH1 could bind to MTs via the FH2 domain, and facilitate MT stabilization even in absence of RhoGTPases. This activity enhances the transport of integrin beta containing vesicles to the plasma membrane, which is essential for the tumor cell adhesion to the extracellular matrix (ECM)* [52].

been also shown that depletion of DIAPH1 reduced adhesion, migration and transmigration in CRC cells [46]. Furthermore, it was found that DIAPH1 promoted cellular adhesion by stabilizing

interphase MTs, most likely by direct binding of the FH2 domain to MTs (Fig. 13B) [52]. Scheme of DIAPH1 domains is shown in Figure 13A.

1.5 Aim of the project

Our previous data indicated that DIAPH1 is essential to regulate the dynamics of interphase MTs in HCT-116 cells [45], hence it was interesting to analyze whether DIAPH1 may also control spindle MT dynamics and thereby CIN in CRCs. Based on this consideration, aim of this project was to elucidate the role of DIAPH1 in spindle MT-dynamics and CIN in chromosomally stable HCT-116 and unstable HT-29 cells.

2 Material

2.1 Plasmids

Table 2 used plasmids

Plasmid name	**Bacterial resistance**
pGem Teasy	Ampicillin
pGEX-6P-2A DIAPH1	Ampicillin
pGEX-6P-2A DIAPH1 FH2	Ampicillin
pGEX-6P-2A DIAPH1 dFH2	Ampicillin
pSF421_10× His_GFP_DIAPH1	Ampicillin
pSF421_10× His_GFP_DIAPH1 FH2	Ampicillin

2.2 Primers

Table 3 used primers

Primer name	**Binding location**	**Primer sequence**
pSF421_DIAPH1 FW	GFP-DIAPH1 gene (forward primer)	gctgatggaatctttattttcagggcca-ttcaatggagccgcccggc
pSF421_DIAPH1 RV	GFP-DIAPH1 gene (reverse primer)	caacagagtccaagctcgctaattaag-cttagcttgcacggcc
pSF421_FH2 FW	GFP-DIAPH1 FH2 gene (forward primer)	gatgagaatctttattttcagggccattca-atgcctccacctcccccatttg
pSF421_FH2 RV	GFP-DIAPH1 FH2 gene (reverse primer)	caacaggagtccaagctcagctaattaa-gcttgctctctcttctgctgcttctctagc
Primer 2071 FW	pSF421_10× His_GFP gene (forward primer)	gcttaattagctgagcttggactc
Primer 3855 RV	pSF421_10× His_GFP gene (reverse primer)	atggccctgaaaataaagattctc
DIAPH1 dFH2 FW	GST-DIAPH1 dFH2 gene (forward primer)	ctcatagacatgaatgcagagggcg
DIAPH1 dFH2 RV	GST-DIAPH1 dFH2 gene (reverse primer)	acccattccgggtggaggtg

2.3 Antibodies

Table 4 used antibodies

Primary antibodies			
Antibody	**Dilution**	**Fixation**	**Supplier**
Rb pAb to Detyro-sinated alpha Tubulin	1:200 in 1.25% BSA/0.03% Triton X-100/PBS (IF)	cold methanol	Abcam/ ab 48389
Polyglutamylation Modification mAb (GT335) mouse IgG	1:200 in 1.25% BSA/0.03% Triton X-100/PBS (IF)	cold methanol	AG-20B-0020C00
Beta Tubulin Polyclo-nal Antibody (Rabbit)	1:200 in 1.25% BSA/0.03% Triton X-100/PBS (IF)	4% PFA/4% Sucrose	Invitrogen (USA)/ PA5-16863
Monoclonal Anti-ß-Tubulin	1:200 in 1.25% BSA/0.03% Triton X-100/PBS (IF)	4% PFA/4% Sucrose	SIGMA/T4026
Rb pAb to DIAPH1	1:200 in 1.25% BSA/0.03% Triton X-100/PBS (IF)	4% PFA/4% Sucrose	Abcam/ ab11173
Ms mAb to CENPA	1:200 in 1.25% BSA/0.03% Triton X-100/PBS (IF)	4% PFA/4% Sucrose and cold methanol	Abcam/ ab13939
Secondary antibodies			
Antibody	**Dilution**	**Fixation**	**Supplier**
Alexa Fluor® 568 goat anti-mouse (H+L)	1:2000 in 1.25% BSA/0.03% Triton X-100/PBS (IF)	-	A11031
Alexa Fluor® 488 donkey anti-mouse (H+L)	1:2000 in 1.25% BSA/0.03% Triton X-100/PBS (IF)	-	A21202
Alexa Fluor® 568 goat anti-rabbit IgG (H+L)	1:2000 in 1.25% BSA/0.03% Triton X-100/PBS (IF)	-	ab 175471
Alexa Fluor® 488 goat anti-rabbit IgG (H+L)	1:2000 in 1.25% BSA/0.03% Triton X-100/PBS (IF)	-	ab 150077

2.4 Media

All media were prepared using Millipore water and autoclaved. For preparation of plates 1.5% (w/v) DifcoTM Agar (BD) was given to the medium

Table 5 Used media

Medium	**Ingredients**
LB Medium	2.5% (w/v) LB Broth (Luria/Miller) (Roth)
Medium for transfection of HEK-293 cells	OPTI-MEM®I (1×) Reduced Serum Medium (gibco) [+] HEPES [+] 2.4 g/L Sodium Bicarbonate [+] L-Glutamine
Medium for HEK-293 cells and HCT-116/HT-29 wt cells	10% FBS in DMEM (Gibco by LifeTechnologies)
Medium for HCT-116/HT-29 genome editing cells	10% FBS 1% Penicillin/Streptomycin Puromycin 2.0 µg/ml in DMEM (Gibco by LifeTechnologies)

2.5 Buffers, gels and other solutions

Table 6 Used buffer, gels and other solutions

Solution	**Ingredients**
1× Western transfer buffer	38.6 mM Glycine 47.9 mM Tris 1.3 mM SDS 20% (v/v) Methanol
1× SDS-PAGE running buffer	25 mM Tris 250 mM Glycin 3.5 mM SDS
1× PBS	137 mM NaCl 2.68 mM KCl 10 mM Na2HPO4 1.76 mM KH2PO4 PH to 7.4 with HCl
6× DNA loading dye	0.25% Bromphenol blue 0.25% Xylene Cyanol FF 30% Glycerol in water

4× SDS-PAGE loading buffer (Laemmli)	313 mM M Tris HCl (pH 6.8) 10% (w/v) SDS 0.05% (w/v) Bromphenol blue 50% Glycerol 500 mM DTT (add before usage)
Hyper Ladder I DNA ladder (1 kb or 100 bp)	10 µl 1kb or 100 bp DNA ladder stock (Bi-oLabs) 20 µl 6× DNA loading dye 90 µl H_2O
Fairbanks Solutions for Coomassie Staining	
Fairbanks Solution A (requires filtering)	0.05% Coomassie (500 mg/L) 10% acetic acid 25% isopropanol
Fairbanks Solution B	0.005% Coomassie (50 mg/L) 10% acetic acid 10% isopropanol
Fairbanks Solution C	0.002% Coomassie (20 mg/L) 10% acetic acid
Fairbanks Solution D	10% acetic acid
SDS-PAGE gel	Volume for 2-3 gels
10% Gel	4.8 ml H_2O 2.5 ml 40% acrylamide mix 2.5 ml 1.5 M Tris pH 8.8 0.1 ml 10% SDS 0.1 ml 10% APS 4 µl TEMED
8% Gel	5.3 ml H_2O 2.0 ml 40% acrylamide mix 2.5 ml 1.5 M Tris pH 8.8 0.1 ml 10% SDS 0.1 ml 10% APS 4 µl TEMED
Stacking gel	2.5 ml H_2O 0.375 ml 40% acrylamide mix 0.375 ml 1.5 M Tris pH 8.8

	30 µl 10% SDS 30 µl 10% APS 3 µl TEMED
1.0% Agarose gel	1.0% (w/v) agarose in 1× TAE buffer 1.0 µl ethidium bromide per 50 ml gel
1.25% BSA/0.03% Triton/PBS 12 ml	5% BSA:3 ml 10% Triton: 36 µl 1×PBS: 9ml
0.05% Tween/PBS 40 ml	0:05% Tween: 20 µl 1× PBS: 40 ml
2.5% BSA/0.5% Triton/PBS 6 ml	5% BSA: 3 ml 0.5% Triton: 300 µl PBS: 3 ml
Lysis Buffer 500 ml, pH 8.0 1× PBS 10% glycerol (not for NGC) 1 mM EDTA 1 mM DTT (before usage)	 50 ml 10× PBS 50 ml of pure glycerol 1 mM EDTA 500 µl 1 M DTT
Gefi running Buffer 500 ml, pH 8.0 20 mM HEPES 150 mM KCl 10% glycerol (not for NCG) 1 mM DTT (before usage)	 10 ml 1 M HEPES 75 ml 1 M KCl 50 ml of pure glycerol 500 µl 1 M DTT
Elution Buffer 10 ml, pH 8.0 1× PBS 10% glycerol 1 mM EDTA 1 mM DTT (before usage) 30 mM GSH	 50 ml 10× PBS 50 ml of pure glycerol 1 mM EDTA 500 µl 1 M DTT 0.09 g GSH powder
Buffer A 500 ml (for NGC system) 20 mM HEPES 150 mM KCl 35 µl ß-Mercaptoethanol (before usage)	 10 ml 1 M HEPES 75 ml 1 M KCl 35 µl ß-Mercaptoethanol
Buffer B 500 ml (for NGC system) 20 mM HEPES 150 mM KCl 500 mM Imidazol	 10 ml 1 M HEPES 75 ml 1 M KCl 100 ml 2.5 M Imidazol

35 µl ß-Mercaptoethanol (before use)	35 µl ß-Mercaptoethanol
Dialysis Buffer 3 L 20 mM HEPES 150 mM KCl 210 µl ß-Mercaptoethanol	 60 ml 1 M HEPES 450 ml 1 M KCl 210 µl ß-Mercaptoethanol

3 Methods

3.1 Biochemical methods

3.1.1 Cell culture

The cell line HCT-116 was obtained from the Deutsche Sammlung von Mikroorganismen und Zellkulturen (Braunschweig, Germany). HCT-116 cells were cultured in Dulbecco´s modified Eagle´s medium (DMEM, Gibco), supplemented with 10% (v/v) fetal calf serum (FCS) in the presence of streptomycin (100 µg/ml) and penicillin (100 units/ml). HT-29 DIAPH1 depleted cells were ready to use [50]. Cells stably expressing scrambled shRNA served as control. All in vitro data shown here were reproduced with two DIAPH1 shRNAs, the corresponding cell lines were termed D4 (DIAPH1 shRNA 4 knockdown) and D5 (DIAPH1 shRNA 5 knockdown). The DIAPH1 knockdown D4 and D5, and scrambled cell lines were additionally treated with 2.0 µg/ml puromycin for selection. Cells were cultured at 37°C in a humidified incubator with 5% CO_2.

3.1.2 Generation of HCT-116 DIAPH1 stably depleted cells

For the transfection of adherent cells, here 2.0×10^5 HCT-116 wild type (wt) cells, target cells were seeded into a single well of a 6-well cell culture plate in 2 ml DMEM complete medium and incubated at 37°C, 5% CO_2 overnight. The shRNA 4 and shRNA 5 (pLKO.1 shRNA) from Sigma, coding for shRNA against DIAPH1 were already tested as effective lentiviral vectors [46]. Viral particles (DIAPH1 shRNA 4 knockdown, DIAPH1 shRNA 5 knockdown, DIAPH1 scrambled shRNA) stored at -80°C and were thawed at room temperature (RT). The medium was aspirated from each well and replaced daily with 1 ml fresh medium containing 2 ml corresponding virus supernatant and 8 µg/ml Sequabrene for three days. Meanwhile, medium in control cells was also replaced with an equal amount of fresh and virus-free medium. The shRNA vector (pLKO.1-puro) has a puromycin-resistant gene, therefore the DIAPH1 knockdown D4 and D5, and scrambled cell lines were additionally treated with puromycin (2.0 µg/ml) for selection, and the selection was started at 72 h after infection. Untransfected HCT-116 cells were taken as negative control. Stable cell lines were established after two weeks of selection and were continuously grown in 2.0 µg/ml of puromycin afterwards.

3.1.3 SDS polyacrylamide gel electrophoresis (SDS-PAGE)

For protein analysis, polyacrylamide gel-based separation method is commonly used, known as Sodium-Dodecyl-Sulfate-polyacrylamide gel electrophoresis (SDS-PAGE). SDS-PAGE is used to separate denatured and reduced proteins from cell lysates primarily by their molecular weights within an electric field.

The SDS-PAGE gel can be divided into stacking and separating gel. To obtain optimal resolution of proteins, a stacking gel was cast over the top of the separating gel, and a gel comb was inserted into the stacking gel. The acrylamide percentage in SDS-PAGE gel was inversely related to the size of the pores and dependent on the size of the target protein in the sample (for instance, 8-10% acrylamide for DIAPH1 mixtures). Stacking and separating gel preparation (see the ingredients in table 6) were polymerized successively at RT for 30 min. Gels were then wrapped in wet tissue and stored at 4℃.

Afterwards, a lysate volume (section 3.1.5) containing 10-50 µg protein was transferred into a 1.5 ml tube. The required volume of 4× SDS-PAGE loading dye was added to the lysate, and then the mixture was boiled at 95°C for at least 5 min. Samples were then centrifuged at 2 000 rpm, 4℃ for 5 min and allowed to cooled down prior to transferring into the pockets of SDS-PAGE gels. To facilitate protein identification, 10 µl of a protein ladder (PageRuler TM Unstained High Range Protein Ladder Commassie dye (Themo Scientific, product#26637) was loaded as a protein marker. Ice cold SDS gel running buffer was filled up in both inner and outer chamber of the electrophoresis apparatus. SDS gels were subsequently run at 100 V for stacking gel (around 20 min) and 140 V for separating gel (around 1.5 h).

3.1.4 Bradford protein assay

The Bradford assay is a quick and accurate spectroscopic analytical procedure used to measure the concentration of proteins in a solution. The principle of this assay is the binding of protein molecules to Coomassie dye reagent (Bio-Rad Cat, LOT 5000006) under acidic conditions results in a color change from brown to blue.

Cells were gently harvested by trypsinization and rinsed once with 1× PBS. Subsequently, cells were pelleted by centrifugation (5 min, 4°C, 700 g) and lysed by 60-100 µl mammalian protein extraction reagent (M-Per, ThermoFisher, LOT 78501) with PI (Protease Inhibitor) and PS (Phosphatase Stop). The cell lysates were rapidly frozen at -80°C for 5 min and then thawed slowly on ice. The proteins were thereby extracted by centrifugation at 13 000 g for 15 min at

4°C. Protein standard were made through serial dilution using 0.1 mg/ml BSA solution, yielding BSA solutions of the following concentrations: 0.005 mg/ml, 0.01 mg/ml, 0.02 mg/ml, 0.03 mg/ml, 0.04 mg/ml and 0.06 mg/ml. Meanwhile, proteins were also prepared in a dilution of 1:200, and 50 µl of each sample was also pipetted in duplicate into the 96-well plate. 200 µl of coomassie dye reagent (1:50; Bio-Rad) were then added to protein standards and protein samples, and protein-dye mixtures were incubated for 5 min at RT to allow color to develop. Afterwards the absorbance in the preparations was measured at 595 nm using TECAN (infinite M200) to obtain the standard protein curve and the concentration of each protein sample.

3.1.5 Western blot analysis

Western Blot was used for the electrophoretic transfer of proteins from the SDS-PAGE gel onto nitrocellulose membrane and target proteins were visualized by decoration with specific antibodies. The gel/membrane sandwiches were assembled in the right order (sponge, filter paper-gel-membrane-filter paper, sponge), and then electrophoretic transfer took place in a transfer tank filled with cold transfer buffer (see the ingredients in table 6) under constant voltage (35 V), 2 h at 4℃, adding a magnetic stirring bar to ensure a gentle and effective mixing.

Afterwards the nitrocellulose membrane was blocked with 5% milk/0.1% TBS-Tween for 45 min at RT. After removal of the blocking solution, the primary antibody solution (diluted in 0.1% TBST with 5% milk, 1:1000-5000) was subsequently added to the membrane and incubated overnight at 4℃ on the platform rocking shaker. Following primary antibody incubation, the membrane was rinsed 3 times for 10 min with TBST on the shaker. Afterwards, corresponding secondary antibody solution (horseradish peroxidase (HRP)-linked, 1:5000) was added to the membrane and incubated for 1 h at RT with gentle agitation. The same washing steps took place as after incubation with first antibody solution. Subsequently, the whole nitrocellulose membrane was incubated with enhanced chemiluminescence (Amersham ECL Western Blotting Detection Reagent) for detection of HRP for 5 min.

Finally, the target protein on the membrane was detected as ECL signal (LAS 4000, FujiFilm, Raytest, Straubenhardt, Germany) and digital images of the autoradiograph were acquired with the protein marker. The band intensities representing target protein expression level were quantitated with reference to loading control bands (e.g. the heat-shock cognate 70) using the Fiji software.

3.1.6 Cell synchronization with double Thymidine Block

To enrich mitotic cells, cells were synchronized at G1/S boundary from distinct cell cycle stage using double thymidine block. For this purpose, 3.0×10^4 cells per 200 µl were seeded into single well of ibidi 8-well chambers (ibidi ®). After 8 h of growth, adherent cells were incubated for 16 h in the medium containing 2 mM thymidine (T1895-1G, Sigma-Aldrich) in humidity incubator. Thereafter, the replication block was removed by releasing the cells into fresh pre-warmed complete medium for 8 h. Cells were then again treated with 2 mM thymidine for another 16 h. Following the release into fresh medium for 7-7.5 h or 7.5-8 h, many cells were in metaphase or anaphase based on the purpose of research.

3.1.7 Cell fixation and immunostaining

To visualize chromosomal alignment, the cells were synchronized with a double thymidine block (see 5.1.6) and fixed with 4% paraformaldehyde/4% sucrose/PBS for 10 min at 37°C. After incubation with 0.3% Triton X-100/PBS at RT for 5 min, fixed cells were blocked in 2.5% BSA/PBS for 20 min at 37 °C. Without any washing step, primary antibodies against ß-tubulin (Sigma-Aldrich Cat# T4026) were applied to fixed cells in a dilution of 1:200 in 1.25% BSA/0.03% Triton X-100/PBS and incubated at 4°C overnight. On the following day cells were rinsed 3 times with 1x PBS and the primary antibody was coupled with an Alexa-fluor-conjugated 568 antibody (Jackson ImmunoResearch) in a dilution of 1:1000 in 1.25% BSA/0.03% Triton X-100/PBS (for 1 h at 37°C) in the dark. Cells were then rinsed 3 times in 500 µl 1x PBS for 10 min under gentle shaking followed by DAPI staining (4,6-Diamidin-2-phenylindol, ab11173 Abcam) in a dilution of 1:2000 in 1.25% BSA/0.03% Triton X-100/PBS for 10 min at 37°C in the dark.

For immunofluorescence analysis of cellular DIAPH1 colocalization in metaphase cells, cells were induced to mitotic arrest by a double thymidine block (see 5.1.6) and then fixed with 4% paraformaldehyde/4% sucrose/PBS, and subsequently stained with antibodies against ß-tubulin and DAPI as described above. On the following day cells were stained with DIAPH1 primary antibodies (ab11173, Abcam) (1 h, RT), coupled with an Alexa-fluor-conjugated 488 antibody (mouse, Alexa Fluor® 488 donkey anti-mouse IgG (H+L), A21202).

For fluorescence intensity analysis of cellular detyrosinated and glutamylated microtubules in metaphase cells, cells were synchronized by double thymidine block and then fixed with ice-cold methanol at -20°C for 5 minutes, followed by BSA-block (2.5% BSA/0.05% Triton-X-

100/PBS) for 1 h at 37°C. Firstly, the methanol-fixed cells were stained with antibodies against detyrosinated alpha-tubulin (ab48389, Abcam) or Polyglutamylation Modification mAb (GT 335, mouse IgG 1×, AdipoGen® Life Science AG-20B-0020-C100), then with antibod-ies against β-tubulin and DAPI as previously described for chromosome alignment analysis. The primary antibodies against detyrosinated or glutamylated tubulin should not be derived from the same species as that against ß-tubulin to reduce the non-specific background.

For analysis of chromosomes segregation, cells were synchronized in anaphase and fixed with 4% paraformaldehyde/4% sucrose/PBS for 10 min at RT, followed with cold methanol at -20°C for 20 min, and then with PBS-Tween (0.05% v/v) for 5 min at RT. Afterwards fixed cells were blocked to avoid non-specific binding by 2.5% BSA/0.5% Triton X-100/PBS for 20 min at 37°C. Anti-CENPA primary antibody (ab13939, Abcam, mouse) was applied to fixed cells in a dilution of 1:200 in 1.25% BSA/0.03% Triton X-100/PBS overnight at 4 °C. On the next day cells were incubated with anti-mouse secondary antibody (Alex-fluor-conjugated 488) in a di-lution of 1:2000, followed by staining with beta Tubulin Polyclonal Antibody (Invitrogen PA5-16863) and DAPI as described above. Between each staining step cells were washed 3 times with PBS-Tween (0.05% v/v) for 10 min with gentle agitation.

To compare the F-actin fluorescence intensities of DIAPH1 scrambled and DIAPH1 knock-down cell lines, cells underwent double thymidine block and fixed with 4% PFA/4%Su-crose/PBS. Thereafter cell membrane permeability was increased with 0.3% Triton X-100 and unspecific binding was blocked by 2.5% BSA/PBS. Afterwards, staining of fixed cells with ß-tubulin primary antibody was performed as above. The next day, cells were rinsed 3 times with 1× PBS and stained with phalloidin (Alexa-Flour®488) in a dilution of 1:2000 with 1x PBS for 30 min at RT.

Prior to imaging or storage, a final 3 times wash steps for 3 to 5 minutes in 1× PBS should follow. The stained cells were analyzed with the Keyence Microscope (Biorevo, BZ-9000), and fluorescence signals (microtubules, chromosomes, DIAPH1, detyrosinated microtubules, glu-tamylated microtubules and CENP-A, phalloidin) of samples in corresponding emission chan-nels were detected and documented based on corresponding assay requirements. After subtract-ing the background, fluorescence intensities of F-actin were quantified by ImageJ (Fiji) and comparable F-actin intensities were controlled with reference to nucleus intensities.

3.1.8 Chromosome preparation and staining

As soon as cells were detached from the culture flask, 2 ml of the cell suspension were seeded in 10 cm dish and kept in a humidified incubator at 37°C with 5% CO_2 for 6 h. Afterwards cells were incubated with 0.06 µg/ml colchicine overnight to induce metaphase arrest. On the next day, the treated cells were harvested with trypsin and resuspended in medium, engorged slowly with cold 75 mM potassium chloride (KCl) hypotonic solution and then incubated on ice for 10 min. After centrifugation for 5 min at 1 200 rpm at 4°C and removal of supernatants, engorged cells were fixed slowly with cold Carnoy's fluid fixation (cold methanol and acetic acid mixture (3:1)) twice. Microscope slides (not HistoBond® slides) were pre-coated with a thin layer of distill water. Fixed cells (20-50 µl) were dropped onto the slide from a height of 30 cm, and then cells were swelled and burst open because of lower extracellular osmotic pressure. When the slides were completely air dried, chromosomes on the slides were stained with cold Giemsa solution (Sigma-ALDRICH) in a dilution of 1:5 with cold PBS for 15 min, washed once with tap water and thoroughly dried again. Alternatively, chromosomes were mounted using the DAPI-containing mounting medium (VECTASHIELD®Antifade Mounting Medium). The slides containing stained chromosomes were then placed on the stage of digital microscope (Keyence, Biorevo, BZ-9000) and fluorescence images were documented.

3.1.9 Micronucleus Test

After cell harvesting with trypsin-EDTA solution, 2 ml of the cell suspension were placed in a 10 cm dish and incubated overnight. Then cells were harvested and fixed as described in the section of chromosome preparation. Instead of dropping down from high distance, 30-50 µl fixed cells were smeared directly over the pre-cleaned and uncoated microscope slides with a pipet tip (100 µl ClearLine Tip). When the slides were completely air dried, chromosomes on the slides were stained and imaged as mention in the chromosome preparation section. Cells with micronucleus were recorded. 2 000 cells per cell line for one experiment were analyzed and two different experiments were done.

3.1.10 Proliferation and MTS assay

Proliferation was examined by image analysis, measuring the cell confluence, and using the software IncuCyte Zoom 2016B (Essen BioScience). 100 µl of cells suspension/well (HCT-116 DIAPH1 cell lines: 5 000 cells; HT-29 DIAPH1 cell lines: 2 500 cells) were seed with a multi-

channel pipette (Finnpipette® Labsystems E84170, 50-300 µl) in 96-well flat-bottom transparent microplates (Greiner, CELLSTAR® 655180) and kept at 37°C in the 5% CO_2 humidified incubator overnight. On the following day, related parameters of the software program were set up beforehand and the 96-well plate was placed into the device when the scanning sys-tem did not start to scan for the next 30 min. The interval of time between cells seeding and scan of the system in different assay should be kept similar. Cell proliferation curves were automatically plotted by the software, reflecting the corresponding confluence of the cells at different time points (24 h, 48 h, 72 h, 96 h). The adjustment of the confluence mask for the cell lines in different assays should be kept the same.

MTS(3-(4,5-dimethylthiazol-2-yl)-5-(3-carboxymethoxyphenyl)-2-(4-sulfophenyl)-2H-tetrazolium) assay is a colorimetric assay for assessing cell metabolic activity by producing a formazan product, reduced by NAD(P)H-dependent oxidoreductase enzyme in mitochondria in living cells. Cells were seeded in triplicate into 96-well microplates at a density of 2.5×10^3 cells per well in 100 µl, and media were added to one well per plate as blank sample. Cells were cultured overnight at 37°C in an atmosphere of 5% CO_2. On the following day, 20 µl of the MTS Reagent (CellTiter96® A Queous One Solution Cell Proliferation Assay, Promega, G3580) were pipetted into each well of the 96-well assay plate, air bubbles should be avoided. After 1.5 h incubation at 37°C, the absorbance of the treated cells was measured at 490 nm using absorbance-based plate reader (TECAN, infinite M200). Cells viability was assessed by the scatter diagram consisting with serial plots of the absorbance in corresponding time points.

3.1.11 Live cell imaging for spindle MT-dynamics

To compare spindle MT-dynamics between control and DIAPH1 knockdown cell lines using live cell imaging, cells were seeded at 3.0×10^4 cells/well in 8-well chamber slide (ibidi ®) and synchronized with a double thymidine block as described in 3.1.6. Following the release from the second thymidine block, the cell culture medium was replaced with 200 µl pre-warmed fresh medium containing 0.5 µM SiR-tubulin (SCOO2; SiR-tubulin kit)), and synchronized cells were incubated for 4 h in standard cell culture incubator. Afterwards, the cells were stained with 50 ng/ml Hoechst to stain nuclei and kept in the dark. The spindle MT-dynamics was evaluated by the speed of the spindle microtubules movement (µm/h) using the Vision Spinning-disk confocal microscopy (confocal 640), which is an imaging technique and provides high-resolution imaging by combing the out-of-focus light rejection of confocal microscopy with the high sensitivity of wide-field microscopy. The spindle MT-dynamics between different

cell lines were compared at the same time points, and the com-mon intermediate time point was at the metaphase to anaphase transition.

3.1.12 Measurement of caspase 3/7 activities

To measure the cell apoptosis, 2 $\times 10^4$ cells/well were seeded on a Corning® 96 well white microplate (tissue culture treated, LOT 09020056) in 100 µl. Cells were seeded in triples for each measurement, with a blank control group (containing completed medium) and positive control group (containing paclitaxel), and incubated at 37°C in a humidified incubator with 5% CO_2. On the following day, Caspase-Glo® 3/7 Reagent (mixtures of Caspase-Glo® 3/7 Buffer and Caspase-Glo® 3/7 Substrate, Promega, G8091), as well as the white plate, was equilibrated to RT. Afterwards, cell culture medium was aspirated and replaced by 100 µl reagent (in a twofold dilution using growth medium). The plate was then put onto the plate shaker, wrapped in silver paper, and cells were incubated for 30 min with 350 rpm shaking at RT. The signals of luminescence, which is ex-pressed as relative light units (RLUs), were measured by TECAN reader (as mentioned in section 3.1.10). With respect to the positive control, HCT-116 cells were treated with 10 nM paclitaxel (Sigma-Aldrich, T7402), while HT-29 cells were exposed to 5 µM paclitaxel. Cells were added with Caspase-Glo® 3/7 Reagent and the measurements of RLUs were repeated at 24 h, 48 h and 72 h after treatment with paclitaxel. To achieve the real RLUs values of each cell line, the RLUs blank was subtracted. To compare the differences of RLUs values between DIAPH1 scrambled and knockdown cells, the RLUs data at different time points were normalized to the RLUs values at 24 h after paclitaxel treatment for corresponding cell line.

3.1.13 Paclitaxel treatment of CRC cells

To compare the sensitivities of CRC cells to paclitaxel, cells were seeded on 96-well transparent microplates at a density of 2 $\times 10^4$ cells per well in 100 µl complete growth medium. Following overnight incubation, the optical density (OD) values were measured using MTS assay as described in section 3.1.10. Afterwards, cells were treated with a range concentrations of paclitaxel. While HCT-116 cells were exposed to paclitaxel (0 nM, 0.5 nM, 1 nM, 5 nM, 7 nM, and 10 nM), HT-29 cells were treated with different concentrations of paclitaxel at 0 µM, 0.5 µM, 1 µM, 2 µM, 5 µM and 10 µM. The absorbances of these treated cells were measured at 24 h, 48 h and 72 h after adding the paclitaxel as described above. Before analyzing the OD values of each cell line, the values of growth medium should be subtracted. To compare the differences of OD data between DIAPH1 control and knockdown cells, the OD values of cells

without paclitaxel treatment should be subtracted. Then the OD values at different paclitaxel concentrations were normalized with the OD data of 24-hour paclitaxel treatment (0 nM).

3.1.14 Quantification of mRNA levels for IFNs by RT-qPCR

For quantification of mRNA levels, RNA was extracted from fresh cell lysates with the NucleoSpin RNA Kit (MACHEREY-NAGEL). Prior to RNA extraction, all working surfaces, pipettes, equipment must be routinely cleaned with RNase cleaning agent (RNase ZAPTM, SIGMA® Life Science® R2020), and spits were carefully avoided.

Cells were harvested with trypsin, resuspended in used media and washed once with ice cold 1× PBS. After centrifugation at 700 g, 5 min at 4 °C, cell pellets were lysed by the mixture of 350 µl RAI (lysis buffer, LOT 79743) and 3.5 µl β-ME (ß-Mercaptoethanol) with enough vorticity. Cell lysates were then filtered with purple filter (NucleoSpin® Filters, LOT SPI002340), and the collected flow-through was mixed with 350 µl 70% ethanol by gently pipetting up and down (5 times) to adjust the RNA binding condition. Following centrifugation at 11,000 g, 30 s at 4°C, RNA was bound to the RNA affinity column (NucleoSpin® RNA Columns, LOT SPB002382), and 350 µl MDB (Membrane Desalting Buffer, LOT 79753) was added onto the column to desalt the silica membrane. To digest the DNA, 95 µl DNase (1:10 dilution with reaction buffer) were added directly to the desalted silica membrane and incubated for 15 min at RT. The silica membrane was then washed once with RAW2 buffer (wash buffer, LOT 79209) and twice with RA3 buffer (wash buffer, adding 48 ml ethanol before first use, LOT 79797). Subsequently, RNA on the membrane was eluted with 60 µl RNase-free H_2O with a 5 min incubation time.

The concentration of extracted RNA was determined photometrically using RNA program in Nanodrop (Peqlab), and RNA purified quality was evaluated by the ratio of the absorbance at 260 nm and 280 nm (A260/280 should be around 2.0). 2 µg of total RNA were reverse transcribed into DNA with 400 U SuperScript III Reverse Transcriptase (Invitrogen, Cat no. 18080-093). The remaining RNA was stored in the -80°C freezer. The mixture of 2 µg RNA and 1 µl 50 µM Primer/Oligo dT were diluted to 18.5 µl with nuclease-free H_2O and incubated 10 min at 70°C. Afterwards, reverse transcription mixture (6 µl 5× buffer, 6.7 mM DTT, 0.5 mM dNTPs and 2 µl 200 U/µL superscript (SSIII)) were added to RNA mixture and incubated for 1 h at 42°C.

Quantitative RT-PCR analysis was carried out on the QuantStudio™ 3 System (Applied Biosystems) using the Mastermix. Samples (cDNA of DIAPH1 scrambled and knockdown cells, nuclease-free water) were applied in triplicate and mixed with corresponding targets (interested mRNA primer and GAPDH primer). The reaction mixtures (5 µl buffer, 1.5 µl 3 nM forward/reverse primer, 1 µl nuclease-free H_2O and 1 µl cDNA) were applied into sterilized 96-well microplate, 96-well plates were sealed tightly with plate sealer (MicroAmp™ Optical Adhesive Film, applied biosystems® by Thermo Fisher Scientific, Abcam, 4311971) and spun down by centrifugation for 1 min at 1 100 rpm. Afterwards QuantStudio™ 3 System was started for running the qPCR reactions. Data were analyzed with the QuantStudio™ Design & Analysis software based on the comparative ΔΔCt method with the cDNA from DIAPH1 scramble cells as a reference sample, nuclease-free H_2O serving as a negative control and mRNA levels of GAPDH serving as an internal reference. All designed qPCR primers were searched in databases to amplify target mRNA between 90 and 200 bp. Exon-spanning primers were used to avoid intron amplification.

3.1.15 Human Cytokine Array (Proteome Profiler™ Array)

Cells were harvested and lysed as previously described for western blot analysis in 3.1.5, and concentrations of protein mixtures were determined by Bradford assay as described in 3.1.4.

Human Cytokine Array membrane were blocked with 2.0 ml Array Buffer 4 in 4-well Multi-dish for 1 h at RT on a rocking platform shaker, the array number should be facing upward. Meanwhile, 1 ml cell lysates were diluted into 1.5 ml solution with Array Buffer 4 and then mixed with 15 µl reconstituted Human Cytokine Array Detection Antibody (reconstituted in 100 µl distilled water), incubated for 1 h at RT on the shaker. After the removal of Array Buffer 4 from the 4-well dish, the blocked nitrocellulose membranes were incubated with sample/antibody mixtures in a plastic container on the rocking shaker overnight at 4 °C in the fridge. The mixtures of cytokine (from the cell lysates) and antibody would be bound by its cognate immobilized capture antibodies, which were spotted in duplicate on the membrane. Following a total of 3 washing steps with 20 ml 1× wash buffer for 10 min per time, mem-branes were returned back to the 4-Well Multi-dish with flat-tip tweezers and then incubated with 2.0 ml Streptavidin-HRP (diluted with Array Buffer 5 in 1:5 000) for 30 min at RT on the rocking shaker. After 3 times washing as described above, nitrocellulose membranes were incubated with 1 ml of the chemiluminescent detection reagents mixture for 1 min at RT. Chemi Reagent 1 and 2 should be mixed in equal volumes, protecting from light, within 15 minutes of use. Target cytokines

on the membrane were exposed to X-ray film for 1-10 minutes, and the expression levels of cytokines were detected as ECL signal (LAS 3000, FujiFilm, Raytest, Straubenhardt, Germany). Multiple exposure times were recommended.

The average pixel density of the duplicate spots in the array was quantified with ImageJ (Fiji) by subtracting an averaged background signal (negative control spots).

3.2 Microbiological and molecular biological methods

3.2.1 Phusion PCR

For the amplification of specific DNA sequences, Phusion PCR (Polymerase Chain Reaction) was used. The following components (table 7) were transferred into a 0.2 ml microcentrifuge tube, keeping on ice, and then thermocycled (table 8).

Table 7 Components for Phusion PCR

Volume	Component
10.0 µl	5× Q5 Reaction buffer
10.0 µl	5× GC enhancer
1.0 µl	dNTPs (10 mM)
1.0 µl	Template DNA (10 ng/µl)
1.0 µl	Forward Primer (10 µM)
1.0 µl	Reverse Primer (10 µM)
0.5 µl	Q5 High-fidelity DNA Polymerase (1 kb/20-30 s), (2U/µl)
Add nuclease-free water up to 50 µl.	

Table 8 Thermocycler program for Phusion PCR

Step	Time	Temperature	
Initial Denaturation	30 s	98°C	
Denaturation	15 s	98°C	30×
Primer annealing	30 s	55-65°C	
Elongation	1 kb/20-30 s	72°C	
Final elongation	5 min	72°C	
Hold	permanent	4°C	

3.2.2 Agarose gel electrophoresis

For separation of a mixed population of DNA fragments by length, agarose gel electrophoresis was supposed to be the most effective way. 10 µl DNA loading dye (6×, Thermo Scientific) was added to 2 µl DNA sample, and then the mixture was applied into the pocket of 0.8% (w/v) agarose gel, containing 0.2 µg/ml ethidium bromide. 10 µl Hyper Ladder I (Bioline) was used as marker. Afterwards, the electrophoresis tank was filled up with 1× Tris-Acetate-EDTA-Buffer (TAE, SERVA; LOT 07026) and DNA fragments were run on the agarose gel at 80-100 V for 1 h. DNA fragment bands were then detected using an ultraviolet (UV) transilluminator, and the fragment sizes were determined by comparing to known marker fragments. Under UV light detectable DNA bands were cut out from the gel and DNA was extracted using the NucleoSpin® Gel and PCR Clean-up Kit (Macherey-Nagel) according to the manufacture's instruction.

3.2.3 SLIC reaction

The method of sequence- and ligation-independent cloning (SLIC) uses an exonuclease, T4 DNA polymerase, to generate single-stranded DNA overhangs in insert and vector sequences. These fragments are then assembled *in vitro* and transformed into *Escherichia coli* (*E. Coli*) to generate recombinant DNA of interest.

For amplification of vector DNA and insert DNA, the PCR with phusion hot-start polymerase was performed as described above. Afterwards, the target DNA fragments were checked by running an agarose gel and purified by the PCR Clean-up kit (as described in section 3.2.2).

To ligate the vector DNA into the insert DNA, following components were mixed in a 0.2 ml tube, keeping at RT, and T4 DNA polymerase was added in the last step.

Table 9 Ingredients for SLIC reaction

Volume	Component (10 µl)
1.0 µl	2.1 buffer NEB
X µl	Insert DNA
Y µl	Vector DNA
0.5 µl	T4 DNA ligase
to 10 µl	nuclease-free water
Start the 2.5 min incubation at RT immediately, then put the mixture on ice for 10 min to stop the reaction.	

The volume of linearized insert DNA and vector DNA used in the ligation was calculated based on the molar ratio of backbone to insert. (https://nebiocalculator.neb.com/#!/ligation)

After the SLIC reaction, the insert DNA is physically ligated to the backbone, and the complete plasmid could be transformed into competent cells for propagation.

The following work mapping described below shows how it works.

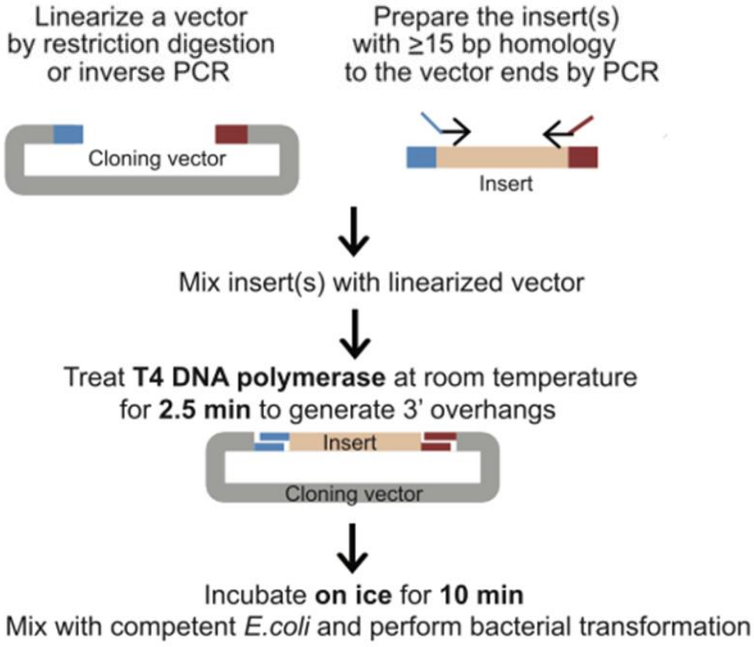

Figure 14 Scheme of the process of one-step SLIC . *Vector is firstly to be linearized by restriction enzyme of inverse PCR. In the meantime, inserts are prepared by PCR, with more than 15 base pairs (bps) homology to the vector ends. Afterwards, linearized vectors are mixed with prepared, and the mixtures are incubated at RT for 2.5 min, generating 3' overhangs with T4 DNA polymerase. The ratio between vectors and inserts are calculated (Table 9). DNA mixtures are then incubated on ice for 10 min and transformed into competent E.coli directly* [53].

3.2.4 KLD reaction

KLD Enzyme Mix (Q5 Site-Directed Mutagenesis Kit), containing blend of Kinase, Ligase and DpnI enzymes, allows rapid and efficient incorporation of insertions, deletions and substitutions into double-stranded plasmid DNA at RT.

The linearized target DNA sequences were prepared by phusion PCR (Table 8), and PCR products were checked and purified as described above. The following components were mixed in a 0.2 ml tube at RT.

Table 10 Components of KLD reaction

Volume	**Component (10 µl)**
5.0 µl	KLD reaction buffer (2×)
1.0 µl	PCR product
3.0 µl	nuclease-free water
1.0 µl	KLD enzyme mix
Incubate for 1 h at 37°C	

The following work mapping described below shows how it works.

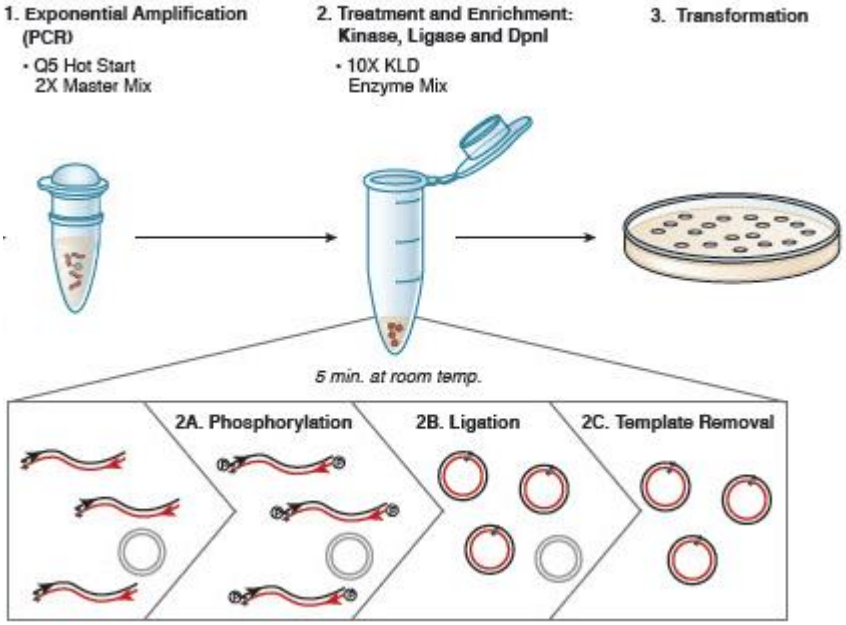

Figure 15 Scheme of the process of KLD reaction. *Exponential amplification of target DNA is performed by phusion PCR as described in section 3.2.1. Afterwards, the DNA product is incubated with KLD enzyme mix for 1 h at 37°C. This enzyme mixture contains a kinase, a ligase and DpnI, allowing rapid PCR product ligation and template removal. DNA mixtures are then transformed into competent E.coli directly* [54].

After Kinase-Ligase-Dpnl (KLD) reaction, the site-specific mutagenesis of double-stranded plasmid DNA is finished in a single 5 min reaction step, and then the complete plasmid DNA was transformed into competent cells.

3.2.5 Transformation of plasmids into competent *E. coli* cells

To transfer plasmids into competent *E. coli* cells, DNA solution (5-100 ng of plasmid DNA or 5-10 µl ligation reaction) were added to 100 µl competent *E. coli* (XL-1 blue, BL21(DE3) pLysSpRep4, C41(DE3)) cell suspension (stored at -80°C, thawed on ice), swirling gently, and mixtures were then incubated on ice for 30 min. To improve the transformation success rate, cells were heat-shocked for 1 min at 42°C and then transferred to ice immediately for at least 1 min. Following adding 900 µL luria broth (LB) medium, cell suspensions were incubated at 500 rpm, 1 h at 37°C using the mixer incubator. Transformed cell suspension were then centrifuged at 5 000 rpm for 5 min. After removal of 800-900 µl supernatants, the residual 100-200 µl of the cell suspension was plated onto a pre-warmed LB agar plate with appropriate selection antibiotic (Ampicillin, 100 µg/ml) and spread it using sterile glass beads. Following incubation in a 37°C incubator overnight, the plates containing colonies were stored at 4°C in the refrigerator.

3.2.6 Preparation of XL-1 blue cells for plasmid purification

In order to get high-quality plasmid DNA for molecular biology applications, plasmid DNA was purified from XL-1blue cells using QIAprep Miniprep Kits (Jena Bioscience). A single colony from a selective LB agar plate was picked by a pipette tip, placing the tip into 6 ml LB medium containing ampicillin (100 µg/ml), and the starter culture of bacterial cells was incubated overnight at 37°C with vigorous shaking (approx. 180-200 rpm). On the following day the bacterial cells were harvested by centrifugation at 10 000 × g for 1 min in a standard benchtop microcentrifuge. For subsequent Mini plasmid purification, the protocol "Isolation of high-copy plasmid DNA from *E.coli*" from the Macherey-Nagel plasmid DNA purification user manual was used. (should be replaced by Miniprep protocol later)

3.2.7 Recombinant expression of GST-DIAPH1 FL, GST-DIAPH1 FH2 and GST-DIAPH1 dFH2 in bacteria

The GST-DIAPH1full length (FL) in the pGEX-6P-2A vector was provided by Saskia Grüb (PhD student) and the FH2 domain was (aa 624–1049) provided by Jessica Nojszewski (PhD student). For the mutation of GST-DIAPH1 dFH2, the KLD reaction was performed as described in 3.2.4.

The DIAPH1 recombinant proteins with N-terminal GST-tag (GST-DIAPH1 FL, GST-DIAPH1 FH2 and GST-DIAPH1 dFH2) were expressed in BL21(DE3) pLysS *E. coli* cells. A

single colony from the LB agar plate was picked, and the picked bacterial cells were incubated as described above. On the next day, pre-cultured cells were transferred into an Erlenmeyer flask (1L) with 400 ml LB medium containing 100 µg/ml of ampicillin and incubated in a shaker at 37 °C until OD600 reaching 0.8-1.0. At the desired OD600 the expression was induced with 0.7 mM Isopropyl-β-D-thiogalactopyranosid (IPTG) and the bacteria were incubated overnight at 20 °C with vigorous shaking (approx. 180-200 rpm). On the third day the bacterial cells were harvested by centrifugation at 5 000 rpm, 15 min at 4 °C (GSA Rotor) and the cell pellets were washed once with 1× PBS. Thereafter, the cell pellets were resuspended in 20 ml lysis buffer (1× PBS, 10% glycerol, 1 mM EDTA, 1 mM DTT, 5 mg/ml lysozyme, 0.5 mM PMSF and 0.2 mM protease inhibitor cocktail (PI, LOT 45842900, Sigma-Aldrich), pH 7.5) (see more details in table 8) and sonicated (75% power, interval 50%) on ice three times for 60 seconds each. After the centrifugation of lysates for 45 min at 4 °C (Sorvall SS-34 rotor, 20 000 rpm), the cell-free supernatants were cleared using a 0.45 µM pore filtropur syringe filter (Sarstedt). In the meantime, 1.0 ml of Glutathione sepharose-beads (GE Healthcare) were washed three times with running buffer (see the components in table 8) (20 mM HEPES, 150 mM KCl, 10% glycerol, 1.0 mM DTT). Afterwards, cell lysates and equal amounts of running buffer were applied to equilibrated beads and incubated overnight at 10°C in a rotator in the cooling cabinet (Thermo Fisher Scientific Asheville LLC). On the next day agarose beads coupling to glutathione, an efficient ligand for GST fusion proteins, were centrifuged at 500 g, 10 min at 4°C, and supernatants were stored in 50 ml Falcon in an icebox while beads were washed 3 times with running buffer. Afterwards the beads were incubated with 1 ml elution buffer (0.1 M PMSF, 0.2 mM PI and 30 mM glutathione in running buffer, pH 8.0) on the rotating wheel for 10 min at RT and the supernatants were collected as elution fractions. The elution step was repeated twice and then eluted beads were incubated with lysates supernatants again as mentioned above, and proteins were eluted again the following day. The amount of proteins in elution fractions, lysate supernatants and eluted beads were quantified in SDS-Page using 0.5 µg/20 µl BSA as standard, stained with Roti Blue quick (Roth). Afterwards, the eluted beads and soluble proteins were stored on ice to maintain the activity of the proteins. Degradation of proteins should be checked weekly, especially before performing functional analysis experiment.

3.2.8 Recombinant expression of GFP-DIAPH1 FL, GFP-DIAPH1 FH2 and GFP-DIAPH1 dFH2 in bacteria

The cDNA with a single-stranded overhang coding for DIAPH1 FL and DIAPH1 FH2 was mutated from fusion genes (GST-DIAPH1 FL gene in pGEX-4T vector) [45] by polymerase chain

reaction (PCR). The complementary overlaps between the mutated cDNA for coding (as described in 4.2.7) DIAPH1 FL, DIAPH1 FH2 and the cDNA of pSF421_10× His_GFP tag were then proceeded and generated by the exonuclease activity of T4 DNA Polymerase (BioLabs® inc. M0203S). The cDNA coding for GFP-DIAPH1 dFH2 was mutated from GFP-DIAPH1 FL by KLD reaction (Kinase-Ligase-Dpnl, Q5 Site-Directed Mutagenesis Kit) as described in section 3.2.4. Afterwards the GFP fusion genes were checked by 0.8-1.0% agarose gel electrophoresis, transformed on LB agar with 100 µg/ml Ampicillin and purified using QIAprep Spin Miniprep Kit as described in section 3.2.5 and 3.2.6.

The GFP-DIAPH1 recombinant protein (GFP-DIAPH1 FL, GFP-DIAPH1 FH2 or GFP-DIAPH1 dFH2) were expressed in C41(DE3) *E. coli*. The process of protein expression from the pre-culture of bacterial cells to the sonication of the cell suspensions was the same as for GST fusion protein expression as in 3.2.6.

Following centrifugation of lysates using SS-34 rotor (at 20 000 rpm, 45 min at 4°C), the supernatants were added with 5% (25 mM) Imidazole, incubated for 5 min, and then centrifuged (at 20 000 rpm, at 4°C, sorvall SS-34 rotor) again for another 20 min. These supernatants were filtered with a 0.45 µM pore filtropur filter (Sarstedt). Afterwards proteins were purified with NGC Chromatography Systems with regenerated Nickle column (Bio-ScaleTM Mini ProfinityTM IMAC Cartridges, 5 ml). NGC system was flushed by Buffer A (20 mM HEPES, 150 mM KCl, 0.1 mM β-Mercaptoethanol) and Buffer B (20 mM HEPES, 150 mM KCl, 0.1 mM β-Mercaptoethanol, 500 mM Imidazole). Fraction occurring during the peak of curve were collected as elution fraction. All elution fractions were put together in SERVA® dialysis tubing (181080, MWCO 12 000-14 000), and imidazole was eliminated using the method of dialysis, placing the dialysis tubing in 3 L dialysis buffer (20 mM HEPES, 150 mM KCl, 0.1 mM β-Mercaptoethanol) overnight at 10°C with a magnetic stirring bar. The amount of protein in elution fractions was quantified by SDS-Page using 0.5 µg/20 µl BSA as standard, stained with coomassie blue staining solution (Roti®Blue quick). Soluble proteins were stored on ice to maintain the activity of the proteins.

3.2.9 Determination of the binding ratio between DIAPH1 and tubulin

To assess whether DIAPH1 is required to initiate tubulin polymerization via binding to tubulin dimer, the binding concentration ratio of DIAPH1 to tubulin is determined. For this purpose, the amount of DIAPH1 and tubulin was detected in HT-29 scrambled cells, using different

amount of GST-DIAPH1 and tubulin proteins as standards. While contents of tubulin (Cytoskeleton) were prepared based on the manufacturer datasheet, amounts of GST-DIAPH1 protein were estimated with reference to the BSA standard on the SDS-PAGE gel. We prepared a set of standards from GST-DIAPH1 (25 µg, 50 µg, 100 µg and 200 µg) and tubulin (50 µg, 100 µg, 200 µg and 400 µg). On the other hand, HT-29 control cells were lysed with MPer protein extraction reagent, and 20 µg protein were prepared using Bradford protein assay (see more details in section 3.1.4). The cellular concentrations of DIAPH1 and tubulin were evaluated by comparing their band intensities to those of GST-DIAPH1 and tubulin proteins using ImageJ (Fiji). In addition, the band intensities were detected by imaging system after proteins coupling to the corresponding HRP (see more details in section 3.1.5). The mean value of those four calculated concentrations was taken, and then the ratio between cellular DIAPH1 and tubulin was analyzed.

3.2.10 MT polymerization assay

The light could be scattered at 340 nm by microtubules, indicating nucleation, growth and steady state equilibrium of microtubules. To analyze the effect of GST-DIAPH1 FL and GST-DIAPH1 FH2 on MT-polymerization, the proteins dissolved in the running buffer were concentrated with Vivaspin 500 centrifugal concentrators (Sigma-Aldrich), and the running buffer was replaced with microtubule buffer (MT-buffer; 80 mM PIPES, 2 mM $MgCl_2$, 0.5 mM EDTA, pH 6.9) and 1.0 mM GTP. The concentrations of prepared proteins were estimated using 0.5 µg/20 µl BSA as standard by SDS-PAGE and the final concentration was adjusted with MT-buffer based on the molecular ratio of GST-DIAPH1 FL to tubulin (1: 3) and of GST-DIAPH1 FH2 to tubulin (1: 6.7) (see section 3.2.9). Components of 2 µM non-labeled tubulin and 0.67 µM GST-DIAPH1 FL or 0.3 µM GST-DIAPH1 FH2 in 85 µl MT-Buffer were pipetted in duplicate into 96-well transparent plates (pre-warmed to 37°C) to a final volume of 100 µl. In parallel, 2 µM tubulin and 95 µl MT-Buffer in the control group were also added in duplicate into the 96-well plate. Tubulin was added at the last step and bubbles had been avoided. In the end polymerization of the microtubules was measured continually at the absorbance of OD340nm with the Tecan Infinite M200 plate reader for 7 h at 37°C.

3.2.11 MT bundling assay

To assess the effect of GST-DIAPH1 proteins on microtubules assembly, MT bundling assay was performed. Aliquoted labeled tubulin (0.125 mM, stored at -80°C) was thawed in hand quickly. 0.7 µl 100 µM Taxol was added to thawed tubulin, and the mixtures were incubated in

37°C water bath for 30 min. During this incubation period, MT buffer mixtures were prepared freshly, consisting of 0.5 ml MT-buffer (80 mM PIPES, 2 mM $MgCl_2$, 0.5 mM EDTA, pH 6.9), 20 µM Taxol and 1 mM GTP, and incubated in the 37 °C water bath for 10 min. After incubation, 1 µl tubulin containing Taxol were added to 360 µl MTs buffer mixture in 1.5 ml brown reaction tubes, and the mixtures were incubated in 37°C water bath for 20 min. Afterwards, the samples were kept at RT overnight in the dark. On the following day Microtubule-Tubulin mixtures were incubated in a 37°C water bath for 20 min as before. In the meantime, an 8-well chamber slide (ibidi ®) was prepared, coating with 200 µl Poly-L-Lysine for 30 min, and then air dried. Poly-L-Lysine could be reused.

The proteins of GST-DIAPH1 FL and GST-DIAPH1 FH2 were concentrated and the running buffer was replaced as described in section 3.2.7. The final concentration of GST-DIAPH1 FH2 was prepared as 0.45 folds as that of FL using MTs buffer to make sure the molecular ratio and volume of tested proteins being the same. Afterwards, 10 µl of GST-DIAPH1 FL or GST-DIAPH1 FH2 was added to 10 µl labeled MTs, and the mixtures were distributed equally on Poly-L-Lysine coated chamber, then mounted with 40 µl SouthernBiotech mounting medium (Fluoromount G®) after 10 min of incubation. As a control group, 10 µl labeled MTs were mixed with 10 µl MTs buffer, pipetting into the chamber and mounting the medium as above. Finally, MTs signals were detected by Keyence Microscope at 658 nm.

3.2.12 MT binding assay

To analyze the extracellular colocalization of microtubules with the DIAPH1 proteins, labeled MTs, GFP-DIAPH1 proteins (GFP-DIAPH1 FL, GFP-DIAPH1 FH2) and Poly-L-lysine coated chamber slides were prepared as described in section 3.2.10 and 3.2.11. The volumes of MTs and GFP-DIAPH1 proteins were calculated as described in section 3.2.10 to keep the same number of molecules present of GFP-DIAPH1 FL and GFP-DIAPH1 FH2. To evaluate the capacity of GFP-DIAPH1 binding to MTs, the mixtures were imaged by Keyence Microscope after 10 min incubation, and the GFP-DIAPH1 proteins were detected at 488 nm (green channel) while the labeled MTs were detected at 658 nm (red channel).

3.3 Statistical analysis

The number of analyzed experiments is shown in the corresponding figures. Statistical analysis was performed using SigmaPlot 8.0. All data were shown as mean±SD (or SEM) or median ±SD. To calculated the statistical significance, the numerical and normally distributed data

were analyzed by unpaired Student's t-test, while the categorical data with normal distribution were analyzed by One-Way Analysis of Variance (ANOVA). We considered P values < 0.05 as statistically significant, shown as $*p < 0.05$, $**p < 0.01$ $***p < 0.001$, while n.s. means not significant.

4 Results

4.1 Cellular localization of DIAPH1

Since Kato et al. revealed that DIAPH1 co-localizes with spindle MTs in HeLa cells [55], it was likely that, in addition to interphase MTs, DIAPH1 also accumulated at spindle MTs in meta-phase cells. To address this assumption, localization of DIAPH1 in HCT-116 and HT-29 cells

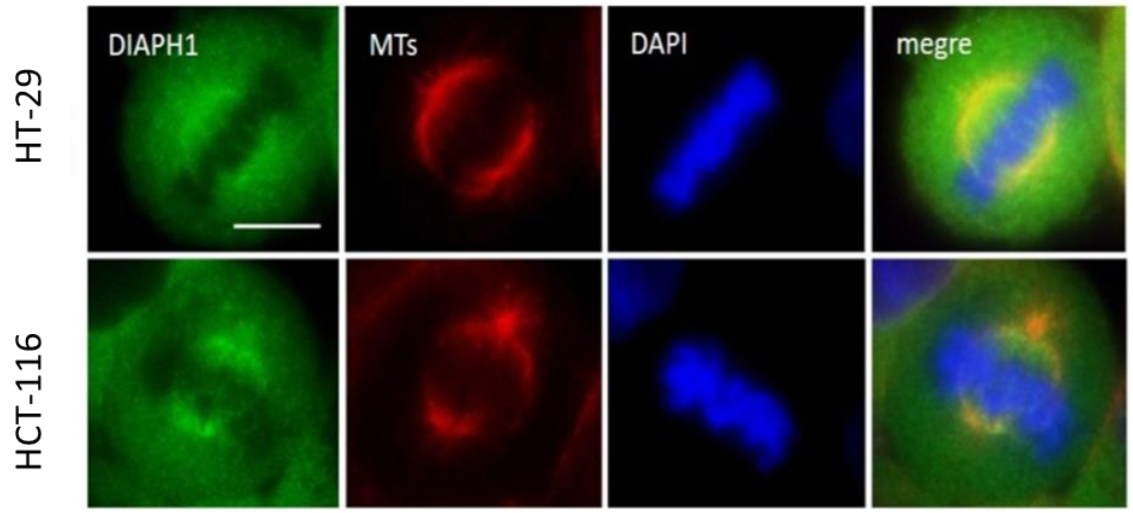

Figure 16 Cellular localization of DIAPH1. *HT-29 (upper panel) and HCT-116 (lower panel) cells were synchronized in meta-phase by double thymidine block, fixed and stained for DIAPH1 (green) and MTs (red) using specific Alexa-Flour-488 or Alexa-Flour 568-coupled antibodies. Chromosomes were stained with DAPI (blue). The right images are merged from all three channels. Bar: 5μm.*

was analyzed using DIAPH1-specific Alexa-fluor488-conjugated (green) and β-tubulin-specific Alexa-fluor568-conjugated (red) antibodies. Indeed, it could be shown that DIAPH1 co-localized with spindle MTs (Fig. 16).

4.2 Depletion of DIAPH1 in colorectal carcinoma cells

To investigate whether the role of DIAPH1 in colorectal carcinoma cells is associated with cancer-specific chromosomal instability, DIAPH1 mRNA was stably depleted in chromosomally stable HCT-116 and chromosomally stable HT-29 cells, using the lentiviral shRNA transduction approach.

DIAPH1 was depleted by sh4 and sh5 vectors (see in section 3.1.2), and the success of this manipulation was checked by Western blotting (Figure 17). In HCT-116 cells, the expression

level of the DIAPH1 protein was decreased by 60% (sh4 = knockdown 4) and by 80% (sh5 = knockdown 5), as compared to HCT-116 scrambled shRNA control cells. While in

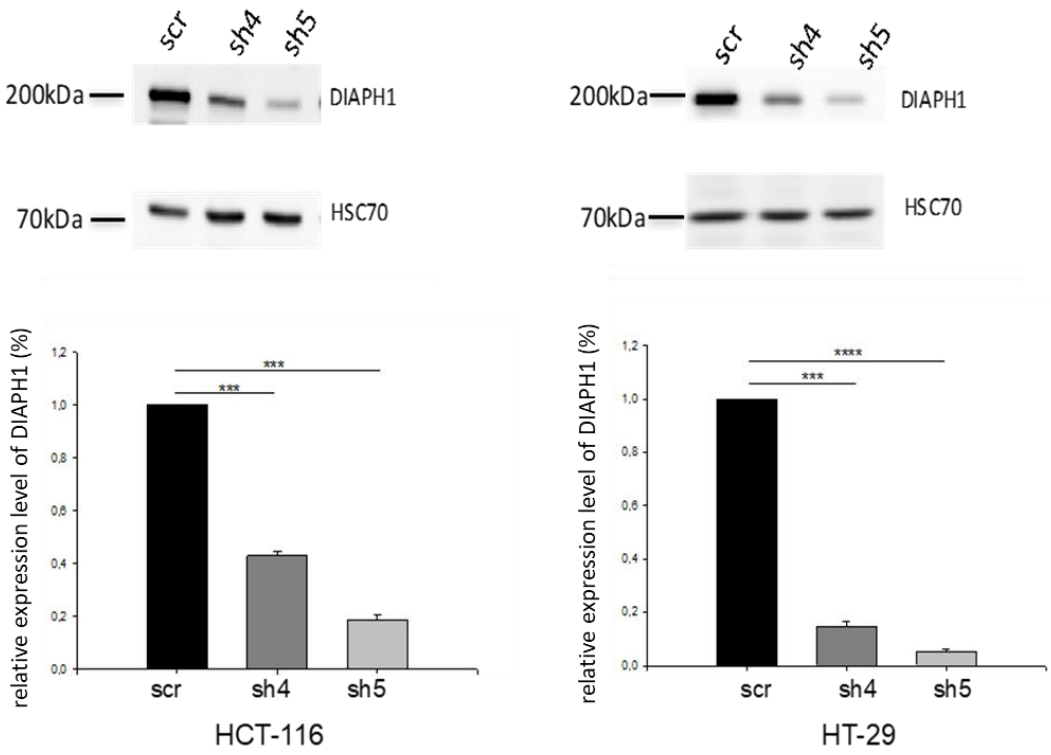

Figure 17 Depletion of DIAPH1 in colorectal carcinoma cells. *HCT-116 and HT-29 cells were transduced with shRNA lentivirus against human DIAPH1 (sh4 and sh5), or with scrambled shRNA viral particles, and then selected with puromycin (2.0 µg/ml). Expression levels of DIAPH1 gene were examined by western blotting and quantified using ImageJ software. HSC70 served as loading control. Data were normalized to DIAPH1 controls and shown as mean ± SD from 3 independent experiments. ***P <0.001.*

HT-29 cells, the expression level of the DIAPH1 protein was decreased by 80% (sh4= knockdown 4) and by 90% (sh5 = knockdown 5), comparing to HCT-116 scrambled shRNA control cells. For all further experiments, we compared scrambled control cells with DIAPH1 sh4 and sh5 cells.

4.3 Effect of DIAPH1 in spindle MT dynamics during metaphase

Localization of DIAPH1 to spindle MTs suggests a role of DIAPH1 in controlling the dynamics of spindle MTs. To validate this assumption, metaphase cells were treated with SiR-tubulin, that specially labels MTs in living cells.

Cells were imaged from meta- until early anaphase every 4 minutes and 3D-reconstructions were created to analyze speed (µm/h) of spindle MTs by the IMARIS software (Fig. 18A). This live cell imaging analysis revealed that spindle MTs in DIAPH1 scrambled cells moved toward

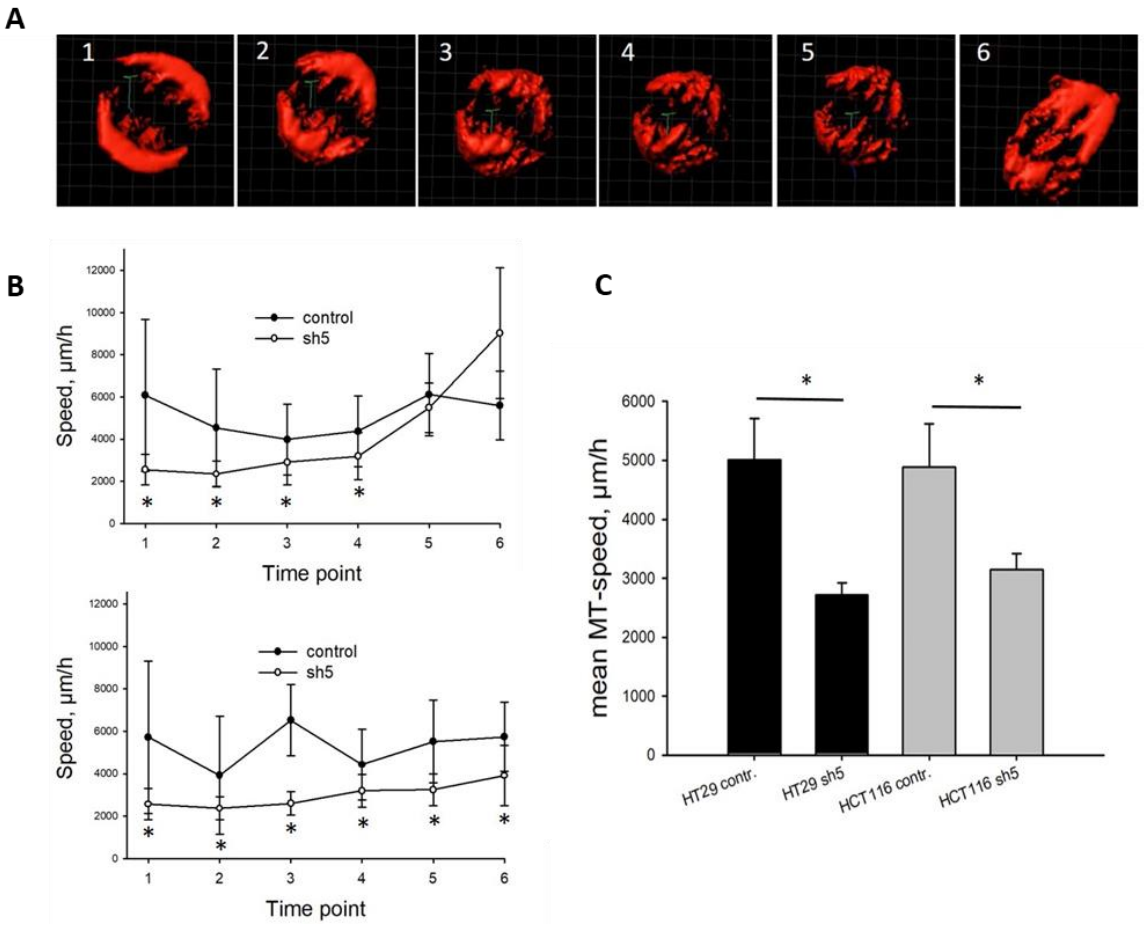

Figure 18 Depletion of DIAPH1 reduces the speed of spindle MT movement in metaphase. *HT-29 and HCT-116 cells were incubated with SiR tubulin and spindle dynamics were imaged from meta- to anaphase by a spinning disk laser microscope. (A) Shown are three-dimensional (3D) reconstruction images created with the IMARIS software of HT-29 cells from metaphase to anaphase. (B) Spindle MT speed dynamics (µm/h) was calculated using IMARIS software at different time points. Upper panel: HT-29 cells, Lower panel: HCT-116 cells. (C) Shown are mean spindle MT speed of both HT-29 and HCT-116 cells at metaphase from time point 1-6. Data were calculated from at least 30 cells per cell line in two different experiments and represented as mean ± SD. *p<0.05.*

the spindle poles faster than those in DIAPH1 knock down cells during metaphase. In addition, the mean speed of spindle MTs was significantly higher in DIAPH1 control cells of both cell lines. In conclusion, DIAPH1 played an essential role in the control of spindle MT-dynamics.

4.4 Effect of DIAPH1 on MT-polymerization *in vitro*

Based on our results that depletion of DIAPH1 reduced spindle speed, we next analyzed the effect of purified DIAPH1 on MT-polymerization in a cell-free *in vitro* assay.

Before doing so, the tubulin to DIAPH1 ratio in HT-29 cells was determined by western-blotting (Figure 19). We found a ratio of 3: 1 (tubulin: DIAPH1) which was used to test the effect of DIAPH1 on MT-polymerization. We also found a similar ratio in HCT-116 cells (data not shown).

To test the effect of DIAPH1 on MT-dynamics, GST-DIAPH1 proteins and GFP-DIAPH1 proteins were expressed in *E.Coli* and enriched by glutathione affinity and affinity column chromatography (ACC) and/or size exclusion chromatography (SEC) separately. Thereafter the concentrations of the elution fractions were estimated, using 0.5 µg BSA as standard in the SDS-PAGE (Fig. S 1).

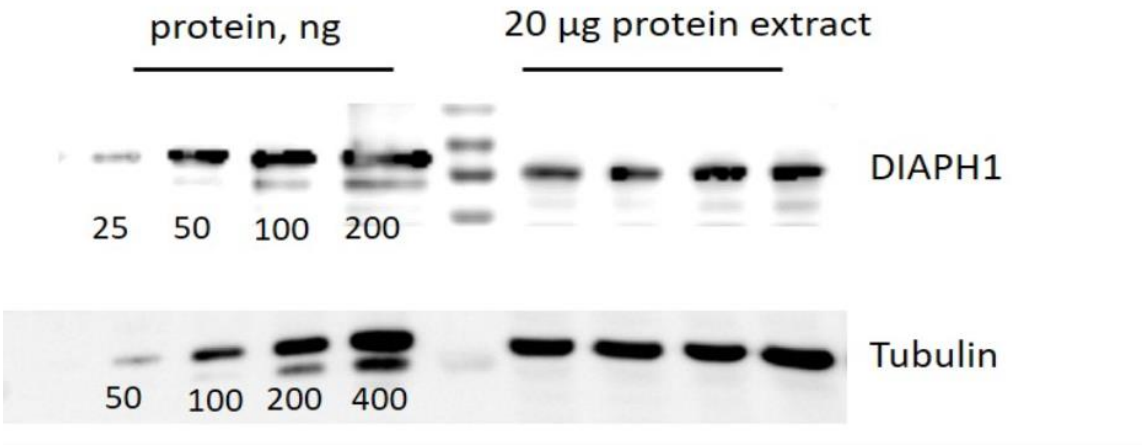

Figure 19 Determination of the cellular tubulin to DIAPH1 ratio. *Different amount of protein standards (GST-DIAPH1and tubulin proteins) as well as 20 µg protein extracted from HT-29 cells were loaded to and separated by SDS-PAGE gel, and then blotted onto nitrocellulose membrane. The amount of cellular DIAPH1 and tubulin were analyzed by comparing their relative band intensities to those of GST-DIAPH1 and tubulin proteins. These band signals were detected by a chemiluminescence imaging system using specific peroxidase coupled antibodies. Mean values of those four intensities were calculated and the cellular binding ratio was then analyzed. (Tubulin: 15 ng/µg and DIAPH1: 5 ng/µg).*

After loading the elution fraction on SDS-PAGE, the bands of GST-DIAPH1 proteins were detected using coomassie staining solution with reference to high molecular weight (HMW) marker (GST-DIAPH1 full-length (FL): 168 kDa, GST-DIAPH1 FH2-domain (FH2): 76 kDa)

(Fig. S 7A-B). The bands corresponding to GST-DIAPH1 FH2 were thick, indicating high protein yields (Fig. S 7B). The analysis of GST-DIAPH1 proteins showed that concentrations of GST-DIAPH1 FH2 and GST-DIAPH1 dFH2 were similar, 1.3-fold higher than GST-DIAPH1 FL at a concentration of 0.075 mg/ml, as estimated by BSA standards (Fig. S 7C).

The effect of DIAPH1 on MT-polymerization was analyzed using a turbidity assay. Importantly there was no paclitaxel present when measuring the effect of DIAPH1 on MT-polymerization at the absorbance of OD340nm with the Tecan Infinite M200 plate reader. The DIAPH1 proteins were concentrated with Vivaspin 500 centrifugal concentrators and the running buffer was replaced with MT-buffer to exclude the effect of HEPES buffer on the assay. The final concentrations were adjusted with MT-buffer based on the molecular ratio as described in 4.2.10. There seems to be no obvious protein degradation after concentrating and buffer exchange (Fig. 20A). The result of this experiment showed that only the isolated FH2 domain increased MT-polymerization while auto-inhibited full length (FL)-DIAPH1 had no effect on the assembly of

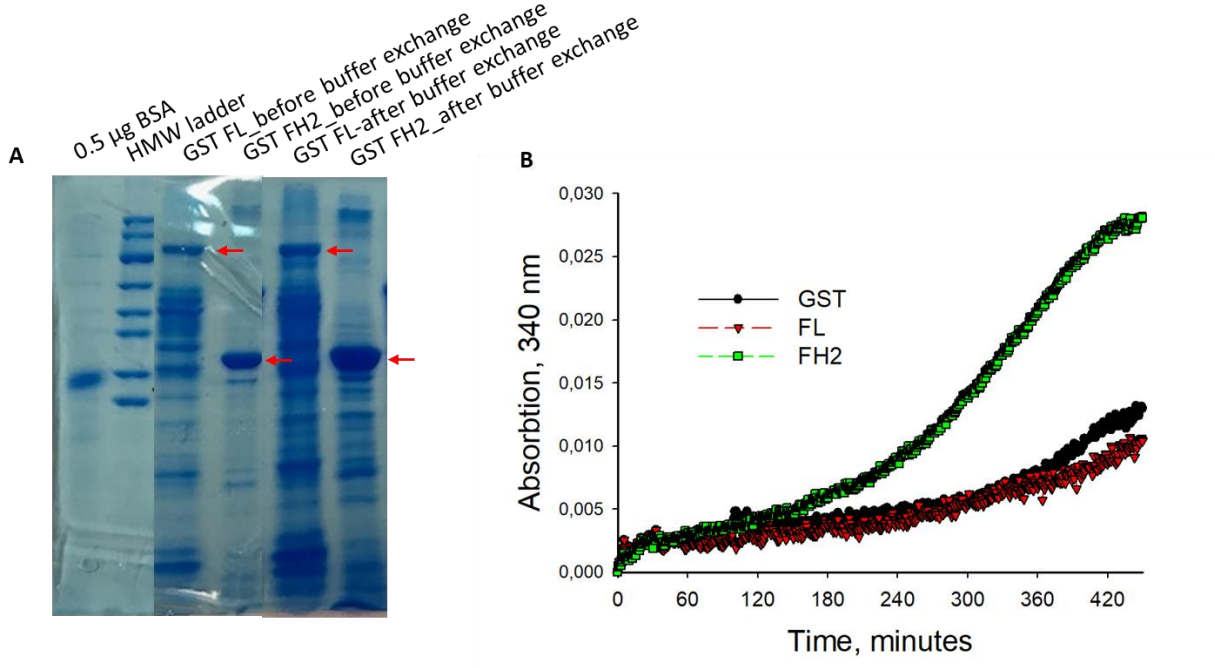

Figure 20 Effect of DIAPH1 FL and DIAPH1 FH2 on MT-polymerization. *The proteins were concentrated and running buffer was replaced with MT-buffer. Final concentrations of proteins were adjusted with MT-buffer based on the molecular ratio of GST-DIAPH1 FL to tubulin (1: 3) and of GST-DIAPH1 FH2 to tubulin (1: 6.7). (A) Shown is the SDS-PAGE of proteins before, and after concentrating and buffer exchange (indicated by the red arrow). The concentration was estimated using 0.5 µg BSA as standard. (B)Tubulin was incubated in GTP-containing MT-buffer for 7 h at 37°C in presence of GST (control), FL or FH2 in a Tecan reader.*

microtubules (Fig. 20B). The absorption line of DIAPH1 FH2 reached the plateau after 7 h and the maximum absorption was 3.0-fold higher compared to that of DIAPH1 FL and GST control (Fig. 20B). We excluded the dFH2 polymerization curve because of its unreasonable and strange trend (data did not show), therefore, dFH2 would not participate in following extracellular assay in this project.

4.5 DIAPH1 enhanced chromosomal stability

Alterations in spindle MT dynamics can result in misalignment and in mis-segregation of chromosomes, leading to unequal distribution of chromosomes into the daughter cells and finally to chromosomal instability (CIN). In order to address this assumption, modified HCT-116 cells and HT-29 cells were synchronized in metaphase and chromosomes, MTs and centromeres were stained with DAPI, using a β−tubulin specific antibody, and an antibody against CENP-A respectively (Figure 21A). Thereafter, the number of metaphase cells with properly aligned or with misaligned chromosomes were counted and the percentage of cells with aligned chromosomes was calculated with reference to control cells (Figure 21B).

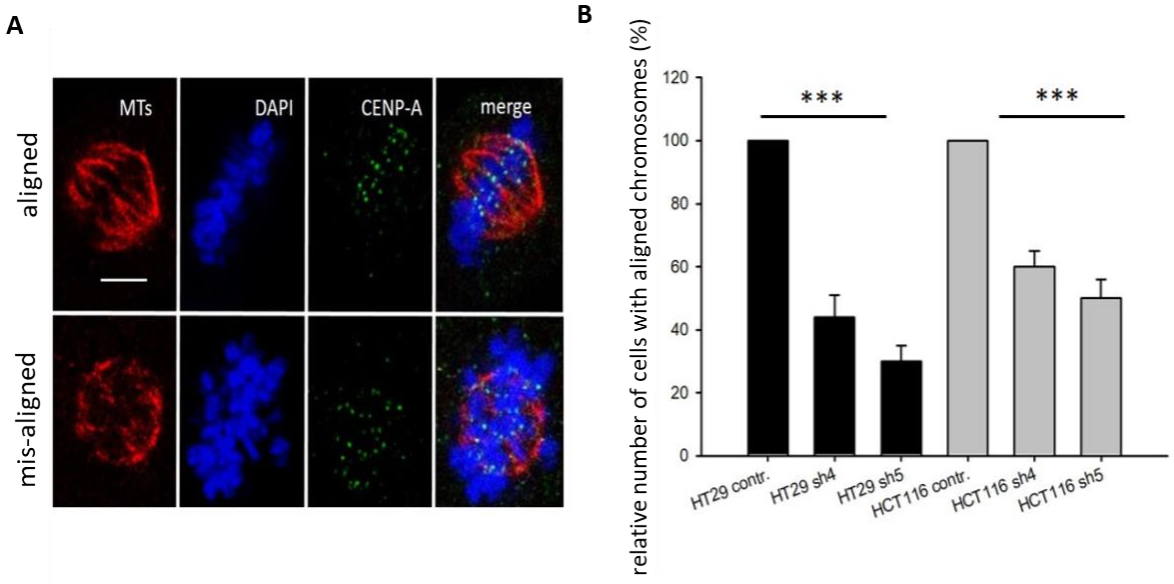

Figure 21 DIAPH1 controls chromosome alignment. *DIAPH1 control and knock down cells (sh4 and sh5) were synchronized in metaphase by double thymidine block. (A) HT-29 and HCT-116 cells were synchronized in metaphase by double thymidine block, fixed and stained for MTs (red) or CENP-A (green) using specific Alexa Flour 568 or Alexa Flour 488-coupled antibodies. Chromosome were stained with DAPI (blue). Bar: 5 µm. Shown are two representative images of HT-29 cells. (B) The number of metaphase control and DIAPH1 sh4 and sh5 cells exhibiting aligned or misaligned chromosomes was counted and the percentage of each type was calculated. 120 cells from two independent measurements were evaluated and a statistical significance was analyzed by the chi square test. Data were shown as mean ± SD. ***p<0.001.*

We found that depletion of DIAPH1 reduced the number of cells with aligned chromosomes by 55% (k.d. 4) and 70% (k.d. 5) in HT-29 cells, in HCT-116 cells by 40% (k.d. 4) and 50% (k.d. 5), indicating that DIAPH1 is indeed involved in controlling chromosome alignment in colorectal carcinoma cells. It seems that the effect of DIAPH1 depletion on mis-segregated chromosomes in HT-29 cells was stronger than that in HCT-116 cells, most likely due to stronger DIAPH1 knockdown in HT-29 cells (see in Figure 17).

Bakhoum, et al. revealed that microtubule dynamics defects not only result in chromosomal misalignment but also in chromosomal mis-segregation [56]. Based on this consideration, cells were synchronized in anaphase and chromosomes, MTs and centromeres were stained as shown in 3.1.7 (Fig. 22A). Thereafter, the number of anaphase cells with mis-segregated chromosomes was compared between DIAPH1 control cells and depleted cells. The analysis showed that the

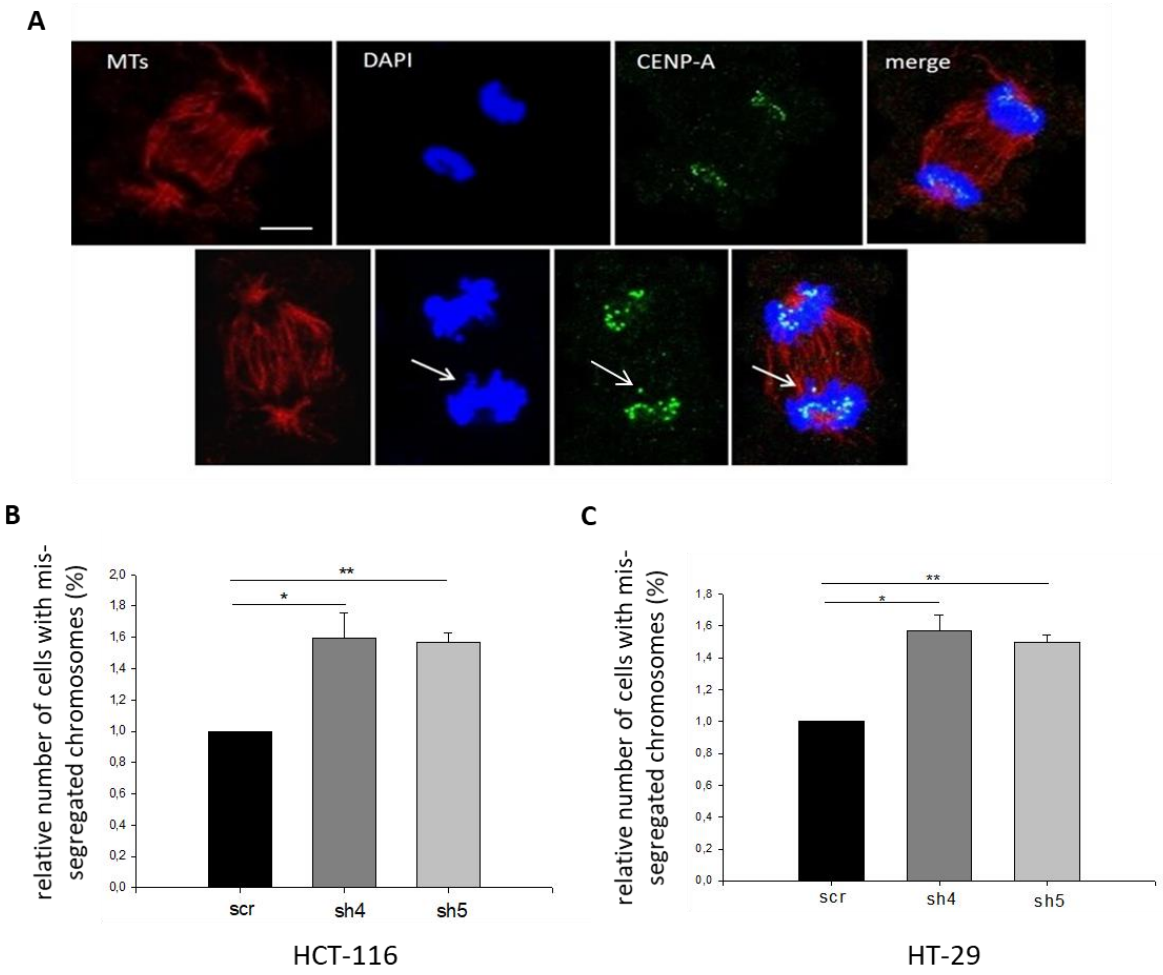

Figure 22 DIAPH1 controls chromosomal segregation. *Control and DIAPH1-depleted cells (sh4 and sh5) were synchronized in anaphase by double thymidine block. (A) The cells were fixed and stained for MTs (red), chromosomes (blue) and centromere protein A (CENP-A, green). Shown are representative images of HT-29 cells with segregated (upper panel) and mis-segregated chromosomes (lower panel).*

*(B, C) The normalized percentage of anaphase cells with mis-segregated chromosomes to control levels is shown. At least 120 cells per cell line were analyzed and experiments were repeated twice. Data were shown as mean ± SD. *p<0.05, **p<0.01.*

number of cells having mis-segregated chromosomes in control cells was nearly 1.6 fold higher as that in knock down cells, both in HCT-116 cells and HT-29 cells (Fig. 22B-C). Interestingly, the number of cells with mis-segregated chromosomes was similar between HT-29 cells and HCT-116 cells, indicating similar effect of DIAPH1 depletion on chromosomal mis-segregation.

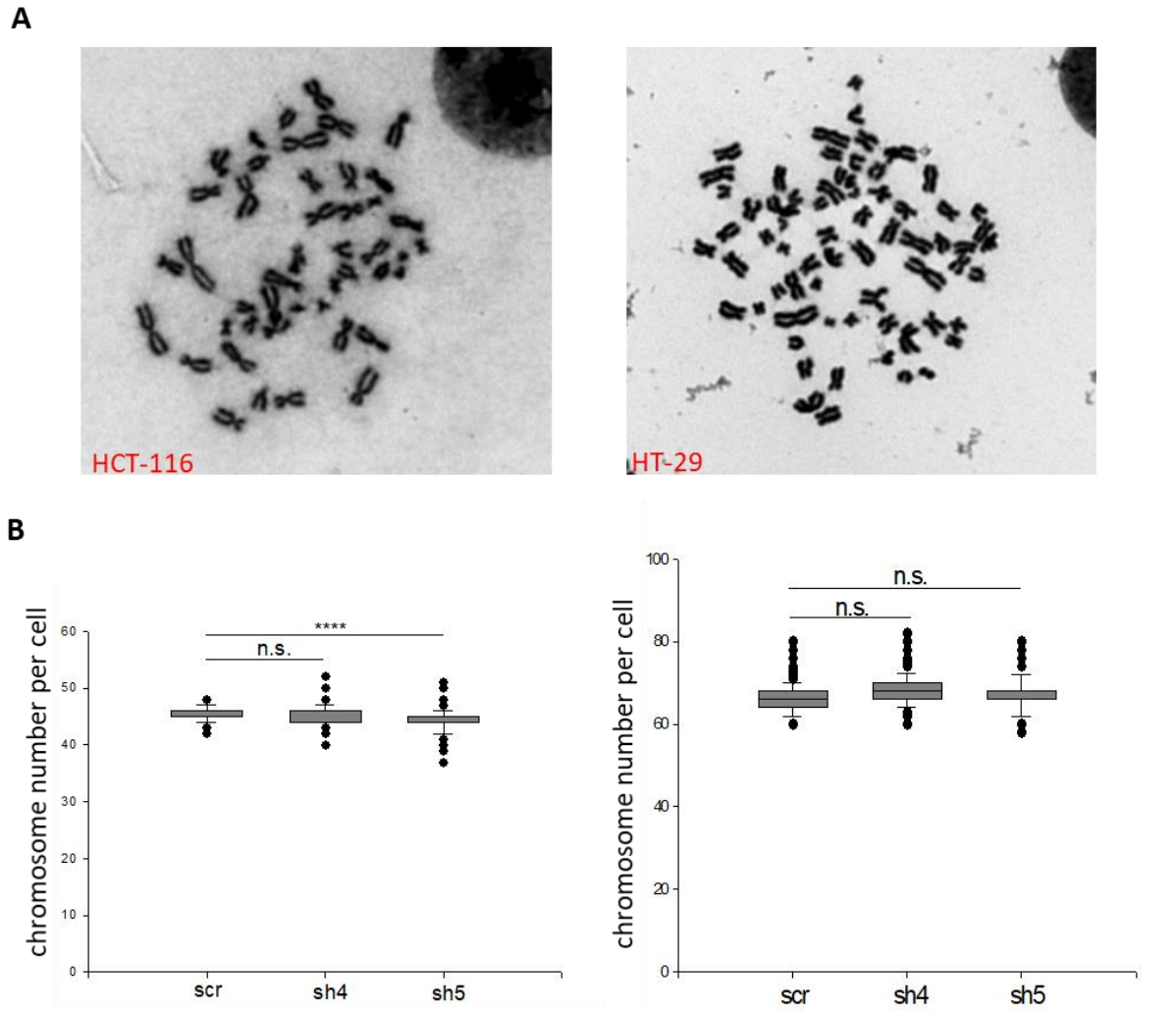

Figure 23 Chromosome number of control and DIAPH1 depleted cells. *Chromosomes were prepared from metaphase cells arrested by colchicine, and stained with Giemsa solution. (A) Upper panel: Shown is one representative preparation from control cells of each cell line. (B) Lower panel: The number of chromosomes from at least 180 control or DIAPH1-depleted cells was counted. Shown are median values of ± SD. ****p<0.0001; n.s. not significant.*

In general, eukaryotic chromosomes have a single centromere that ensures their accurate segregation during mitosis. Chromosomes that lack centromeres or have multiple centromeres will segregate randomly during mitosis [11]. To show if mis-segregation resulted from an increase of acentric chromosomes, number of cells having mis-segregated chromosomes without centromere was counted in both HCT-116 cells and HT-29 cells. The analyzed images were the same as that for cells with chromosomal mis-segregation. Cells were defined as acentric chromosome cells when one of the mis-segregation chromosomes appeared to be without centromeres. This analysis revealed that there was no significant difference between DIAPH1 control and DIAPH1 depleted cells (Fig. S 3).

Increased chromosomal misalignment and mis-segregation found in DIAPH1 depleted cells very likely resulted in altered number of chromosomes in daughter cells. To show this, chromosomes were isolated from control and DIAPH1 depleted cells and stained with Giemsa solution (Fig. 23A). Interestingly, only in the chromosomal stable cell line HCT-116 sh5 DIAPH1 depletion significantly altered chromosome number, while in chromosomal unstable HT-29 cells no effect was found (Fig. 23B). In nHCT-116 sh5 cells, the chromosome number was 44 in average while the average chromosome number of control and sh4 cells was 46 (Fig. 23B). In HT-29 cells, the chromosome number was 68 in average and had high diversity between cells. This heterogeneity may explain why slight differences, possibly caused by DIAPH1 depletion, were not detectable.

Since averaged number of chromosomes in HCT-116 sh5 cells was reduced by two, karyotype analysis was performed. Chromosomes of mitotic cells were stained with Giemsa solution and regions of chromosomes that were rich in the base pairs Adenine (A) and Thymine (T) producing a dark band. Our results showed that in HCT-116 sh5 cells Y chromosome was lost, while chromosome 9 and chromosome 19 were triplet chromosomes in HCT-116 control cells (Fig. S4). This chromosome analysis was performed at the Institute of Human Genetics, University Medical Center Hamburg-Eppendorf (UKE).

Most mis-segregated chromosomes derived from lagging chromosomes (see arrow in Figure 19) or chromosomal fragments can develop to micronuclei [56,57]. Based on this consideration, cells were fixed and stained as described in 4.1.7. Number of interphase cells with micronuclei was counted. Compared with control cells, the number of cells with micronuclei was doubled

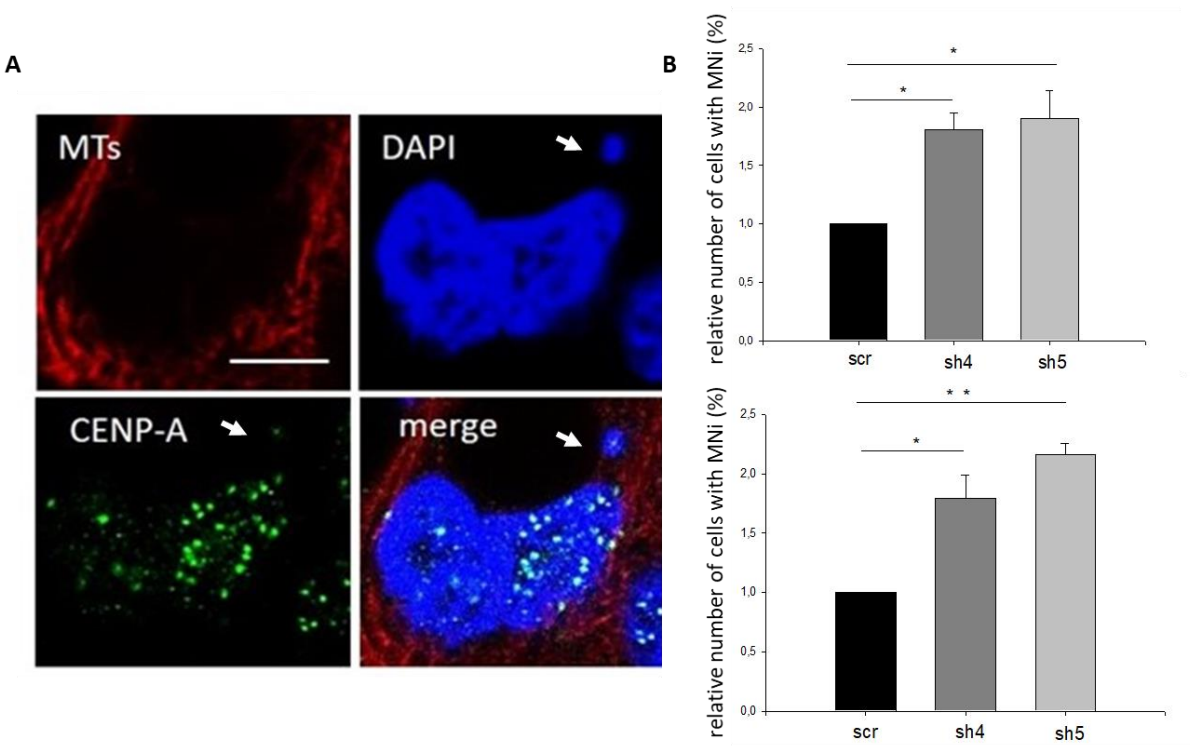

Figure 24 DIAPH1 controls formation of micronuclei. *Control and DIAPH1-depleted cells (sh4 and sh5) cells were fixed and stained for MTs (red), chromosomes (DAPI blue) and CENP-A (green). Micronucleus is indicated by the white arrow. (A) Shown is a representative image of micronuclei formation of HT-29 cells. (B) The relative percentage of cells with micronuclei to control levels is shown. Data were analyzed from 4 000 cells per cell line and shown as mean ± SD. *p<0.05, **p<0.01.*

in DIAPH1 depleted cells in both HCT-116 cells and HT-29 cells (Fig. 24B). We also found that the frequency of increased micronucleus was similar in both cell lines (Fig. 24B).

4.6 Effect of DIAPH1 on cell proliferation and apoptosis

The observed effect of DIAPH1 depletion on misalignment at metaphase may activate the spindle assembly checkpoint (SAC), and thereby reduces proliferation [58]. To validate this assumption, proliferation was measured by the IncuCyte Live Cell Analysis System. However, this analysis revealed that there was no significant difference in cell proliferation between HT-29 control and DIAPH1 depletion cell lines and cells had a rapid growth at 96 h while late-stage slow growth at 144 h (Fig. S 5).

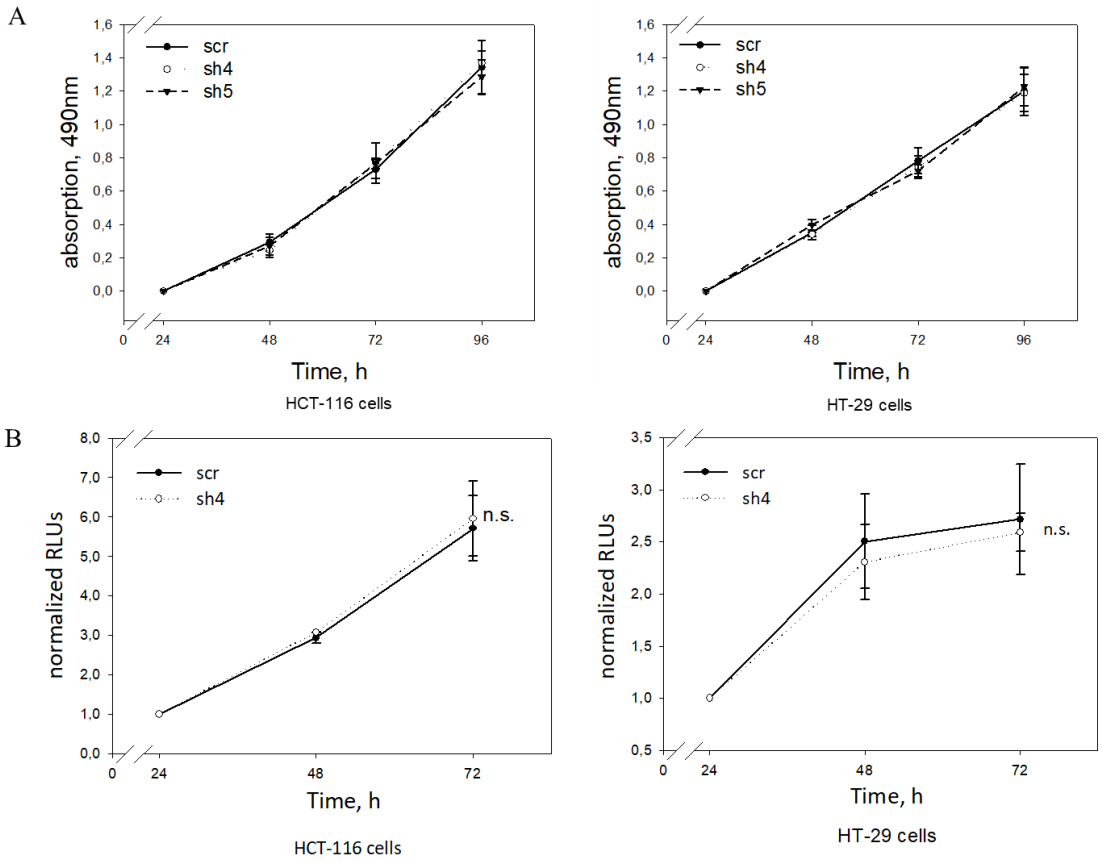

Figure 25 Effect of DIAPH1 on cell viability and caspase-3/7 activity. *For analyzing cell viability, 2.5 × 10^3 cells/well were seeded in triplicate, mixed with MTs reagent and the absorbance of the treated cells was measured at OD490 nm using absorbance-based plate reader. To compare the differences in cell apoptosis between control and DIAPH1 knock down cells, 2.0 × 10^4 cells per well were seeded in corning® 96-well white plates and apoptosis was analyzed by measuring the caspase-3/7 activities using TECAN microplate readers. (A) The viability of HCT-116 cells or HT-29 cells were analyzed using the MTs assay and the absorbance at OD490 nm were measured at 24 h, 48 h, 72 h and 96 h, normalizing by the absorbance values at 24 h. Shown are mean values of ± SD from two different assays. (B) Shown is the normalized relative light units (RLUs) for HCT-116 (left) and HT-29 cells (right) at 24 h, 48 h and 72 h, performed by luminescent assay. Shown are mean values ± SD from three independent assays. n.s. not significant.*

Due to some unsolved problems of the IncuCyte device, the proliferation assay for HCT-116 cells was not able to perform. Therefore, MTS assay was performed instead, for both HCT-116 and HT-29 cells, reflecting the cell's metabolic activity. Again, we found that depletion of DIAPH1 did not have an effect on cell viability on HCT-116 and HT-29 cells (Fig. 25A). Thus, it seems that depletion of DIAPH1 did not activate SAC.

Thompson, et al. reviewed that high CIN levels could induce cell apoptosis [11]. In case depletion of DIAPH1 affected apoptosis mediated by inducing high rates of CIN incidence, this programmed cell death should be increased. To show this, caspase-3/7 activities of control and k.d. cells were measured, using luminescent assay (Fig. 25B). Since DIAPH1 sh4 cells exhibited

stronger knockdown (data not shown), we performed this assay only for DIAPH1 controlled and sh4 cell lines. However, no significant differences were observed in luminescent signals, expressed as number of relative light units (RLUs), between DIAPH1 scrambled and depleted cells.

In conclusion, depletion of DIAPH1 did not alter viability and apoptosis in HCT-116 and HT-29 cells.

4.7 Effect of DIAPH1 on chemotherapy treatments of colorectal carcinoma cells

Colorectal carcinoma frequently shows low chemo-sensitivity during chemotherapy, which is associated with chromosomal instability [11]. To show if depletion of DIAPH1 could decrease the effects of chemotherapy treatments for CRCs by enhancing CIN, the relative viability was analyzed by MTS-assay after paclitaxel treatment.

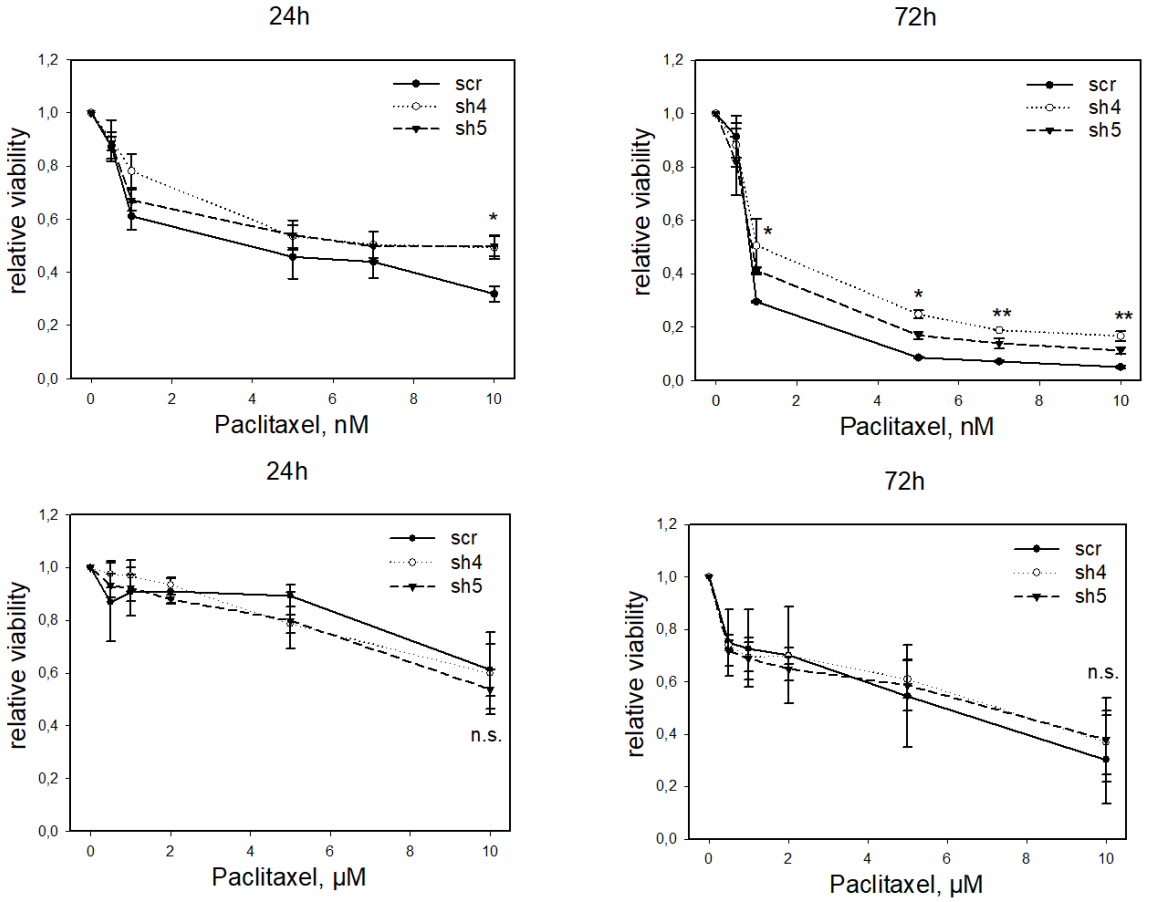

Figure 26 Effect of DIAPH1 on paclitaxel treatment for HCT-116 and HT-29 cells. *1.0 × 10^4 cells/well were seeded in 96-well microplates and cell viability were measured by MT-assay after treating with different concentrations of paclitaxel. Relative cell viability was normalized by the viability at*

*24 h. (A) Shown is the relative viability of HCT-116 cells at 24 h and 72 h. Cells were treated with paclitaxel with low concentrations (0 nM, 0.5 nM, 1.0 nM, 5.0 nM, 7.0 nM and 10 nM). (B) Shown is the relative viability of HT-29 cells after treating with high concentrations of paclitaxel (0 µM, 0.5 µM, 1.0 µM, 2.0 µM, 5.0 µM and 10 µM) at 24 h and 72 h. Shown are mean values ± SEM from three different assays, *p <0.05, **p <0.01, n.s. not significant.*

The analysis revealed that the relative viability of HCT-116 DIAPH1 knock down cells was higher than HCT-116 control cells at 24 h (with 10 nM paclitaxel) and at 72 h (with various concentrations of paclitaxel ranging from 0.5 nM to 10 nM) (Fig. 23A). However, there was no significant difference in cell viability after paclitaxel treatment between HT-29 control and DIAPH1 depleted cell lines, even after employing much higher concentrations of paclitaxel (ranging from 0.5 µM to 10 µM) (Fig. 26B).

In conclusion, DIAPH1 could increase sensitivity to paclitaxel in HCT-116 cells but not in HT-29 cells.

4.8 Cytokine expression in control and DIAPH1-depleted cells

The increased number of micronuclei found in DIAPH1 depleted cells could result in altered cytokine expression because DNA in micronuclei could be released into the cytosol. This cytosolic DNA is recognized by the pattern recognition receptor cyclic GMP-AMP synthase (cGAS) that in turn mediates transcription of inflammatory genes [59]. Accordingly, we analyzed the mRNA levels of IFN-α (IFNA2, IFNL1, IRF7) in control and sh5 cells and the mRNA levels

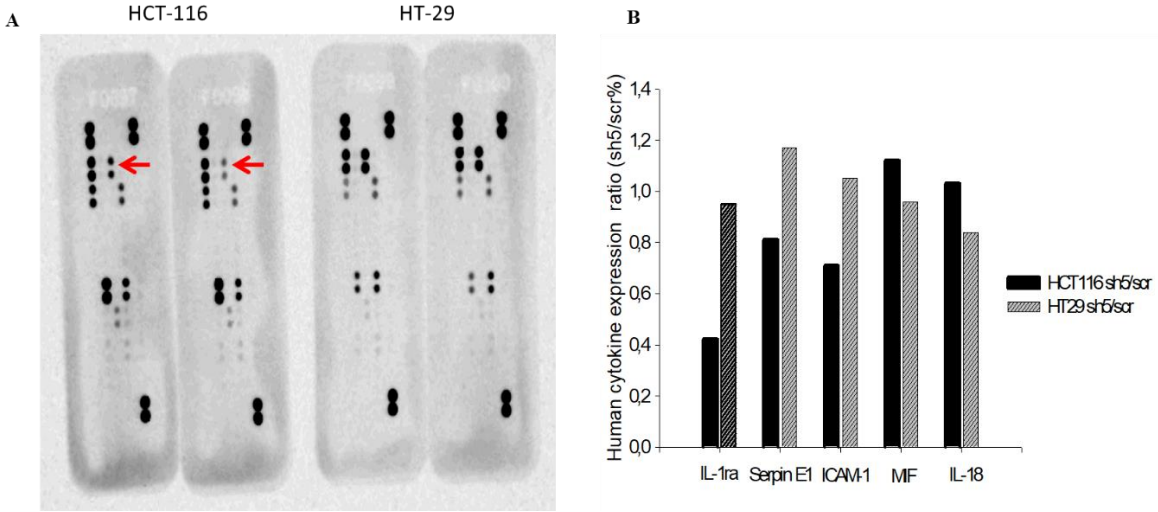

Figure 27 Levels of cytokine expression in control and DIAPH1-depleted cells. *Lysates from control and sh5 HCT-116 and HT-29 cells were analyzed for cytokines levels using the Human Cytokine Array Panel A from R&D Systems. (A) The spots of the upper and lower lay represent the reference signals.*

The other dots representing the cytokines are listed under https://resources.rndsystems.com/pdfs/datasheets/ary005b.pdf. The red arrow marks the signal for IL- 1ra. (B) Right panel: The human cytokine expression ratio of sh5 to control cells is shown. The expression levels were regarded as band intensities measured by ImageJ (Fiji) and the signals were detected using ImageQuant LAS 4000 Imager by electrochemiluminescence (ECL) detection system. The black bar: HCT-116 sh5/control ratio; the gray bar: HT-29 sh5/control ratio.

were quantified using RT-qPCR analysis. This analysis showed that in HCT-116 sh5 cells, the mRNA levels of IRF were increased approximately 1.5-fold compared to control cells, while decrease of IFNL1 and IFNA2 mRNA expression was detected (Fig. S 6). This three mRNA levels were all decreased in HT-29 sh5 cells, and IFNL1 mRNA expression was down-regulated by 37% (Fig. S 6). The IRF mRNA levels showed clearly opposite trends in DIIAPH1 knockdown cells compared to control cells in both HCT-116 and HT-29 cell lines (Fig. S 6).

Although the technique of RT-qPCR which involves measurement of cytokine mRNA transcript abundance, is relatively straightforward and quantitative, one of its major disadvantages is that the presence of RNA does not always accurately reflect protein levels [60]. Considering this fact, we analyzed the protein level of 36 cytokines, using a western-blot based cytokine array (Fig. 27A). The dot-signals intensities were evaluated with subtracting negative control using the base package of ImageJ (Fiji) and the ratio of intensities of sh5 cells to control cells was calculated. This evaluation revealed that the interleukin-1 receptor antagonist (IL-1ra, see red arrow in Fig. 27A) was regulated highest in both cell lines. In HCT-116 sh5 cells its expression was reduced by 60% but in HT-29 sh5 cells only by 20% (Fig. 27B).

4.9 Effect of DIAPH1 on MT-bundling assay

To analyze potential effects of DIAPH1 proteins on MT-bundling, labeled MTs were incubated with DIAPH1 proteins. This analysis showed that neither cross-linking nor bundling phenomenon occurred in GST-DIAPH1 proteins compared to MTs control (Fig. 28).

In summary these results show that the constrictively active FH2 domain of DIAH1 increased MT-polymerization, suggesting DIAPH1 controls spindle MT-dynamics by directly increasing MT-polymerization.

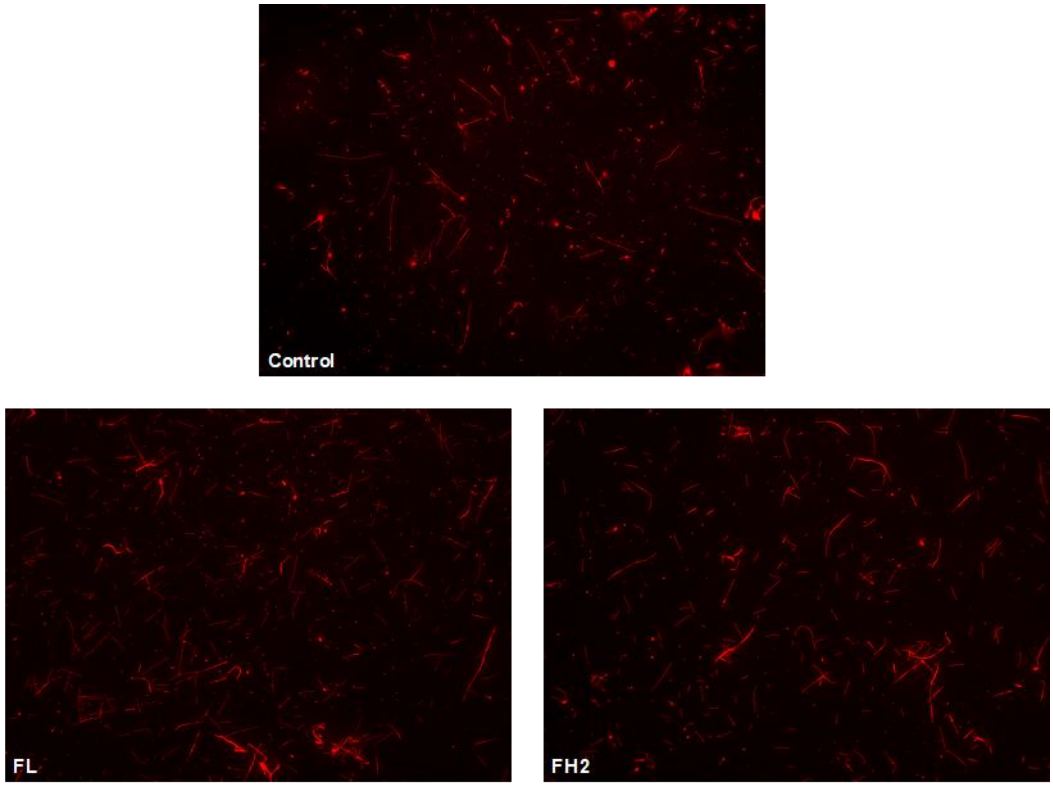

Figure 28 Effect of DIAPH1 FL and DIAPH1 FH2 on MT bundling assay. *GST-DIAPH1 FL and GST-DIAPH1 FH2 were rebuffed and the final concentration of GST-DIAPH1 FH2 were prepared as 0.45-fold as that of FL. Shown is the fluorescence images after coincubation of GST-DIAPH1 proteins with labeled MTs for 10 min, using fluorescence microscope.*

5 Discussion

Colorectal carcinoma (CRC) is ranking the third most commonly diagnosed cancer in males and the second in females. Although in some countries like United States, the overall mortality is declining, it is still increasing even in younger adults and in many other countries with limited resources and health infrastructure (https://www.uptodate.com/contents/colorectal-cancer-epidemiology-risk-factors-and-protective-factors). For those patients suffering from CRC, the rapid evolution of resistance to chemotherapy and molecularly targeted therapies limits the efficiency of neoadjuvant and cytotoxic therapies. This resistance can be caused by pre-existing resistance-mediating factors, dominant resistance mutations as well as various therapy-induced adaptive responses occurring during cancer treatment. For instance, activation of the compensatory signaling pathways would promote tumor tolerance [61]. Therapeutic agents targeting spindle microtubules have already been shown efficiency in clinical applications, however, the biggest challenge of those chemicals is still drug resistance [62]. Taxanes are one of the most widely

used microtubule-targeted agents, and have been shown to induce mitotic arrest [63]. This mitotic arrest results from activation of SAC (spindle assembly checkpoint) and could ultimately induce cell death (as described in section 1.3) [63]. The mechanistic basis of this mitosis-blockage, leading to subsequent death, remains unexplored. However, we acknowledge that the acquisition of tumor resistance to the microtubule-targeted drugs is associated with chromosomal diversity, mediated by persistent chromosomal instability (CIN) in CRC [32,64]. It is well studied that altered regulation of spindle MT dynamics has an essential role in the generation of CIN. Thus, cytoskeletal proteins, regulating dynamics of microtubules, become key targets for anticancer therapy (see more details in section 1.3). Since CRC, especially mCRC, is commonly difficult to treat due to multi-drug resistances; orthogonal therapy that is able to attack the cancer through multiple independent pathways, may be a promising option [61]. With reference to the drug resistance, proteins that perform non-redundant function in directly controlling the complex process of chromosome segregation, may be very interesting targets [50].

5.1 DIAPH1 co-localized with spindle MTs and regulated MT- dynamics

In this study, we analyzed the role of DIAPH1 in regulating spindle MT dynamics and CIN. Our results showed that DIAPH1 localized to the spindle apparatus, but not to the spindle pole centrosome (Fig. 16). In consistent with our results, Kato et al. revealed that DIAPH1 localized to the mitotic spindle of HeLa cells, independent of Rho mediated stimulation, and this localization was seen from prophase to telophase [55]. However, it was unclear whether DIAPH1 localized to all of these three types of spindle microtubules (the kinetochore MTs, the interpolar MTs, and the astral MTs), due to the limited resolution of fluorescence microscopy. Thus, further studies using high resolution microscope are necessary.

Since DIAPH1 co-localized in mitotic MTs, it was possible that this protein also controls its dynamics. Based on this consideration, MT-dynamic assays were performed. The results of these experiments showed that depletion of DIAPH1 decreased the speed of spindle MT movement (Fig. 18). Moreover, the differences of MT movement speed between HCT-116 control and knockdown cells were kept constantly from early metaphase until anaphase onset. In contrast, in chromosomal instable HT-29 cells, the differences between control and knockdown cells disappeared before anaphase onset (Fig. 18B). This result indicates that the effect of DIAPH1 depletion on MT dynamics is more significant in euploid cells.

It is important to mention that the analysis of spindle MT dynamics was performed in non-stimulated cells. Since our previous studies revealed that the isoform 2 of DIAPH (DIAPH2)

controlled MT-dynamics even in its auto-inhibited form. It was also likely that was also true for DIAPH1 protein. To address this possibility, we performed a MT polymerization assay *in vitro* employing GST-DIAPH1 FL protein, and constitutively active GST-DIAPH1 FH2 protein as a positive control. Comparing with the function of FH2 domain on MT polymerization, auto-inhibited GST-DIAPH1 FL had no effect (Fig. 20B). From these data we conclude that the effect of DIAPH1 on the speed of spindle MTs should depend on cellular stimulation, requiring the activation of small GTPase RhoA activation to convert the GST-DIAPH FL into the active conformation. However, future experiments are required to identify these, probably cell-cycle specific, cellular signals.

5.2 Role of DIAPH1 in chromosomal instability

Precise regulation of spindle MT dynamics could align the chromosomes at equatorial plates and distribute them equally into daughter cells, which is essential for normal cell division. Altered MT dynamics could lead to chromosomal instability (CIN) due to improper kinetochore microtubule (KT-MT) attachment to chromosomes or insufficient power to separate chromosomes. In CIN tumor cells, the alignment of chromosomes is mostly impaired, leading to chromosome segregation errors and finally to unequal distribution of chromosomes to daughter cells[56,65]. In order to find out whether DIAPH1-controlled spindle MT-dynamics may be involved in regulation of CIN, number of cells with chromosome alignment and mis-segregation were compared between control and DIAPH1 depleted cells. Interestingly, our data shows that depletion of the DIAPH1 impaired chromosomal alignment (Fig. 21) and further increased the error rates of chromosomal mis-segregation (Fig. 22) in both HCT-116 cells and HT-29 cells. These results indicate a role of DIAPH1 in CIN by controlling spindle microtubule dynamics, which probably correlated with speed of spindle MTs movement (Fig. 18) and/or attachment of kinetochore microtubules (KT-MT) to kinetochores [45].

During cell mitosis, each pair of sister kinetochores from opposing spindle poles is incorporated into the nascent spindle and driven by bipolar microtubule bundles in mitosis, mediating faithful chromosome capture and transport [22,66,66]. Thus, precise kinetochore attachment to spindle MTs is essential for proper chromosomal alignment and segregation. In the studies of figuring out the role of Rho GTPases in nuclear division, Yasuda et al. found that mDia 3 played an important role in proper chromosome alignment and segregation by regulating bi-orientated MT attachment to kinetochores in a cell division control protein 42 homolog (cdc42) stimulation manner [43]. However, they did not show the function of DIAPH1 in chromosome segregation

during mitotic cell division, and most researchers focused more on its role in cytoplasm of interphase cells or polar spindle microtubules [43,55,67]. Although we are the first to show an essential role of DIAPH1 in CIN, we did not compare the kinetochore attachments to chromosomes between control and DIAPH1-depleted cells, due to the limited microscopy resolution (see also section 5.1). To address this possibility, high resolution microscope like Stimulated Emission Depletion (STED), is needed to identify the KT-MT attachment in mitosis. Alternately, co-localization of DIAPH1 with Mad-2, a mitotic spindle-checkpoint protein 2, and/or with CENP-A could be analyzed. Reduced spindle MT-speed in DIAPH1-depleted cells contribute to explain the strong effect of DIAPH1 on chromosome alignment and segregation (Fig. 18, 21-22). Reduced spindle MT speed causes the delay of chromosome alignment, leading to increased error rate of chromosome segregation and further chromosomal instability [68]. This was due to insufficient time to establish chromosome bi-orientation in the spindle equator [68].

Generally, when all kinetochores (KTs) become stably attached to the KT microtubules and chromosomes are aligned at the spindle plate, cell cycle progression could step to anaphase. Otherwise, the spindle assembly checkpoint (SAC) would be activated to stop this process [23]. This physiology behavior could guarantee accurate chromosome segregation, maintaining genomic stability [23]. We found mis-aligned chromosomes developing to mis-segregated chromosomes (Fig. 21-22), indicating SAC did not work correctly in HCT-116 and in HT-29 cells. To examined if improper chromosome alignment and segregation results in M-phase arrest, cellular viability was measured in HCT-116 and HT-29 control and DIAPH1-depleted cells. Interestingly, our results show that there was no difference between DIAPH1 knockdown cells and control cells regarding cell growth rate (Fig. 25A). This result strongly indicates that DIAPH1 depletion-induced misalignment of chromosomes did not activate SAC. Thus, metaphase cells with misaligned chromosomes had escaped surveillance, keeping the errors of unattached KTs and proceeding to anaphase. One explanation of this observation is that most of the chromosomes attaching the same kinetochore fiber extending from two opposite spindle pole, and this attachment could escape the SAC surveillance [29,30]. On the other hand, our previous study revealed that DIAPH2 depletion reduced proliferation of HT-29 cells, due to M-phase delay, which was required to repair defective attachment of spindle fibers to the chromosomes [45]. The fact that the failures in spindle-MT homeostasis induced by knockdown of DIAPH2 could be repaired, indicated that the impact of DIAPH2 is weaker than that of DIAPH1. However, further research is necessary to prove this assumption.

Our analysis of chromosome number showed that there were two chromosomes lost in chromosomal stable HCT-116 sh5 cells, while no significant differences were found in chromosomal unstable HT-29 cells. The lost chromosome was arguably the Y chromosome (Fig. 23, S4). Interestingly, we did not observe this in HCT-116 sh4 cell line, exhibiting a lower DIAPH1 down-regulation. Thus, sufficiently reduced levels of DIAPH1 seem to be required to affect chromosome distribution. Moreover, number of cells having acentric chromosomes was similar in both DIAPH1 depleted cells and control cells (Fig. S 3), indicating that most of the CIN phenotypes are arising from the alteration of numerical chromosomes. This assumption is confirmed by researches of Lengauer et al. and Bakhoum et al. [18,19] Due to the technology limitation, we were not able to detect structural CIN in detail, like gene translocation or point mutation. An association of loss of Y chromosome (LOY) has already been reported in both hematological cancers and solid tumors, like leukemias, hepatocellular carcinoma. Since LOY probably is involved in the oncogenic process of males, it could serve as a marker for cancer classification and clinical prognosis [69,70].

In summary, we conclude that DIAPH1 depletion could increase the rate of chromosomal misalignment and mis-segregation of CRC, thereby contributing to CIN by regulating spindle MT dynamics.

5.3 Effect of DIAPH1 on cytokines expression

Our analysis reveals that DIAPH1 depletion increased the number of cells having micronuclei (MNi) formation (see Figure 24). These MNi arise from lagging chromosomes (see the white arrow in Figure 22A) that are not incorporated into the nuclei but are enveloped by an own leaky membrane [56]. In most cases, these MNi collapse and thereby release free DNA into the cytosol [56], inducing expression of pro-inflammatory cytokines [56,71,72]. To evaluate whether increased number of MNi were found in DIAPH1 depleted cells, altered cytokine expression, protein levels of 36 cytokines were analyzed by using a western-blot based cytokine array. This analysis revealed that IL-1ra was the only protein whose expression was substantially altered in DIAPH1-depleted cells. In HCT-116 sh5 cells, its expression was decreased by 60% and in HT-29 sh5 cells by 20%.

Since IL-1ra blocks IL-1R signaling in monocytes/ macrophages [73], it is very likely that reduction of IL-1ra expression in the cell supernatants will enhance the activation of monocytes/ macrophages cells. Blood monocytes then will show stronger cytotoxic activity against tumor cells, breaking the “cancer-induced tolerance” by increasing expression of Interleukin-1 [74]. This

kind of tolerance occurs when tumor cells deactivate or suppress the anti-cancer activity of tumor-infiltrating macrophages (TIMs) in the tumor microenvironments (TME) [75,76]. It is known that IL-1 has different physiological and biological effects regarding both pro- and anti-tumorigenic effects. These effects depend on tumor type, stage of tumor progression and TME[77,78]. To get deeper insight into the role of IL-1ra in DIAPH1 depleted cells, the immune response in these cells should be investigated in detail. In case future results will show that DIAPH1 depletion increases immune cell response, a combination therapy of DIAPH1 inhibition and immune therapy could be developed (for details, see below).

5.4 Potential role of DIAPH1 in colorectal carcinoma treatment

Eighty-five percent of colorectal carcinoma patients are highly chromosomally instable, and it is well-examined that CIN correlates with poor prognosis because of high aggressiveness and drug-resistant of tumors [11]. Furthermore, CIN cells are often tolerant against immune cell attack [76]. Our results, showing that depletion of DIAPH1 increases CIN, pre-dominantly in chromosomal stable cells, indicate that high levels of DIAPH1 protect against CIN. Thus, high DIAPH1 expression should be associated with good prognosis. However, our previous results revealed the opposite. High DIAPH1 expression in colorectal carcinoma patients was associated with poor prognosis and knock-down of DIAPH1 in HCT-116 cells nearly completely blocked metastasis in SCID mice. These apparently contractionary findings suggest that CIN could also be related to good prognosis under certain conditions, and this effect of CIN on tumor cell malignancy depends on the CIN rate. However, one should notice that the mechanism of DIAPH1 controlling metastasis is very complex. While depletion of DIAPH1 blocked metastasis by regulating interphase MT dynamics, its effect on CIN was associated with its regulation of spindle MT dynamics. Even though, how CIN improves the prognosis is still unclear. It is possible that when exceeding a certain threshold, CIN leads to cell apoptosis or enhances the immune cell activation [11]. Birkbak et al. analyzed the CIN 70 scores of various cancers and supported this kind of theoretical CIN thresholds. They figured out that poorest patient outcomes were associated with intermediate levels of CIN, while patients with extreme CIN tumors had improved prognosis [79]. Based on these considerations, one could assume that increased CIN, induced after depletion of DIAPH1 and exceeded the CIN threshold, could result in induction of apoptosis. However, we found that growth of primary tumors in SCID mice was not different between control and DIAPH1-depleted HCT-116 cells and also viability of cultured tumor cells was the same between these cell lines. In addition, our luminescent assay for analyzing the caspase 3/7 activity did not show any difference between control and DIAPH1 depleted cells in both cell

lines. Thus, we can rule out that increased CIN induced by DIAPH1 depletion induced apoptosis. In summary, future studies are necessary to elucidate the apparently contradictory finding that high levels of DIAPH1 reduces CIN but increases metastasis.

Most colorectal carcinoma cells show low sensitivity to paclitaxel treatment, but the underlying mechanism has not been elucidated yet [11]. Interestingly, our results revealed that depletion of DIAPH1 decreased sensitivity to paclitaxel treatment in chromosomally stable HCT-116, but not in chromosomally instable HT-29 cells (Fig. 26). This finding can be explained by the fact that highly chromosomally instable HT-29 cells were already resistant to paclitaxel. Thus, DIAPH1 depletion could not further enhance paclitaxel resistance. In conclusion, our data indicates that depletion of DIAPH1 can induce chromosomal instability, associated with decreased paclitaxel sensitivity in chromosomally stable cells. However, although its depletion increased CIN in chromosomally instable cells, it could not further increase resistance to paclitaxel. These results indicate that the mechanism of DIAPH1 on paclitaxel resistance is different between chromosomally stable and unstable CRCs. Future studies unravelling the mechanism behind this are required.

Likewise, our finding that DIAPH1-depleted cells show a higher IL-ra concentration also requires further investigation. In the first step, the IL-1 response in immune cells co-incubated with control and DIAPH1-depleted cells has to be examined. Thereafter, it has to be shown whether immune cells pre-incubated with DIAPH1-depleted cells exhibit an increased potential to attack tumor cells. In case we will indeed find an increased immune cell response in DIAPH1 depleted cells, this result has to be confirmed with at least three further DIAPH1 knockdown cells. Thereafter, immune therapies could be developed, targeting tumor cells with low DIAPH1 expression.

5.5 Limitation

This study revealed a role of DIAPH1 in increasing CIN rates by regulating spindle MT dynamics in colorectal carcinoma cells. Our results suggest that DIAPH1 depletion could impair chromosome alignment, contributing to chromosome mis-segregation and even chromosome lost. However, we do not know whether this effect of DIAPH1 depletion is only related to spindle MT-dynamics. Since KT-MT attachment also plays a crucial role in precise chromosome segregation, it is very likely that DIAPH1 depletion could impair the KT-MT attachment and hence affect chromosome alignment. To show this, high resolution microscopy is necessary to detect the specific localization of DIAPH1 and the KT-MT attachment to chromosomes.

Our results reveal that GST-DIAPH1 did not significantly affect MT polymerization in vitro comparing to GST-DIAPH1 FH2 (Fig. 20B). Our explanation is that this activity of GST-DIAPH1 needs RhoA stimulation. In addition, there was still unspecific protein background in the SDS-PAGE, and proteins formed insoluble aggregates or underwent degradation. To validate our results purification and stabilization of GST-DIAPH1 proteins should be improved.

In this study, we focus on the function of DIAPH1 depletion on CIN. CIN includes not only changes in whole chromosomes but also alteration of chromosome fragments, but we could only observe the chromosome number using chromosome preparation technique. Our karyotype analysis indicates that there are also chromosome fragments altered in DIAPH1 depleted cells, indicating that also structural CIN increased in these. To validate this, karyograms of a higher cell numbers should be analyzed.

Furthermore, we could not identify the other types of structural chromosome abnormality like chromosome translocations and/or insertions due to the limited techniques. Hence, in our study, CIN means altered chromosome number regardless of the chromosome integrity in the primary nucleus.

5.6 Outlook

5.6.1 Role of DIAPH1 for colorectal carcinoma cells on immune cell response

Our results show that the expression of IL-1ra in HCT-116 sh5 cells was significantly down-regulated while in HT-29 sh5 cells was slightly reduced. Most likely, this result is related to higher concentration of cytosolic DNA in HCT-116 sh5 cells comparing to HT-29 sh5 cells. To validate our assumption, concentration of cytosolic DNA collapsed from micronuclei have to be measured.

Since cancer-related tolerance in tumor microenvironment (TME) probably would be disrupted by enhanced anti-tumor activity of the monocyte cells, concentration of IL-1 should be measured after cell immune response. Therefore, IL-1 concentration in blood samples have to be compared after co-incubation with control and DIAPH1 depleted cells separately. As positive control, concentration of IL-1 in fresh blood samples after adding IL-1ra has to be measured.

IL-1R is mainly expressed by monocytes in blood and further by macrophages in tissue [73]. In case we will observe altered IL-1 concentration, monocytes have to be isolated from blood to further validate the IL-1 immune response mentioned above. Afterwards, isolated monocytes

will be co-cultured with both control and DIAPH1 depleted cells. If we observe increased IL-1 concentration after co-incubating with DIAPH1 knockdown cells, we can conclude that enhanced IL-1 immune response results from enhanced monocytes activation.

5.6.2 Impact of activated monocytes on the metastatic potential of colorectal carcinoma cells

If DIAPH1 depleted cells can alter monocyte activation, one can conclude that depletion of DIAPH1 can enhance tumor-attack ability from immune cells. To address this possibility, the potential metastasis ability of colorectal cells after co-incubation with monocytes have to be tested. For this purpose, isolated monocytes will be incubated with colorectal cells for 48 h, and a series of experiments representing metastasis ability will be analyzed. These experiments include transwell invasion assay, wound-healing migration assay, colony formation assay, analysis of proliferation, and 3-D-growth. We expect that reduced metastasis will be observed in DIAPH1 depleted cells after co-incubation with activated monocytes, which could indicate that depletion of DIAPH1 can reduce the metastatic potential of colorectal carcinoma cells by improving the immune responses to tumor.

5.6.3 Effect of pharmacologic DIAPH1 inhibition on the metastatic potential and on chromosome segregation of colorectal carcinoma cells

Our results show that depletion of DIAPH1 affected chromosome alignment and segregation by regulating spindle MT dynamics, while FH2 domain of DIAPH1 directly affect microtubule dynamics. To validate the effect of DIAPH1 on chromosomal stability, pharmacologic DIAPH1 inhibition, the small molecule inhibitor of Formin Homology 2 domains (SMIFH2) will be employed. Furthermore, corresponding metastatic potential of colorectal carcinoma cells, like transmigration, colony formation, will be analyzed. Since the effect of SMIFH2 on DIAPH1 is similar to depletion of DIAPH1, role of SMIFH2 in chromosome alignment, chromosome segregation and micronuclei formation will be assessed. In case the function of SMIFH2 on metastatic ability and chromosome segregation has a similar effect as DIAPH1 depletion, SMIFH2 could be a tool compound to develop anti-metastatic drugs.

6 Conclusion

In conclusion, our data indicate an essential role of DIAPH1 in CIN by regulating spindle MT dynamics. Depletion of DIAPH1 impairs chromosome alignment and segregation, contributing

to micronuclei formation in colorectal carcinoma cells. Furthermore, expression of IL-1ra was significantly reduced in chromosomal stable cells with DIAPH1 knock down (HCT-116 sh5 cell line), which probably enhances the tumor-attack ability of innate immune systems.

Tumor cells are characterized by phenotypic heterogeneity through genomic instability, and only mild CIN cells can contribute to tumor evolution and poor prognosis [11,80]. Interestingly, cells with DIAPH1 depletion showed lower sensitivity to paclitaxel treatment, most likely by decreasing the chromosomal diversity in HCT-116 cells. In this respect, DIAPH1 could be a promising therapy biomarker for paclitaxel treatment in chromosomal stable cells.

7 Abstract

Colorectal carcinoma (CRC) is the third leading cause of cancer-related death in the world and chemoresistant CRCs mostly are palliative. Chemoresistances arise, among others, by development of chromosomal instability (CIN), resulting in genomic diversity of tumor cell populations. CIN can be caused by mis-regulation of spindle-MT dynamics. Since spindle-MT dynamics are controlled by microtubule-associated proteins (MAPs), these proteins are interesting molecules for targeted therapy. Protein diaphanous homolog 1 (DIAPH1) belongs to the group of MAPs and preliminary data indicate that DIAPH1 is involved in the control of spindle-MT dynamics in CRCs. In this study, the role of DIAPH1 in spindle MT dynamics and CIN has been analyzed in detail.

For this purpose, spindle MT-dynamics, misalignment and mis-segregation of chromosomes were compared between control and DIAPH1-depleted cells. In addition, these cells were treated with the spindle poison paclitaxel, and then cell viability and apoptosis were measured. To figure out whether the activity of DIAPH1 depends on aneuploidy, we employed two cell lines: HCT-116 (chromosomal stable) and HT-29 (chromosomal instable). Our results reveal that DIAPH1 localized to spindle MTs, and depletion of DIAPH1 decreased the speed of spindle MTs movement during metaphase. In addition, DIAPH1 depletion increased chromosomal misalignment, mis-segregation and micronuclei formation in both cell lines. Moreover, in HCT-116 DIAPH1 k.d. 5 cells, two chromosomes were lost. Interestingly, although there was no significant difference in cell viability and apoptosis, HCT-116 DIAPH1 depleted cells had decreased sensitivity to paclitaxel exposure while HT-29 cells were resistant. In summary, depletion of DIAPH1 resulted in increased rates of CIN and decreased sensitivity to paclitaxel. These data strongly suggest that DIAPH1 controls chromosomal stability of CRC by regulating spindle-MT dynamics and thereby controls sensitivity to chemotherapeutics.

8 Zusammenfassung

Das kolorektale Karzinom (CRC) ist weltweit die dritthäufigste krebsbedingte Todesursache und Patienten mit chemoresistenten CRC sind in der Regel palliativ. Chemoresistenzen können unter anderem durch chromosomale Instabilität (CIN) und einer damit einhergehenden genomische Diversität der Tumorzell-Populationen entstehen. CIN wird unter anderem durch fehlerhafte Regulation der Dynamik von Spindelmikrotubuli (MTs) verursacht. Da die Spindel-MT-Dynamik durch Mikrotubuli-assoziierte Proteine (MAPs) kontrolliert wird, sind MAPs interessante Zielmoleküle zur Therapie von CIN Tumoren. Protein diaphanous homolog 1 (DIAPH1), gehört zu den MAPs und vorläufige Daten wiesen darauf hin, dass DIAPH1 an der Regulation der Spindel-MT-Dynamik in CRC-Zellen beteiligt sein könnte. In dieser Arbeit wurde die Funktion von DIAPH1 bei CIN und der Spindel-MT Dynamik im Detail untersucht.

Hierzu wurde die Spindel-Dynamik, das chromosomale Missalignment und die fehlerhafte Trennung der Chromosomen zwischen Kontroll- und DIAPH1-depletierten Zellen verglichen. Außerdem wurden CRC-Zellen mit den Spindelgift Paclitaxel behandelt und Viabilität und Apoptose untersucht. Um zu zeigen, ob die Aktivität von DIAPH1 abhängig von einer Aneuploidie ist, verwendeten wir zwei Zelllinien: HCT-116 (chromosomal stabil) und HT-29 (chromosomal instabil). Unsere Ergebnisse zeigten, dass DIAPH1 an Spindel-MTs lokalisiert und dass dessen Depletion die Geschwindigkeit der Spindel-MT-Dynamik in der Metaphase verringerte. Außerdem erhöhte die DIAPH1-Depletion das chromosomale Missalignment, die fehlerhafte Trennung der Chromosomen und die Bildung von Mikronuklei in beiden Zelllinien. Darüber hinaus gingen in HCT-116 DIAPH1 k.d.5-Zellen zwei Chromosomen verloren. Obwohl Kontroll- und DIAPH1-depletierte Zellen keine Unterschiede in Viabilität und Apoptose zeigten, wiesen HCT-116 DIAPH1-depletierte Zellen eine geringere Empfindlichkeit gegenüber Paclitaxel auf, HT-29-Zellen hingegen waren resistent. Zusammenfassend konnte gezeigt werden, dass die Depletion von DIAPH1 zu einer erhöhten CIN-Rate und einer verringerten Sensitivität gegenüber Paclitaxel führt. Diese Daten weisen stark darauf hin, dass DIAPH1 die chromosomale Stabilität von CRC durch Regulation der Spindel-MT Dynamik kontrolliert und hierdurch die Sensitivität gegenüber Chemotherapeutika reguliert.

9 Appendix

9.1 Supplementary data

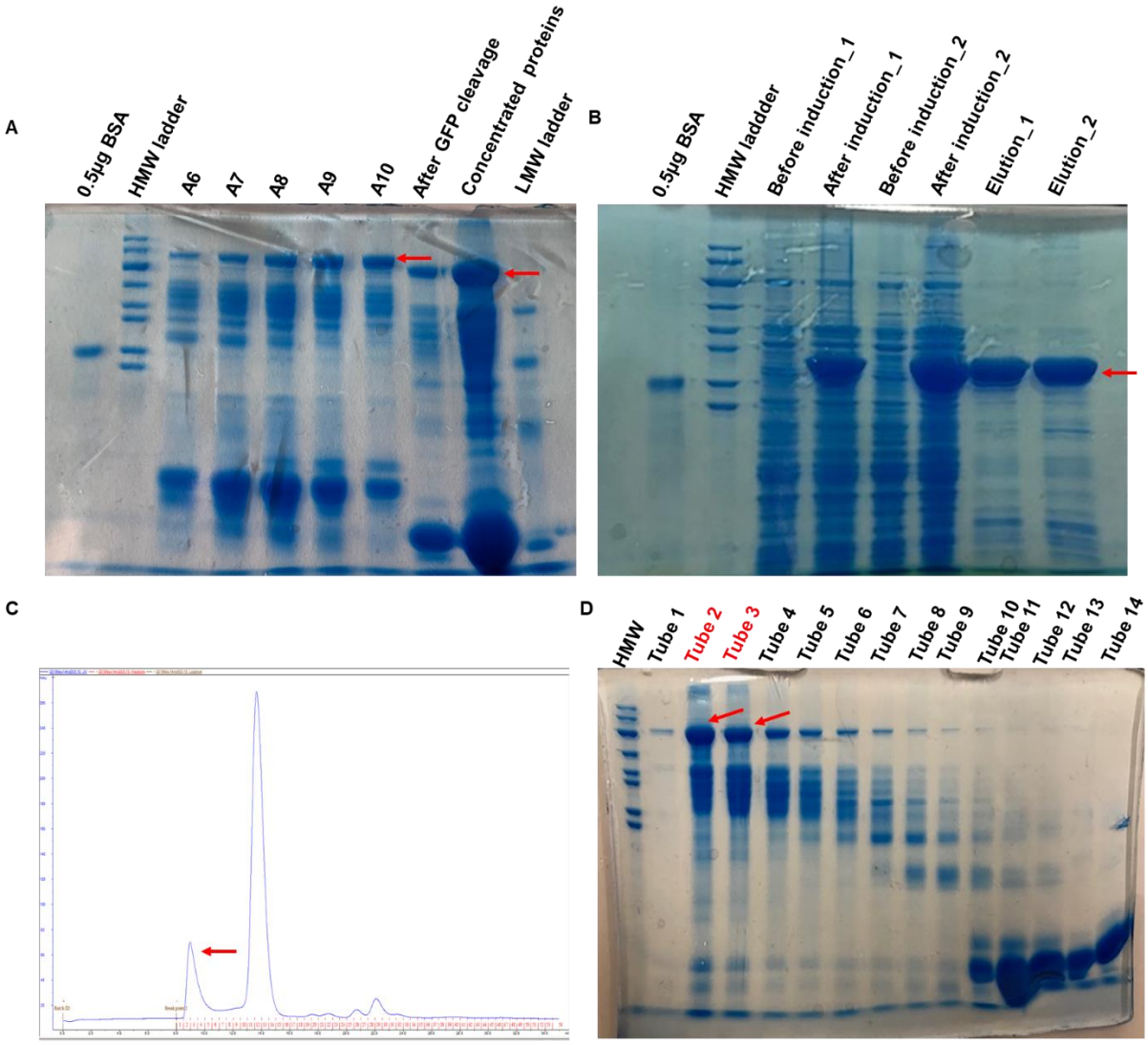

Figure S 1 Expression and purification of recombinant GFP-DIAPH1 proteins. *GFP-DIAPH1 FL, GFP-DIAPH1 FH2 or GFP-DIAPH1 dFH2 genes were cloned into the vector pSF421_10× His_GFP, expressed as GFP-fusion protein in E.coli; and then purified by affinity column chromatography (ACC) and size exclusion chromatography (SEC). (A-B) Shown are SDS-PAGEs of 20 µl elution fraction of GFP-DIAPH1 FL and GFP-DIAPH1 FH2 separately (indicated by the red arrow). (C) Shown is SEC chromatogram of GFP-DIAPH1 FL. The peak is indicated by the red arrow. (D) The SDS-PAGE of 20 µl elution fraction from (C) is shown. The chromatogram curve of GFP-DIAPH protein in tube 2 and 3 is corresponded to the peak in (C).*

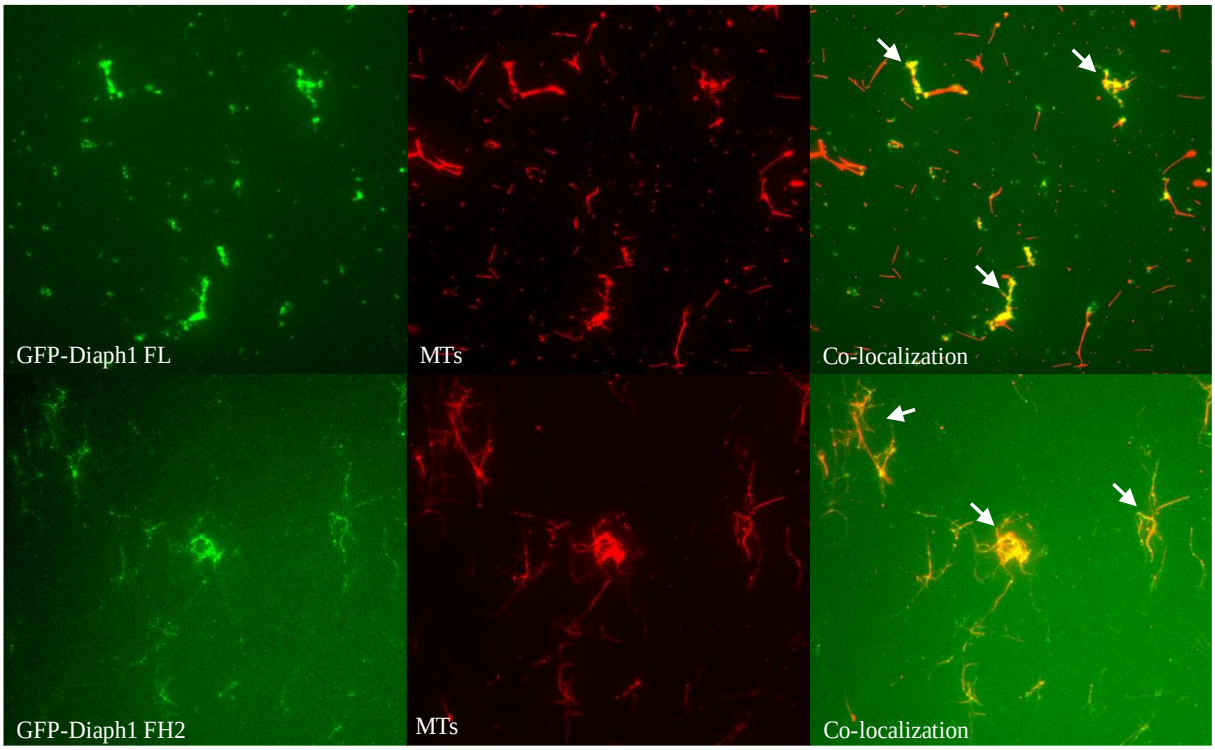

Figure S 2 Extracellular co-localization of GFP-Diaph1 with MTs. *The mixtures of labeled MTs and GFP-Diaph1 proteins were mixed and added into Poly-L-lysine coated chamber slides. GFP-Diaph1 proteins were detected at 488nm (green channel) while the labeled MTs were detected at 658 nm (red channel). The co-localization analysis was performed based on the overlapping fluorescence signals from MTs and GFP-Diaph1 protein. The images of GFP-Diaph1 FL/FH2, MTs and overlapping fluorescence are shown separately. The examples of co-localization are marked by white arrow. This assay was repeated twice with different preparations of labeled MTs.*

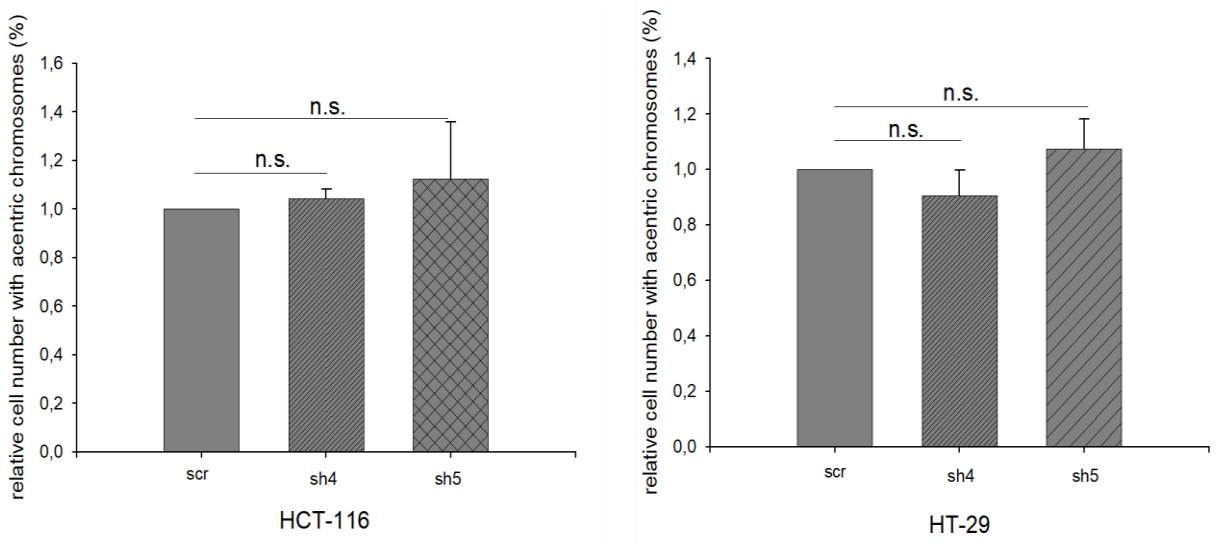

Figure S 3 Normalized number of anaphase cells with acentric chromosomes. *Images of cells with mis-segregated chromosomes (total at least 60 cells for each cell line, see in Fig. 23) were analyzed. The normalized percentage of anaphase cells with mis-segregated chromosomes without centromere to control levels is shown. Data were shown as mean ± SD. n.s. not significant.*

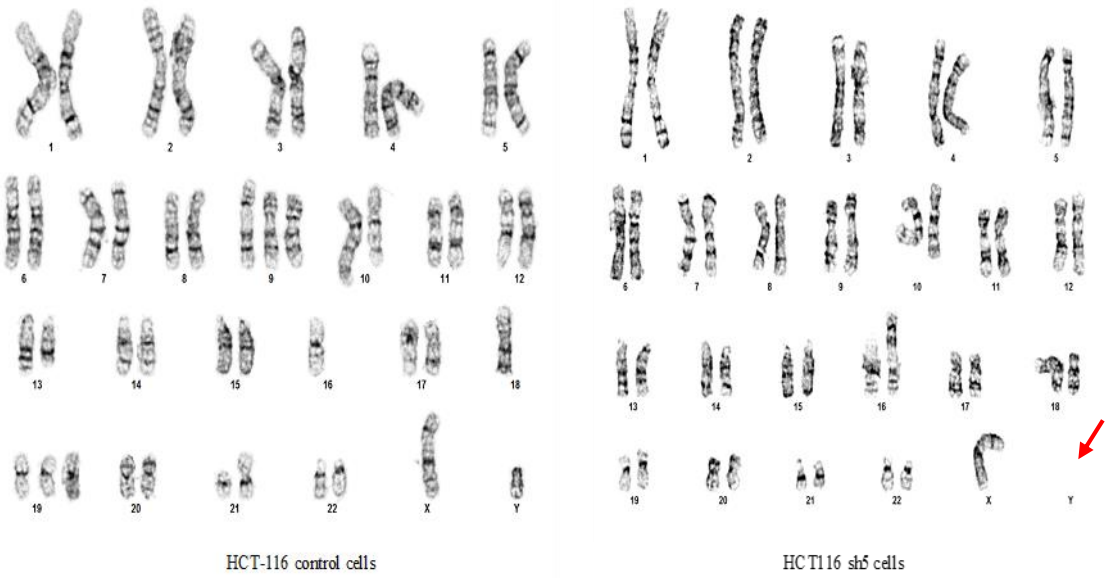

Figure S 4 Karyotype analysis of control and DIAPH1 depleted cells. *Cells were blocked in mitosis and chromosomes were stained with Giemsa dye with AT-rich (A: Adenine, T: Thymine) regions producing a dark band. In HCT-116 sh5 cells, Y chromosome is lost (indicated by the red arrow). Left panel: One presentative karyogram of HCT-116 control cells. Right panel: One presentative karyogram of HCT-116 sh5 cells. Karyotype analysis of control and DIAPH1 depleted cells were from at least 5 cells separately. This analysis was performed in collaboration with the Institute of Human Genetics at Universitätsklinikum Hamburg-Eppendorf (UKE).*

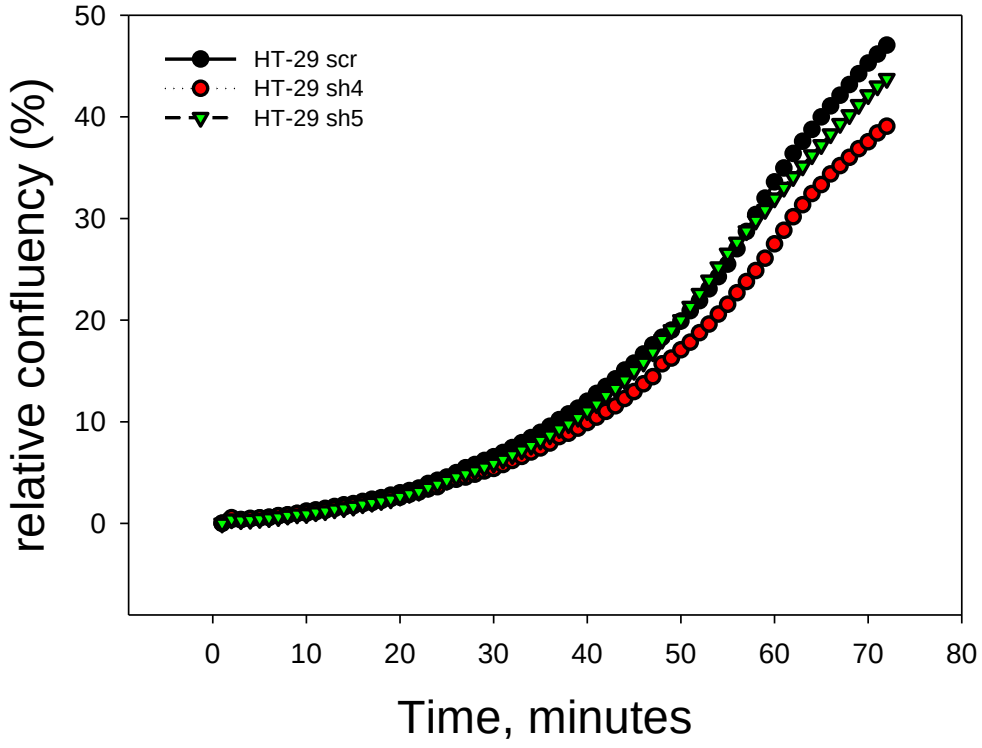

Figure S 5 Effect of DIAPH1 on cell proliferation. *To analyze cell proliferation, 2.5 × 10^3 cells in 100 µl per well were seeded in 96-well microplates and proliferation was analyzed by measuring the cell confluence using the software IncuCyte Zoom 2016B. Shown is the HT-29 cell proliferation for 7 days. Values at the starting point (t=0) were subtracted in corresponding cell line.*

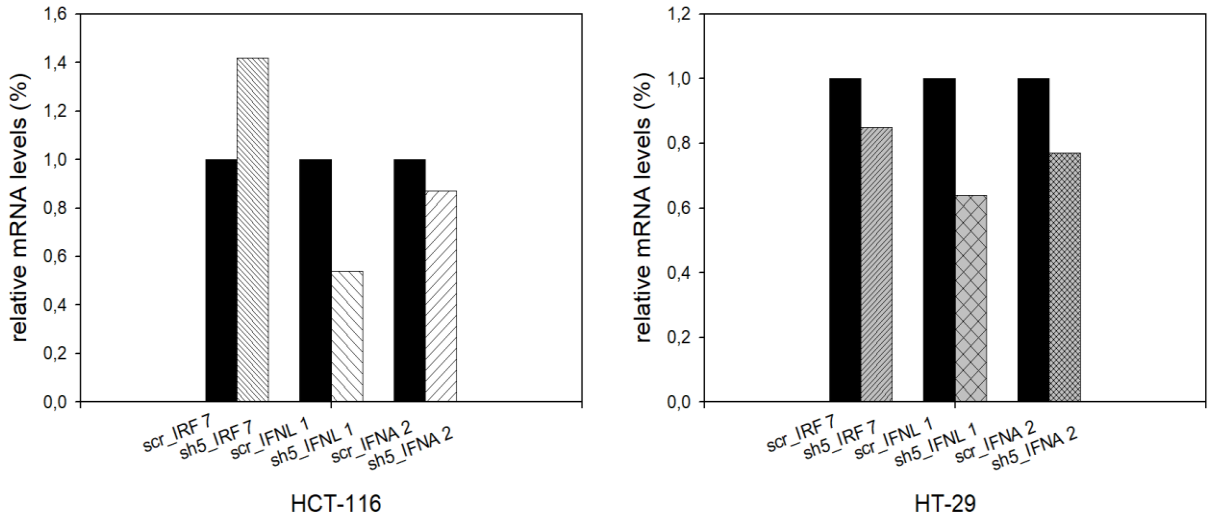

Figure S 6 Quantification of IFN-α mRNA by RT-qPCR. *Cellular RNAs were extracted from fresh cell lysates with the NucleoSpin RNA Kit, reversely transcribe into cDNA, and quantitative RT-PCR analysis was carried out with the cDNA from control cells as a reference sample while mRNA levels of GAPDH as an internal reference. (A, B) Left panel: The amplification plot of target genes (IFNA2, IFNL1, IRF7 and GAPDH) is shown. Right panel: Corresponding mRNA levels were shown separately.*

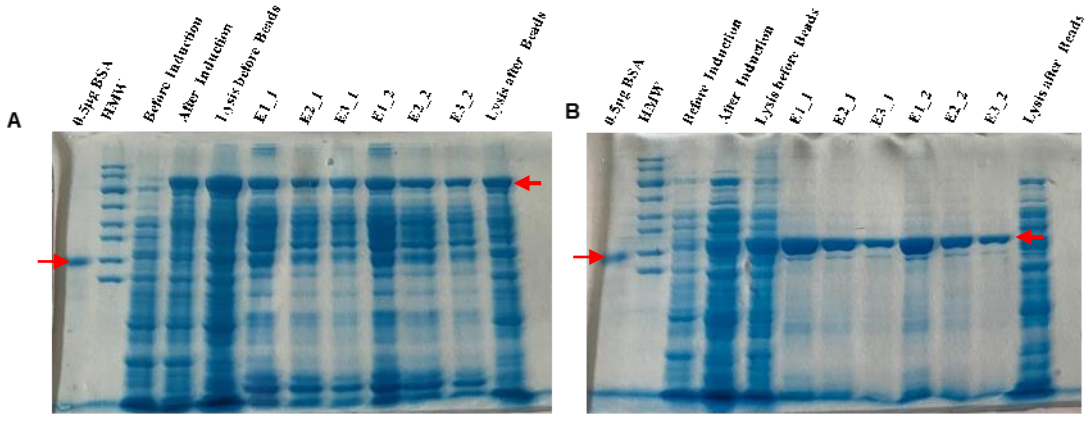

C

	E1 Concentraion (μg/20μL)	E1 Concentraion (mg/mL)
GST-Diaph1 FL	1.5	0.075
GST-Diaph1 FH2	2.0	0.1

Figure S 7 Expression and purification of recombinant GST-DIAPH1 proteins. *DIAPH1 full length (FL), DIAPH1 FH2 domain or DIAPH1 dFH2 genes were cloned into the vector pGEX-6PA, expressed as GST-fusion protein in E.coli and purified by glutathione affinity. (A, B) Shown are bands of 20 μl elution fraction on SDS-PAGE gels. Bands of GST-DIAPH1 FL (left) and GST-DIAPH1 FH2 proteins (right) were indicated by the black arrow separately. (C) The concentrations of the first elution fraction of GST-DIAPH1 proteins were estimated using 0.5 μg BSA (indicated by red arrow) as a standard, and shown as mg/ml.*

9.2 List of abbreviations

3D	three-dimensional
5-Fu	5-fluorouracil
A	Adenine
aa	amino acid
ACC	affinity column chromatography
ANOVA	Analysis of Variance
APC/C	Anaphase Promoting Complex/Cyclosome
APS	ammonium persulfate
BLI	bioluminescence imaging
bp	base pair
BSA	bovine serum albumin
cdc42	cell division control protein 42 homolog
CENPA	centromere protein A
cGAS	cyclic GMP-AMP synthase
CIN	chromosomal instability
c-MET	mesenchymal–epithelial transition factor
CRC	colorectal carcinoma
DAD	diaphanous autoregulatory domain
DAPI	4',6-diamidino-2-phenylindole
DNA	deoxyribonucleic acid
dFH2	deleted formin homology 2

DIAPH1	diaphanous homolog 1
DID	diaphanous inhibitory domain
dNTP	deoxynucleotide
DRF	diaphanous-related formin
dNTP	Desoxynucleosidtriphosphate
DTT	dithiothreitol
E. coli	*Escherichia coli*
ECL	enhanced chemiluminescence
ECM	extracellular matrix
EDTA	ethylenediaminetetraacetic acid
EGF	epidermal growth factor
EGFR	epidermal growth factor receptor
ELISA	enzyme-linked immunosorbent assay
EMT	epithelial-mesenchymal transition
FACS	fluorescence-activated cell sorting
FCS	fetal calf serum
FDA	Food and Drug Administration
FH2	formin homology 2
FL	full length
G-actin	globular actin
GFP	green fluorescent protein
GTP	guanosine trisphosphate

H	hour
HGF	hepatocyte growth factor
HMW	high molecular weight
HRP	horseradish peroxidase
HSC	heat shock cognate
Interleukin-1	IL-1
IL-1R	interleukin-1 receptor
IL-1ra	interleukin-1 receptor antagonist
ITH	intratumoral heterogeneity
Kb	kilo bases
KCl	potassium chloride
kDa	kilo Dalton
Kif2b	kinesin family member 2b
KLD	Kinase-Ligase-Dpnl
KT-MT	kinetochore microtubules
L	liter
IGF	insulin-like growth factor
IGF-1R	insulin-like growth factor 1receptor
LB	Luria Broth
LOY	loss of Y chromosome
M	milli
M	molar

M-Per	mammalian protein extraction reagent
MAPs	microtubule associated proteins
MCAK	mitotic centromere associated kinesin
MCC	mitotic checkpoint complex
MMR	mismatch repair
MSI	microsatellite instability
m	micro
MNi	micronuclei
Min	minute
mCRC	metastatic colorectal carcinoma
MTD	maximum tolerated doses
MTI	microtubule inhibitors
MTOC	microtubule-organizing center
MTs	microtubules
N-terminus	amino-terminus
OD	optic density
OS	overall survival
PBS	phosphate buffered saline
PCR	polymerase chain reaction
PDOs	patient-derived organoids
PH	pleckstrin homology
PI	Protease Inhibitor

PMSF	phenylmethylsulfonyl fluoride
PS	Phosphatase Stop
PTX	Paclitaxel
RBD	Rho-binding domain
RNA	ribonucleic acid
rpm	rounds per minute
RT	room temperature
TIMs	tumor-infiltrating macrophages
TGF	transforming growth factor
s	second
SAC	spindle assembly checkpoint
SEC	size exclusion chromatography
SEM	standard error of the mean
SDS	sodium dodecyl sulfate
SDS-PAGE	sodium dodecyl sulfate polyacrylamide gel electrophoresis
SLIC	sequence- and ligation-independent cloning
SMIFH2	small molecule inhibitor of Formin Homology 2 domains
STED	Stimulated Emission Depletion
T	time
T	Thymine
TAE	Tris-Acetate-EDTA-Buffer
TEMED	N, N, N’, N’ Tetramethylethylene-1,2-diamine

TME	tumor microenvironment
UV	ultraviolett
v/v	volume/volume
VEGF	vascular endothelial growth factor
VEGFR	vascular endothelial growth factor receptor
wt	wild type

9.3 List of figures

to recruit active Kif2b and then inactivate the MCAK, thereby destabilizing spindle MTs for the correction of improper kinetochore attachments. Upon metaphase, generation of high tension by bi-orientation attachments, exceeding the extent limit of the Aurora B kinase activity gradient, could release the Kif2b from kinetochores. In the meantime, a subgroup of MCAK is activated and localizes to centromere, correcting the remaining attachment errors. Kinetochores are shown in grey, microtubules are shown in green, active Kif2b is shown in blue, inactive MCAK is shown in yellow, active MCAK is shown in orange and activity gradient of Aurora B is shown in red. Kif2b: kinesin family member 2b; MCAK/ Kif2c: mitotic centromere associated kinesin [19].

Figure 9 Schematic diagram of three major pathways to chemotherapy resistance*. Innate resistance is the inherency of tumor cells to tolerate chromosomal instability and probably even the chemotherapy agents, allowing tumor growth and progression. Due to high initial chromosomal diversity prior to chemical agents, a subgroup of cells intrinsically carrying the drug resistance are very likely to achieve the adaptive resistance, continuing to grow in the presence of chemotherapeutic agents. Acquired resistance occurs when a subset of cells achieving the drug resistance are generated during cancer treatments, and this resistance does not exist prior to treatments. This process may be promoted by a mutant phenotype that can generate genetic diversity mediated via genome mutation or rearrangements, such as CIN. Chemotherapy-resistant tumor cells are shown in red; chemotherapy-sensitive tumor cells are shown in brown; CIN+ cells with potential resistance are shown in blue* [27].

Figure 10 Cartoon of MT dynamic instability driven by GTP hydrolysis. *(a) Conformational switch of αβ-heterodimers accompanying by cycles of GTP hydrolysis. In the GDP state, the interface of αβ-tubulin dimer achieves a slight curvature (indicated with curved arrow) from the straight status in the GTP state. (b) The transitions between MTs assembly and disassembly at the plus ends. Physiologically, GTP-tubulin dimers (shown in green) assemble on the MT plus ends along with GTP hydrolysis, and this process is termed rescue event. In the catastrophe phase, GDP-tubulin dimers (shown in blue) curl and peel off the plus ends, starting the MT shrinkage* [25].

Figure 11 Scheme of DIAPH domains in regulating actin nucleation. *Dia-inhibitory-domain (DID) and diaphanous autoregulatory domain (DAD) interact and prevent binding of profilin/actin to the FH1 and binding of F-actin to FH2 domains. After binding of GTPases of the Rho family, the interaction of the DID and DAD domain is disrupted and the FH1/FH2 domains are released* [38].

Figure 12 Reduced metastasis in SCID mice injected with HCT-116 DIAPH1 depleted cells. *In SCID mice injected with luciferase-over-expressing HCT-116 DIAPH1-depleted (D5) cells, histological examinations did not show any metastatic cells at different potential metastatic locations, such as lungs and livers. In contrast, the bioluminescence imaging (BLI) analysis showed strong signals at different distant locations in the mice injected with HCT-116 control cells. Moreover, the histological examinations of corresponding tissues showed abundant CRC cells (indicated as "M") in both lungs (upper panel) and livers (lower panel) respectively* [46].

Figure 13 Scheme of DIAPH1 domains and its binding to microtubules. *(A) Scheme of DIAPH1 domains. GBD: GTPase binding domain, DID: Diaphanous Inhibitory Domain domain, DD: Dimerization Domain. CC: Coiled Coiled, FH1: Formin homology do-main 1, FH2: Formin homology domain 2, DAD: Diaphanous Autoregulatory; (B) DIAPH1 promotes cellular adhesion by stabilizing MTs. The DIAPH1 could bind to MTs via the FH2 domain, and facilitate MT stabilization even in absence of RhoGTPases. This activity enhances the transport of integrin beta containing vesicles to the plasma membrane, which is essential for the tumor cell adhesion to the extracellular matrix (ECM)* [52].

Figure 14 Scheme of the process of one-step SLIC . *Vector is firstly to be linearized by restriction enzyme of inverse PCR. In the meantime, inserts are prepared by PCR, with more than 15 base pairs (bps) homology to the vector ends. Afterwards, linearized vectors are mixed with prepared, and the mixtures are incubated at RT for 2.5 min, generating 3' overhangs with T4 DNA polymerase. The ratio between vectors and inserts are calculated (Table 9). DNA mixtures are then incubated on ice for 10 min and transformed into competent E.coli directly* [53].

Figure 15 Scheme of the process of KLD reaction. *Exponential amplification of target DNA is performed by phusion PCR as described in section 3.2.1. Afterwards, the DNA product is incubated with KLD enzyme mix for 1 h at 37°C. This enzyme mixture contains a kinase, a ligase and DpnI, allowing rapid PCR product ligation and template removal. DNA mixtures are then transformed into competent E.coli directly [54].*

Figure 16 Cellular localization of DIAPH1. *HT-29 (upper panel) and HCT-116 (lower panel) cells were synchronized in meta-phase by double thymidine block, fixed and stained for DIAPH1 (green) and MTs (red) using specific Alexa-Flour-488 or Alexa-Flour 568-coupled antibodies. Chromosomes were stained with DAPI (blue). The right images are merged from all three channels. Bar: 5µm.*

Figure 17 Depletion of DIAPH1 in colorectal carcinoma cells. *HCT-116 and HT-29 cells were transduced with shRNA lentivirus against human DIAPH1 (sh4 and sh5), or with scrambled shRNA viral particles, and then selected with puromycin (2.0 µg/ml). Expression levels of DIAPH1 gene were examined by western blotting and quantified using ImageJ software. HSC70 served as loading control. Data were normalized to DIAPH1 controls and shown as mean ± SD from 3 independent experiments. ***P <0.001.*

Figure 18 Depletion of DIAPH1 reduces the speed of spindle MT movement in metaphase. *HT-29 and HCT-116 cells were incubated with SiR tubulin and spindle dynamics were imaged from meta- to anaphase by a spinning disk laser microscope. (A) Shown are three-dimensional (3D) reconstruction images created with the IMARIS software of HT-29 cells from metaphase to anaphase. (B) Spindle MT speed dynamics (µm/h) was calculated using IMARIS software at different time points. Upper panel: HT-29 cells, Lower panel: HCT-116 cells. (C) Shown are mean spindle MT speed of both HT-29 and HCT-116 cells at metaphase from time point 1-6. Data were calculated from at least 30 cells per cell line in two different experiments and represented as mean ± SD. *p<0.05.*

Figure 19 Determination of the cellular tubulin to DIAPH1 ratio. *Different amount of protein standards (GST-DIAPH1and tubulin proteins) as well as 20 µg protein extracted from HT-29 cells were loaded to and separated by SDS-PAGE gel, and then blotted onto nitrocellulose membrane. The amount of cellular DIAPH1 and tubulin were analyzed by comparing their relative band intensities to those of GST-DIAPH1 and tubulin proteins. These band signals were detected by a chemiluminescence imaging system using specific peroxidase coupled antibodies. Mean values of those four intensities were calculated and the cellular binding ratio was then analyzed. (Tubulin: 15 ng/µg and DIAPH1: 5 ng/µg).*

Figure 20 Effect of DIAPH1 FL and DIAPH1 FH2 on MT-polymerization. *The proteins were concentrated and running buffer was replaced with MT-buffer. Final concentrations of proteins were adjusted with MT-buffer based on the molecular ratio of GST-DIAPH1 FL to tubulin (1: 3) and of GST-DIAPH1 FH2 to tubulin (1: 6.7). (A) Shown is the SDS-PAGE of proteins before and after concentrating and buffer exchange. The concentration was estimated using 0.5µg BSA as standard. (B)Tubulin was incubated in GTP-containing MT-buffer for 7h at 37°C in presence of GST (control), FL or FH2 in a Tecan reader.*

Figure 21 DIAPH1 controls chromosome alignment. *DIAPH1 control and knock down cells (sh4 and sh5) were synchronized in metaphase by double thymidine block. (A) HT-29 and HCT-116 cells were synchronized in metaphase by double thymidine block, fixed and stained for MTs (red) or CENP-A (green) using specific Alexa Flour 568 or Alexa Flour 488-coupled antibodies. Chromosome were stained with DAPI (blue). Bar: 5 µm. Shown are two representative images of HT-29 cells. (B) The number of metaphase control and DIAPH1 sh4 and sh5 cells exhibiting aligned or misaligned chromosomes was counted and the percentage of each type was calculated. 120 cells from two independent measurements were evaluated and a statistical significance was analyzed by the chi square test. Data were shown as mean ± SD. ***p<0.001.*

Figure 22 DIAPH1 controls chromosomal segregation. *Control and DIAPH1-depleted cells (sh4 and sh5) were synchronized in anaphase by double thymidine block. (A) The cells were fixed and stained for MTs (red), chromosomes (blue) and centromere protein A (CENP-A, green). Shown are representative images of HT-29 cells with segregated (upper panel) and mis-segregated chromosomes (lower panel).*

*(B, C) The normalized percentage of anaphase cells with mis-segregated chromosomes to control levels is shown. At least 120 cells per cell line were analyzed and experiments were repeated twice. Data were shown as mean ± SD. *p<0.05, **p<0.01.*

Figure 23 Chromosome number of control and DIAPH1 depleted cells. *Chromosomes were prepared from metaphase cells arrested by colchicine, and stained with Giemsa solution. (A) Upper panel: Shown is one representative preparation from control cells of each cell line. (B) Lower panel: The number of chromosomes from at least 180 control or DIAPH1-depleted cells was counted. Shown are median values of ± SD. ****p<0.0001; n.s. not significant.*

Figure 24 DIAPH1 controls formation of micronuclei. *Control and DIAPH1-depleted cells (sh4 and sh5) cells were fixed and stained for MTs (red), chromosomes (DAPI blue) and CENP-A (green). Micronucleus is indicated by the white arrow. (A) Shown is a representative image of micronuclei formation of HT-29 cells. (B) The relative percentage of cells with micronuclei to control levels is shown. Data were analyzed from 4 000 cells per cell line and shown as mean ± SD. *p<0.05, **p<0.01.*

Figure 25 Effect of DIAPH1 on cell viability and caspase-3/7 activity*. For analyzing cell viability, 2.5 × 10^3 cells/well were seeded in triplicate, mixed with MTs reagent and the absorbance of the treated cells was measured at OD490 nm using absorbance-based plate reader. To compare the differences in cell apoptosis between control and DIAPH1 knock down cells, 2.0 × 10^4 cells per well were seeded in corning® 96-well white plates and apoptosis was analyzed by measuring the caspase-3/7 activities using TECAN microplate readers. (A) The viability of HCT-116 cells or HT-29 cells were analyzed using the MTs assay and the absorbance at OD490 nm were measured at 24 h, 48 h, 72 h and 96 h, normalizing by the absorbance values at 24 h. Shown are mean values of ± SD from two different assays. (B) Shown is the normalized relative light units (RLUs) for HCT-116 (left) and HT-29 cells (right) at 24 h, 48 h and 72 h, performed by luminescent assay. Shown are mean values ± SD from three independent assays. n.s. not significant.*

Figure 26 Effect of DIAPH1 on paclitaxel treatment for HCT-116 and HT-29 cells. *1.0 × 10^4 cells/well were seeded in 96-well microplates and cell viability were measured by MT-assay after treating with different concentrations of paclitaxel. Relative cell viability was normalized by the viability at 24 h. (A) Shown is the relative viability of HCT-116 cells at 24 h and 72 h. Cells were treated with paclitaxel with low concentrations (0 nM, 0.5 nM, 1.0 nM, 5.0 nM, 7.0 nM and 10 nM). (B) Shown is the relative viability of HT-29 cells after treating with high concentrations of paclitaxel (0 µM, 0.5 µM, 1.0 µM, 2.0 µM, 5.0 µM and 10 µM) at 24 h and 72 h. Shown are mean values ± SEM from three different assays, *p <0.05, **p <0.01, n.s. not significant.*

Figure 27 Levels of cytokine expression in control and DIAPH1-depleted cells. *Lysates from control and sh5 HCT-116 and HT-29 cells were analyzed for cytokines levels using the Human Cytokine Array Panel A from R&D Systems. (A) The spots of the upper and lower lay represent the reference signals. The other dots representing the cytokines are listed under https://resources.rndsystems.com/pdfs/datasheets/ary005b.pdf. The red arrow marks the signal for IL- 1ra. (B) Right panel: The human cytokine expression ratio of sh5 to control cells is shown. The expression levels were regarded as band intensities measured by ImageJ (Fiji) and the signals were detected using ImageQuant LAS 4000 Imager by electrochemiluminescence (ECL) detection system. The black bar: HCT-116 sh5/control ratio; the gray bar: HT-29 sh5/control ratio.*

Figure 28 Effect of DIAPH1 FL and DIAPH1 FH2 on MT bundling assay. *GST-DIAPH1 FL and GST-DIAPH1 FH2 were rebuffed and the final concentration of GST-DIAPH1 FH2 were prepared as 0.45-fold as that of FL. Shown is the fluorescence images after coincubation of GST-DIAPH1 proteins with labeled MTs for 10 min, using fluorescence microscope.*

9.4 List of tables

10 Reference

1. Dekker E, Tanis PJ, Vleugels JLA, Kasi PM, Wallace MB. Colorectal cancer. *Lancet Lond Engl*. 2019;394(10207):1467-1480. doi:10.1016/S0140-6736(19)32319-0

2. Xie Y-H, Chen Y-X, Fang J-Y. Comprehensive review of targeted therapy for colorectal cancer. *Signal Transduct Target Ther*. 2020;5(1):22. doi:10.1038/s41392-020-0116-z

3. Modest DP, Pant S, Sartore-Bianchi A. Treatment sequencing in metastatic colorectal cancer. *Eur J Cancer Oxf Engl 1990*. 2019;109:70-83. doi:10.1016/j.ejca.2018.12.019

4. Woo IS, Jung YH. Metronomic chemotherapy in metastatic colorectal cancer. *Cancer Lett*. 2017;400:319-324. doi:10.1016/j.canlet.2017.02.034

5. Ahmed D, Eide PW, Eilertsen IA, et al. Epigenetic and genetic features of 24 colon cancer cell lines. *Oncogenesis*. 2013;2:e71. doi:10.1038/oncsis.2013.35

6. Pretzsch E, Bösch F, Neumann J, et al. Mechanisms of Metastasis in Colorectal Cancer and Metastatic Organotropism: Hematogenous versus Peritoneal Spread. *J Oncol*. 2019;2019:7407190. doi:10.1155/2019/7407190

7. Gervaz P, Cerottini J-P, Bouzourene H, et al. Comparison of microsatellite instability and chromosomal instability in predicting survival of patients with T3N0 colorectal cancer. *Surgery*. 2002;131(2):190-197. doi:10.1067/msy.2002.119816

8. Burt R. Inheritance of Colorectal Cancer. *Drug Discov Today Dis Mech*. 2007;4(4):293-300. doi:10.1016/j.ddmec.2008.05.004

9. Nguyen HT, Duong H-Q. The molecular characteristics of colorectal cancer: Implications for diagnosis and therapy. *Oncol Lett*. 2018;16(1):9-18. doi:10.3892/ol.2018.8679

10. Vargas-Rondón N, Villegas VE, Rondón-Lagos M. The Role of Chromosomal Instability in Cancer and Therapeutic Responses. *Cancers*. 2017;10(1). doi:10.3390/cancers10010004

11. Thompson LL, Jeusset LM-P, Lepage CC, McManus KJ. Evolving Therapeutic Strategies to Exploit Chromosome Instability in Cancer. *Cancers*. 2017;9(11). doi:10.3390/cancers9110151

12. Bakhoum SF, Silkworth WT, Nardi IK, Nicholson JM, Compton DA, Cimini D. The mitotic origin of chromosomal instability. *Curr Biol CB*. 2014;24(4):R148-149. doi:10.1016/j.cub.2014.01.019

13. Johnson SC, McClelland SE. Watching cancer cells evolve through chromosomal instability. *Nature*. 2019;570(7760):166-167. doi:10.1038/d41586-019-01709-2

14. Bolhaqueiro ACF, Ponsioen B, Bakker B, et al. Ongoing chromosomal instability and karyotype evolution in human colorectal cancer organoids. *Nat Genet*. 2019;51(5):824-834. doi:10.1038/s41588-019-0399-6

15. Thompson SL, Bakhoum SF, Compton DA. Mechanisms of chromosomal instability. *Curr Biol CB*. 2010;20(6):R285-295. doi:10.1016/j.cub.2010.01.034

16. Kops GJPL, Weaver BAA, Cleveland DW. On the road to cancer: aneuploidy and the mitotic checkpoint. *Nat Rev Cancer*. 2005;5(10):773-785. doi:10.1038/nrc1714

17. Fernández-Casañas M, Chan K-L. The Unresolved Problem of DNA Bridging. *Genes*. 2018;9(12). doi:10.3390/genes9120623

18. Lengauer C, Kinzler KW, Vogelstein B. Genetic instability in colorectal cancers. *Nature*. 1997;386(6625):623-627. doi:10.1038/386623a0

19. Bakhoum SF, Thompson SL, Manning AL, Compton DA. Genome stability is ensured by temporal control of kinetochore-microtubule dynamics. *Nat Cell Biol*. 2009;11(1):27-35. doi:10.1038/ncb1809

20. Walczak CE, Cai S, Khodjakov A. Mechanisms of chromosome behaviour during mitosis. *Nat Rev Mol Cell Biol*. 2010;11(2):91-102. doi:10.1038/nrm2832

21. Chromosome Segregation - an overview | ScienceDirect Topics. Accessed September 8, 2020. https://www.sciencedirect.com/topics/biochemistry-genetics-and-molecular-biology/chromosome-segregation

22. Glotzer M. The 3Ms of central spindle assembly: microtubules, motors and MAPs. *Nat Rev Mol Cell Biol*. 2009;10(1):9-20. doi:10.1038/nrm2609

23. Lara-Gonzalez P, Westhorpe FG, Taylor SS. The spindle assembly checkpoint. *Curr Biol CB*. 2012;22(22):R966-980. doi:10.1016/j.cub.2012.10.006

24. Dou Z, Prifti DK, Gui P, Liu X, Elowe S, Yao X. Recent Progress on the Localization of the Spindle Assembly Checkpoint Machinery to Kinetochores. *Cells*. 2019;8(3). doi:10.3390/cells8030278

25. Vicente JJ, Wordeman L. The quantification and regulation of microtubule dynamics in the mitotic spindle. *Curr Opin Cell Biol*. 2019;60:36-43. doi:10.1016/j.ceb.2019.03.017

26. Kline-Smith SL, Walczak CE. Mitotic spindle assembly and chromosome segregation: refocusing on microtubule dynamics. *Mol Cell*. 2004;15(3):317-327. doi:10.1016/j.molcel.2004.07.012

27. McClelland SE. Role of chromosomal instability in cancer progression. *Endocr Relat Cancer*. 2017;24(9):T23-T31. doi:10.1530/ERC-17-0187

28. Cimini D, Degrassi F. Aneuploidy: a matter of bad connections. *Trends Cell Biol*. 2005;15(8):442-451. doi:10.1016/j.tcb.2005.06.008

29. Cimini D, Moree B, Canman JC, Salmon ED. Merotelic kinetochore orientation occurs frequently during early mitosis in mammalian tissue cells and error correction is achieved by two different mechanisms. *J Cell Sci*. 2003;116(Pt 20):4213-4225. doi:10.1242/jcs.00716

30. Cimini D, Howell B, Maddox P, Khodjakov A, Degrassi F, Salmon ED. Merotelic kinetochore orientation is a major mechanism of aneuploidy in mitotic mammalian tissue cells. *J Cell Biol*. 2001;153(3):517-527. doi:10.1083/jcb.153.3.517

31. Kinetochore microtubule dynamics and the metaphase-anaphase transition. *J Cell Biol*. 1995;131(3):721-734.

32. Swanton C, Tomlinson I, Downward J. Chromosomal instability, colorectal cancer and taxane resistance. *Cell Cycle Georget Tex*. 2006;5(8):818-823. doi:10.4161/cc.5.8.2682

33. Extra JM, Rousseau F, Bruno R, Clavel M, Le Bail N, Marty M. Phase I and pharmacokinetic study of Taxotere (RP 56976; NSC 628503) given as a short intravenous infusion. *Cancer Res*. 1993;53(5):1037-1042.

34. Tao W, South VJ, Zhang Y, et al. Induction of apoptosis by an inhibitor of the mitotic kinesin KSP requires both activation of the spindle assembly checkpoint and mitotic slippage. *Cancer Cell*. 2005;8(1):49-59. doi:10.1016/j.ccr.2005.06.003

35. Burbank KS, Mitchison TJ. Microtubule dynamic instability. *Curr Biol CB*. 2006;16(14):R516-517. doi:10.1016/j.cub.2006.06.044

36. Arden JD, Lavik KI, Rubinic KA, et al. Small-molecule agonists of mammalian Diaphanous–related (mDia) formins reveal an effective glioblastoma anti-invasion strategy. *Mol Biol Cell*. 2015;26(21):3704. doi:10.1091/mbc.E14-11-1502

37. Lammers M, Rose R, Scrima A, Wittinghofer A. The regulation of mDia1 by autoinhibition and its release by Rho•GTP. *EMBO J*. 2005;24(23):4176-4187. doi:10.1038/sj.emboj.7600879

38. Chesarone MA, DuPage AG, Goode BL. Unleashing formins to remodel the actin and microtubule cytoskeletons. *Nat Rev Mol Cell Biol*. 2010;11(1):62-74. doi:10.1038/nrm2816

39. Copeland SJ, Green BJ, Burchat S, Papalia GA, Banner D, Copeland JW. The Diaphanous Inhibitory Domain/Diaphanous Autoregulatory Domain Interaction Is Able to Mediate Heterodimerization between mDia1 and mDia2. *J Biol Chem*. 2007;282(41):30120-30130. doi:10.1074/jbc.M703834200

40. Palazzo AF, Cook TA, Alberts AS, Gundersen GG. mDia mediates Rho-regulated formation and orientation of stable microtubules. *Nat Cell Biol*. 2001;3(8):723-729. doi:10.1038/35087035

41. Bartolini F, Moseley JB, Schmoranzer J, Cassimeris L, Goode BL, Gundersen GG. The formin mDia2 stabilizes microtubules independently of its actin nucleation activity. *J Cell Biol*. 2008;181(3):523-536. doi:10.1083/jcb.200709029

42. Ishizaki T, Morishima Y, Okamoto M, Furuyashiki T, Kato T, Narumiya S. Coordination of microtubules and the actin cytoskeleton by the Rho effector mDia1. *Nat Cell Biol*. 2001;3(1):8-14. doi:10.1038/35050598

43. Yasuda S, Oceguera-Yanez F, Kato T, et al. Cdc42 and mDia3 regulate microtubule attachment to kinetochores. *Nature*. 2004;428(6984):767-771. doi:10.1038/nature02452

44. Cheng L, Zhang J, Ahmad S, et al. Aurora B regulates formin mDia3 in achieving metaphase chromosome alignment. *Dev Cell*. 2011;20(3):342-352. doi:10.1016/j.devcel.2011.01.008

45. Grueb SS, Muhs S, Popp Y, et al. The formin Drosophila homologue of Diaphanous2 (Diaph2) controls microtubule dynamics in colorectal cancer cells independent of its FH2-domain. *Sci Rep*. 2019;9(1):5352. doi:10.1038/s41598-019-41731-y

46. Lin Y-N, Bhuwania R, Gromova K, et al. Drosophila homologue of Diaphanous 1 (DIAPH1) controls the metastatic potential of colon cancer cells by regulating microtubule-dependent adhesion. *Oncotarget*. 2015;6(21):18577-18589. doi:10.18632/oncotarget.4094

47. Naj X, Hoffmann A-K, Himmel M, Linder S. The formins FMNL1 and mDia1 regulate coiling phagocytosis of Borrelia burgdorferi by primary human macrophages. *Infect Immun*. 2013;81(5):1683-1695. doi:10.1128/IAI.01411-12

48. Su AI, Wiltshire T, Batalov S, et al. A gene atlas of the mouse and human protein-encoding transcriptomes. *Proc Natl Acad Sci U S A*. 2004;101(16):6062-6067. doi:10.1073/pnas.0400782101

49. Tanji M, Ishizaki T, Ebrahimi S, et al. mDia1 targets v-Src to the cell periphery and facilitates cell transformation, tumorigenesis, and invasion. *Mol Cell Biol*. 2010;30(19):4604-4615. doi:10.1128/MCB.00197-10

50. Lin Y-N, Izbicki JR, König A, et al. Expression of DIAPH1 is up-regulated in colorectal cancer and its down-regulation strongly reduces the metastatic capacity of colon carcinoma cells. *Int J Cancer*. 2014;134(7):1571-1582. doi:10.1002/ijc.28486

51. Schiewek J, Schumacher U, Lange T, et al. Clinical relevance of cytoskeleton associated proteins for ovarian cancer. *J Cancer Res Clin Oncol*. 2018;144(11):2195-2205. doi:10.1007/s00432-018-2710-9

52. Lin Y-N, Windhorst S. Diaphanous-related formin 1 as a target for tumor therapy. *Biochem Soc Trans*. 2016;44(5):1289-1293. doi:10.1042/BST20160120

53. Jeong J-Y, Yim H-S, Ryu J-Y, et al. One-Step Sequence- and Ligation-Independent Cloning as a Rapid and Versatile Cloning Method for Functional Genomics Studies. *Appl Environ Microbiol*. 2012;78(15):5440-5443. doi:10.1128/AEM.00844-12

54. Biolabs NE. KLD Enzyme Mix | NEB. Accessed September 14, 2020. https://international.neb.com/products/m0554-kld-enzyme-mix

55. Kato T, Watanabe N, Morishima Y, Fujita A, Ishizaki T, Narumiya S. Localization of a mammalian homolog of diaphanous, mDia1, to the mitotic spindle in HeLa cells. *J Cell Sci*. 2001;114(Pt 4):775-784.

56. Bakhoum SF, Ngo B, Laughney AM, et al. Chromosomal instability drives metastasis through a cytosolic DNA response. *Nature*. 2018;553(7689):467-472. doi:10.1038/nature25432

57. Norppa H, Falck GC-M. What do human micronuclei contain? *Mutagenesis*. 2003;18(3):221-233. doi:10.1093/mutage/18.3.221

58. Proudfoot KG, Anderson SJ, Dave S, et al. Checkpoint Proteins Bub1 and Bub3 Delay Anaphase Onset in Response to Low Tension Independent of Microtubule-Kinetochore Detachment. *Cell Rep*. 2019;27(2):416-428.e4. doi:10.1016/j.celrep.2019.03.027

59. Mackenzie KJ, Carroll P, Martin C-A, et al. cGAS surveillance of micronuclei links genome instability to innate immunity. *Nature*. 2017;548(7668):461-465. doi:10.1038/nature23449

60. Amsen D, de Visser KE, Town T. Approaches to determine expression of inflammatory cytokines. *Methods Mol Biol Clifton NJ*. 2009;511:107-142. doi:10.1007/978-1-59745-447-6_5

61. Holohan C, Van Schaeybroeck S, Longley DB, Johnston PG. Cancer drug resistance: an evolving paradigm. *Nat Rev Cancer*. 2013;13(10):714-726. doi:10.1038/nrc3599

62. Stanton RA, Gernert KM, Nettles JH, Aneja R. Drugs That Target Dynamic Microtubules: A New Molecular Perspective. *Med Res Rev*. 2011;31(3):443-481. doi:10.1002/med.20242

63. Weaver BAA, Cleveland DW. Decoding the links between mitosis, cancer, and chemotherapy: The mitotic checkpoint, adaptation, and cell death. *Cancer Cell*. 2005;8(1):7-12. doi:10.1016/j.ccr.2005.06.011

64. Sudo T, Nitta M, Saya H, Ueno NT. Dependence of paclitaxel sensitivity on a functional spindle assembly checkpoint. *Cancer Res*. 2004;64(7):2502-2508. doi:10.1158/0008-5472.can-03-2013

65. Cisyk AL, Penner-Goeke S, Lichtensztejn Z, et al. Characterizing the prevalence of chromosome instability in interval colorectal cancer. *Neoplasia N Y N*. 2015;17(3):306-316. doi:10.1016/j.neo.2015.02.001

66. Tanaka K. Dynamic regulation of kinetochore-microtubule interaction during mitosis. *J Biochem (Tokyo)*. 2012;152(5):415-424. doi:10.1093/jb/mvs109

67. Watanabe N, Madaule P, Reid T, et al. p140mDia, a mammalian homolog of Drosophila diaphanous, is a target protein for Rho small GTPase and is a ligand for profilin. *EMBO J*. 1997;16(11):3044-3056. doi:10.1093/emboj/16.11.3044

68. Kuniyasu K, Iemura K, Tanaka K. Delayed Chromosome Alignment to the Spindle Equator Increases the Rate of Chromosome Missegregation in Cancer Cell Lines. *Biomolecules*. 2018;9(1). doi:10.3390/biom9010010

69. Chapiro E, Antony-Debre I, Marchay N, et al. Sex chromosome loss may represent a disease-associated clonal population in chronic lymphocytic leukemia. *Genes Chromosomes Cancer*. 2014;53(3):240-247. doi:10.1002/gcc.22134

70. Park S-J, Jeong S-Y, Kim HJ. Y chromosome loss and other genomic alterations in hepatocellular carcinoma cell lines analyzed by CGH and CGH array. *Cancer Genet Cytogenet*. 2006;166(1):56-64. doi:10.1016/j.cancergencyto.2005.08.022

71. He B, Gnawali N, Hinman AW, Mattingly AJ, Osimani A, Cimini D. Chromosomes missegregated into micronuclei contribute to chromosomal instability by missegregating at the next division. *Oncotarget*. 2019;10(28):2660-2674. doi:10.18632/oncotarget.26853

72. Gao D, Wu J, Wu Y-T, et al. Cyclic GMP-AMP synthase is an innate immune sensor of HIV and other retroviruses. *Science*. 2013;341(6148):903-906. doi:10.1126/science.1240933

73. Madej MP, Töpfer E, Boraschi D, Italiani P. Different Regulation of Interleukin-1 Production and Activity in Monocytes and Macrophages: Innate Memory as an Endogenous Mechanism of IL-1 Inhibition. *Front Pharmacol*. 2017;8:335. doi:10.3389/fphar.2017.00335

74. Fresno C del, Otero K, Gómez-García L, et al. Tumor Cells Deactivate Human Monocytes by Up-Regulating IL-1 Receptor Associated Kinase-M Expression via CD44 and TLR4. *J Immunol*. 2005;174(5):3032-3040. doi:10.4049/jimmunol.174.5.3032

75. Mytar B, Wołoszyn M, Szatanek R, et al. Tumor cell-induced deactivation of human monocytes. *J Leukoc Biol*. 2003;74(6):1094-1101. doi:10.1189/jlb.0403140

76. Sica A, Saccani A, Bottazzi B, et al. Autocrine production of IL-10 mediates defective IL-12 production and NF-kappa B activation in tumor-associated macrophages. *J Immunol Baltim Md 1950*. 2000;164(2):762-767. doi:10.4049/jimmunol.164.2.762

77. Kaplanov I, Carmi Y, Kornetsky R, et al. Blocking IL-1β reverses the immunosuppression in mouse breast cancer and synergizes with anti-PD-1 for tumor abrogation. *Proc Natl Acad Sci U S A*. 2019;116(4):1361-1369. doi:10.1073/pnas.1812266115

78. Baker KJ, Houston A, Brint E. IL-1 Family Members in Cancer; Two Sides to Every Story. *Front Immunol*. 2019;10:1197. doi:10.3389/fimmu.2019.01197

79. Birkbak NJ, Eklund AC, Li Q, et al. Paradoxical relationship between chromosomal instability and survival outcome in cancer. *Cancer Res*. 2011;71(10):3447-3452. doi:10.1158/0008-5472.CAN-10-3667

80. Laughney AM, Elizalde S, Genovese G, Bakhoum SF. Dynamics of Tumor Heterogeneity Derived from Clonal Karyotypic Evolution. *Cell Rep*. 2015;12(5):809-820. doi:10.1016/j.celrep.2015.06.065

11 Acknowledgements

First of all, I would like to thank Prof. Dr. Sabine Windhorst for giving me a chance to work in the lab and entrusting me with an interesting project. She always helps me out from scientific problems and gives me useful advice during the project. In the late stages of my PhD, she trains me a lot on the scientific writing and thinking, which promotes me to be a real research scientist. I would also like to thank her for the correction of my work and cares for my life in Germany.

Furthermore, I would like to thank Stefanie Muhs, Christine Blechner, Julia Arnold, Themis Paraschiakos, Willi Flat, and other colleagues in AG Windhorst for their kindness and patience to help me adapt to the life and work in the lab. They are always at my side with help and encouraged me when I stuck in the experiments.

In addition, I would also like to thank Dr. Leticia Oliveira-Ferrer and Prof. Dr. Thorsten Schinke for reviewing my thesis; thank Prof. Dr. Eva Tolosa and Manuela Kolster (Institute of Immunology, UKE) for performing the immunology assays; thank Dr. Siegrid Fuchs (Institute of Human Genetics, UKE) for performing the karyotype analysis: thank colleges in AG Itzen (Institute of Biochemistry and Signaling Transduction) for the introduction of protein purification; thank colleagues in AG Jücker (Institute of Biochemistry and Signaling Transduction) for sharing the experimental devices; thank UKE Microscopic Imaging Facility for providing the spinning disk confocal microscopy; thank Dr. Katrin Klempahn and other colleagues in the doctoral office for giving me advice on doctoral issues.

I am also quite appreciated the China Scholarship Council (CSC) offering me the scholarships and cares for my studies in Germany. Meanwhile, I acknowledge the Chinese Embassy in Germany supporting me with essential medical protection and kind regards during this Coronavirus Pandemic.

I also would like to thank my friends both in China and Germany. Our friendship gives me a safe feeling to share happiness and sadness.

Last but not least, I would like to thank my family, who care me a lot regardless of the distance and time difference between China and Germany. Personally, I would like to thank Canshan Lao. They support and love me all the time, which gives me the infinite power.

12 Curriculum vitae

Lebenslauf wurde aus datenschutzrechtlichen Gründen entfernt.

13 Eidesstattliche Erklärung

Ich versichere ausdrücklich, dass ich die Arbeit selbständig und ohne fremde Hilfe verfasst, andere als die von mir angegebenen Quellen und Hilfsmittel nicht benutzt und die aus den benutzten Werken wörtlich oder inhaltlich entnommenen Stellen einzeln nach Ausgabe (Auflage und Jahr des Erscheinens), Band und Seite des benutzten Werkes kenntlich gemacht habe.

Ferner versichere ich, dass ich die Dissertation bisher nicht einem Fachvertreter an einer anderen Hochschule zur Überprüfung vorgelegt oder mich anderweitig um Zulassung zur Promotion beworben habe.

Ich erkläre mich einverstanden, dass meine Dissertation vom Dekanat der Medizinischen Fakultät mit einer gängigen Software zur Erkennung von Plagiaten überprüft werden kann.

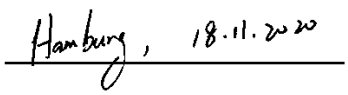

Place, Date

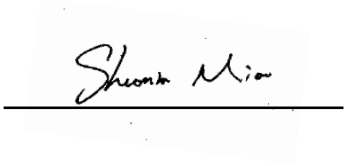

Signature